

國立交通大學

材料科學與工程學系

博士論文

軟性電路板及電極之製備與特性研究

及其於有機太陽能電池之應用

Fabrication and Characterization of Flexible Printed Circuit Boards
and Electrodes, and those Applications in Organic Solar Cells



研究生：蕭育生

指導教授：黃華宗 博士

中華民國九十八年四月

軟性電路板及電極之製備與特性研究及其於有機太陽能電池之應用

Fabrication and Characterization of Flexible Printed Circuit Boards
and Electrodes, and those Applications in Organic Solar Cells

研究生：蕭育生

Student : Yu-Sheng Hsiao

指導教授：黃華宗

Advisor : Wha-Tzong Whang



A Thesis

Submitted to Department of Materials Science and Engineering

College of Engineer

National Chiao Tung University

in Partial Fulfillment of the Requirements

for the Degree of

Doctor of Philosophy

in

Materials Science and Engineering

April 2009

Hsinchu, Taiwan, Republic of China

中華民國九十八年四月

軟性電路板及電極之製備與特性研究

及其於有機太陽能電池之應用

摘要

隨著能源危機的時代漸漸來臨，太陽能電池的發展也逐漸受重視。除了目前廣泛被使用的矽晶圓太陽能電池及無機薄膜太陽能電池技術外，有機太陽能電池因為具有低成本、耐衝擊、高產出及方便攜帶等優點，已成為新世代發展攜帶型電子產品的重點發展技術。本論文主要探討由低成本的濕式製程製備軟性印刷電路板、陰極及陽極，並且利用此兩種濕式製備電極的技術，去製備出全濕式製程的反式有機太陽能電池元件於軟性聚亞醯胺基材上，並探討其中的物性及化性對於元件中光電轉換效率的影響。另一部分，藉由探討不同電極的表面能對於有機小分子的自我組裝型態的不同，去提高有機太陽能電池的光電轉換效率。

本論文研究第一部分主要探討一種全濕式製程的表面鍍金屬化聚亞醯胺基板的製備及特性分析，而此表面的金屬與聚亞醯胺基板間有優異的接著性以期應用在軟性電子的軟性印刷電路板方面。此表面金屬化聚亞醯胺的製作方法為首先利用強鹼對亞醯胺環開環、再依序進行鍍金屬離子的離子交換、強還原劑還原出具有無電解電鍍鍍活性的無鈹系鍍金屬奈米顆粒當作品種、及最後利用鍍無電解電鍍增厚與平坦化鍍層。由原子力顯微鏡及掃描式電子顯微鏡的觀察，可以了解無鈹系鍍金屬奈米顆粒在鍍無電鍍液下的成長型態；搭配表面電阻的量測，可知鍍奈米顆粒經由無電解電鍍後明顯的導電度提升。綜合穿透式顯微鏡及膠帶接著性測試法的分析，可知此鍍薄膜可以控制在 382 nm 並且對於聚亞醯胺具有良好的接著性。

本論文研究第二部分是利用一簡單的後續表面改質物的旋轉塗佈處理方法去提升 poly(3,4-ethylenedioxythiophene)/poly(styrene-sulfonate) (PEDOT:PSS) 薄膜的導電度，並利用此技術應用在無銻錫氧化物(ITO-free)的高分子太陽能電池中。在此研究中，搭配選擇不同改質物(包含一個或多個極性官能基的醇類或醚類)，並利用不同的

分析方式去了解此溶劑效應對於 PEDOT:PSS 薄膜之導電度提升的真實原因。經由不同分析方式的分析，可以推測此溶劑處理之 PEDOT:PSS 薄膜的三維模型出來，而相信此研究對未來製作 ITO-free 的元件是有很大的幫助及潛能。

本論文研究第三部分是結合先前兩部分開發的部分技術，由鎳金屬化聚亞醯胺當作陰極及表面溶劑改質的高導電度 PEDOT:PSS 薄膜當作陽極，並且搭配 poly(3-hexylthiophene) (P3HT)及[6,6]-phenyl-C₆₁-butyric acid methyl ester (PCBM)的混成材料當作光電作用層去製作出全溶劑製程的反式結構 ITO-free 的高分子太陽能電池。而此顆粒狀導電鎳薄膜對於聚亞醯胺基材有良好的接著性且具有高的導電度 (ca. 2778 S cm⁻¹)，經由功函數的量測可知此方法製作出的電極為 3.9 eV，此結果有別於一般鎳金屬的功函數(5.4 eV)。製作出此反式結構的高分子太陽能電池製程中，會存在很多介面能不匹配的問題，例如在塗佈光電作用層之前，製程中會導入一層 titanium(diisopropoxide)bis(2,4-pentanedionate) (TIPD)當作電洞阻障層並且有利於得到良好成膜性的 P3HT:PCBM 薄膜於表面鎳金屬聚亞醯胺上。另外，在塗佈 PEDOT:PSS 薄膜之前，此研究會先使用五秒鐘溫和的氧電漿處理使主動層表面變成較親水的介面，進而有利於後續較親水性的 PEDOT:PSS 成膜，目前此系統的反式結構高分子太陽能電池製作最好的光電轉換效率約為 2.4% (AM 1.5 及 100 mW cm⁻² 條件下)。此技術的特點為完全濕式的製程。另外藉由 UV-vis、Haze effect、AFM 及 TEM 的分析，可以初步推斷此次微米級顆粒狀金屬電極具有幫助光在主動層內的吸收，以期提升反式結構之有機太陽能電池的效率。

本論文研究最後一部分是利用基材效應，藉由不同基材的表面能控制，經由熱蒸鍍方法去製備自我組裝之 copper phthalocyanine (CuPc)的奈米柱狀結構當施體，與覆蓋 fullerene (C60)當受體，以期達到理想的異質接面型有機太陽能電池。我們可以觀察到柱狀奈米結構的 CuPc 於 indium-tin oxide (ITO)、PEDOT:PSS 及 Au 上的自組裝型態的不同，CuPc 可以於 Au 表面進而形成理想的異質接面型主動層結構。藉由不同分析方法及理論計算去分析表面能對於沉積 CuPc 型態學的影響。於 OPV 的光電轉換效率探討方面，可推知由 PEDOT:PSS 表面造成的平躺及垂直站立混合型態之 CuPc 奈米柱薄膜，其相對於平面結構之元件的光電轉換效率有 50 倍以上的提升。

Fabrication and Characterization of Flexible Printed Circuit Boards and Electrodes, and those Applications in Organic Solar Cells

Abstract

Over the past two decades, satisfying the world's growing demand for energy is one of the most significant challenges facing society. Therefore, the development of solar energy is viewed as an ideal technology for power generation because it is clean and renewable. Although the photovoltaic (PV) technology platforms of silicon-based PV and thin-film PV are now undergoing a rapid expansion in production, the next generation PV—organic solar cells (OSCs)—could soon be playing a major role with the advantages of ultralow production costs, rugged and lightweight. One part of this dissertation describes the fabrication of cathodes and anodes with low costs and high-throughput-solution processes in attempt to apply in all-solution-processed OSCs on flexible substrates. In another part of this dissertation, the variable self-assembly behavior of small molecular on a diverse range of substrates (surface energies) was used to control the morphology of the interface and the degree of carrier transportation within the active layer in OSCs, and furthermore enhance the power conversion efficiency. All of the phenomena occurring are investigated in this thesis, and those techniques are believed the important roles for developing high efficiency and low-cost OSCs in the future.

In the first part of the dissertation, I discussed the fabrication of surface-nickelized polyimide films using a fully solution-based process, and excellent adhesion between the nickel and polyimide phases was observed. Flexible polyimide substrates were modified by alkaline hydrolysis, ion exchange, reduction and nickel electroless deposition without palladium. Atomic force microscopy and field emission scanning electron microscopy were used to follow the growth of nickel nanoparticles (Ni-NPs) and nickel layers on the polyimide surface. The surface resistances of the Ni-NPs/PI films and Ni/PI films, measured using a four-point probe, were 1.6×10^7 and $0.83 \text{ } \Omega/\text{cm}^2$, respectively. The thicknesses of Ni-NPs and the Ni layer on the polyimide surface were 82 nm and 382 nm,

respectively, as determined by transmission electron microscopy, and the Ni layer adhered well to PI, as determined by the adhesive tape testing method.

In the second part of this dissertation, I devised a simple method to enhance the conductivity of poly(3,4-ethylenedioxythiophene)-poly(styrene-sulfonate) (PEDOT:PSS) films through spin-coating with various surface-modified compounds, and then applied this technique to the preparation of ITO-free polymer solar cells (PSCs). The electrical conductivity of PEDOT:PSS films can be increased by more than two order of magnitudes merely by spin-coating a compound containing one or more polar groups—such as ethanol, methoxyethanol, 1,2-dimethoxyethane, and ethylene glycol—onto the films. The phenomena occurring are discussed through conductivities, morphologies, and chemical properties of the modified PEDOT:PSS films as determined using Raman spectroscopy, a four-point probe, scanning electron microscopy (SEM), atomic force microscopy (AFM), transmission electron microscopy (TEM), and X-ray photoelectron spectroscopy (XPS). The schematic 3D morphological model of directly solvent-modified PEDOT:PSS films is presumed for ITO-free devices. The desirable conductivity enhancements of these materials make them attractive candidates for use as anode materials in ITO-free PSCs.

In the third part of this dissertation, I prepared all-solution-processed inverted polymer solar cells (PSCs) incorporating two solution-processed electrodes—surface-nickelized polyimide films (NiPI films) as cathodes and high-conductivity poly(3,4-ethylenedioxythiophene)/poly(styrene-sulfonate) (PEDOT:PSS) films as anodes—and an active layer with a bulk heterojunction morphology of poly(3-hexylthiophene) (P3HT) and [6,6]-phenyl-C₆₁-butyric acid methyl ester (PCBM). The granular Ni thin films, which exhibited good adhesion and high conductivity (ca. 2778 S cm⁻¹) on the polyimide (PI) substrates and possessed a work function different from that of pure Ni metal (WF, 5.4 eV). Using ultraviolet photoelectron spectroscopy, we determined that the WF of the NiPI films was ca. 3.9 eV. Prior to the coating of the photoactive layer, the surface of the NiPI films were treated with titanium(diisopropoxide)bis(2,4-pentanedionate) (TIPD) solution to facilitate the deposition of high-quality active layer and further as a hole blocking layer. The solution processed anodes (solvent-modified PEDOT:PSS films) were further coated and subjected to mild oxygen plasma treatment on the active layer. Short exposure (5 s) to the plasma

improved the quality of the surface of the active layer for PEDOT:PSS deposition. These inverted PSCs on flexible granular NiPI films provided a power conversion efficiency of 2.4% when illuminated under AM 1.5 conditions (100 mW cm^{-2}). The phenomenon of light absorption enhancement in those inverted PSCs was observed as indicated in reflective UV-vis, haze factor and external quantum efficiency (EQE) responses. The resulting fill factor (FF) of 0.43 is still significantly lower than the FF of 0.64 for standard devices. When compared to the planar structure, the improvement of absorbance of light and good haze factors was obtained for granular structure which suggests NiPI as a better back contact electrode through enhancing the light trapping and scattering in inverted PSCs.

In the last part of this dissertation, I have prepared organic photovoltaic (OPV) cells possessing an ideal bulk heterojunction (BHJ) structure using the self-assembly of copper phthalocyanine (CuPc) as the donor material and fullerene (C60) as the acceptor. The variable self-assembly behavior of CuPc on a diverse range of substrates (surface energies) allowed us to control the morphology of the interface and the degree of carrier transportation within the active layer. We observed rod-like CuPc structures on indium–tin oxide (ITO), poly(3,4-ethylenedioxythiophene)-poly(4-styrenesulfonate) (PEDOT:PSS) and Au substrates. Accordingly, the interfaces and continuing transport path between CuPc and fullerene domains could be greatly improved due to the ideal BHJ structure. In this paper, we discuss the mechanisms of producing CuPc rod-like films on ITO, PEDOT:PSS and Au. The OPV cell performance was greatly enhanced when a mixture of horizontal and vertical CuPc rods was present on the PEDOT:PSS surfaces, i.e. the power conversion efficiency was 50 times greater than that of the corresponding device featuring a planar CuPc structure.

致謝

首先非常感謝黃華宗教授對我研究上的指導，特別要感謝的是黃老師對於我在交大的碩博研究生涯共六年的寬容與鼓勵。而黃老師在解惑、授業之餘，對於教化人心及傳揚救恩的熱忱，也讓我深受激勵。

感謝台灣大學材料系林金福教授、交通大學材料系韋光華教授、成功大學材料系許聯崇教授、交通大學顯示所陳方中副教授及工業技術研究院陳志平研究員於博士口試時所惠賜的寶貴意見，讓本論文得以更臻完善。

感謝達邁科技的吳昇昌學長、陳宗儀博士及同仁在聚亞醯胺方面等實驗及知識上的協助。感謝工業技術研究院的陳志平學長及L800全體同仁(丁副、柯寶、衛博、楊博、黃博、俊榮、昭穎、亮年、淑華、瑞芬、意君、怡伶、宜心、陳大哥)對於我實驗及生活上的幫助與鼓勵。感謝中興化工鄭如忠老師實驗室的成員(小丁學長、鑫磊學長、政哲學長、英孝等)對於我博班研究生涯的鼓舞及幫助。感謝以前中興化工的大學同學(弟弟、嘉慶等)在新竹一起為博班畢業而奮鬥與彼此鼓勵。感謝材料所韋老師實驗室的小豬學長、阿茂學長、耀德學長及茂源同學與應化所許千樹老師實驗室的小毛及小P對我實驗上的幫助與指教。感謝材料所其他實驗室的學長及學弟陪我一起打籃球瘦身。感謝黃華宗老師實驗室眾多的成員(慶勳學長、美慧學姐、小賢學長、佩君學姐、義男學長、守謙學長、惠晶學姐、國倫學長、玉芳學姐、柏霖同學、昭業同學、曉琪同學、國容、政榮、彥文、育銓、雅婷、惟昇、美嬋、宗哲、登元、俊超、也綠及佩君)的幫忙及生活上的照顧，使得各項實驗得以順利完成且使枯燥的研究生生活多彩多姿起來。感謝我的室友(大哥/智傑同學)在實驗與生活上的彼此幫助，很高興博班生涯有你相挺及一起加油，使我在交大材料的生活一點都不孤單，大哥你永遠是對的。感謝系辦余小姐、黃小姐、郎小姐及張小姐在博班口試期間於行政事務上的熱心協助。

最後，感謝我最親愛的家人(爸爸、媽媽、姐姐及姐夫)對我博士進修的支持與鼓勵，讓我得以完成研究論文，謝謝你們。

TABLE OF CONTENTS

摘要.....	I
Abstract.....	III
致謝.....	VI
LIST OF TABLES.....	IX
LIST OF FIGURES.....	XI
Chapter 1 Introduction.....	1
1.1 Background.....	1
1.2 Aims of Objectives.....	5
1.3 Brief Structures of this Thesis.....	7
Chapter 2 Literature Review.....	9
2.1 Polymer Substrates.....	9
2.2 Flexible Printed Circuit Boards.....	11
2.3 Electrode Materials.....	15
2.4 Organic Solar Cells.....	19
2.4.1 Principle of Operation.....	19
2.4.2 Built-in Potential.....	23
2.4.3 Excitons in Organic Materials.....	26
2.4.4 Conjugated Materials for Polymer Solar Cells.....	28
2.4.5 Small Molecular Materials for Organic Solar Cells.....	29
2.5 Device Architectures for Organic Solar Cells.....	30
2.6 Characterizing Efficiency.....	33
2.6.1 Current-Voltage Characteristics.....	33
2.6.2 Equivalent Circuit Diagrams.....	35
2.6.3 Spectral Response.....	35
2.6.4 Air Mass.....	38
2.6.5 Power Efficiencies under Solar Conditions.....	40
2.7 Surface Energy.....	42
2.7.1 Definition of Surface Energy.....	42
2.7.2 Surface Energy of Solids.....	43
Chapter 3 Materials and Experimental Techniques.....	45
3.1 Materials.....	45
3.2 Experimental Techniques.....	35

3.2.1 Preparation of Polyimide Films.....	50
3.2.2 Preparation of Surface-Nickelized Polyimide Films.....	50
3.2.3 Device Fabrication.....	51
Chapter 4 Chemical Formation of Palladium-free Surface-nickelized Polyimide Film for Flexible Electronics.....	57
4.1 Introduction.....	58
4.2 Experimental Details.....	60
4.2.1 Materials.....	60
4.2.2 Preparation of polyimide films.....	60
4.2.3 Preparation of the surface-nickelized polyimide films.....	60
4.2.4 Measurements.....	62
4.3 Result and Discussion.....	63
4.4 Conclusion.....	80
4.5 Appendix.....	81
Chapter 5 High-Conductivity Poly(3,4-ethylenedioxythiophene):Poly(styrene sulfonate) Film for Use in ITO-Free Polymer Solar Cells.....	85
5.1 Introduction.....	86
5.2 Experiment Details.....	89
5.2.1 Materials and Polymer Solar Cells.....	89
5.2.2 Instrumentation.....	90
5.3 Result and Discussion.....	91
5.3.1 The Origin of Conductivity Enhancement of Surface-modified PEDOT:PSS Films.....	91
5.3.2 Application of Solvent-modified PEDOT:PSS Film in ITO-free Solar Cells.....	105
5.5 Conclusion.....	108
Chapter 6 All-Solution-Processed Inverted Polymer Solar Cells on Granular Surface-Nickelized Polyimide.....	109
6.1 Introduction.....	110
6.2 Experiment Details.....	115
6.2.1 Nickelized Polyimide Films (Cathodes and Substrates).....	115
6.2.2 Active-Layer Materials.....	115
6.2.3 High-Conductivity PEDOT:PSS Films (Anodes).....	116
6.2.4 Instrumentation.....	117

6.3 Result and Discussion.....	119
6.5 Conclusion.....	135
Chapter 7 Morphological Control of CuPc and its Application in Organic Solar Cells.....	136
7.1 Introduction.....	137
7.2 Experiment Details.....	140
7.3 Result and Discussion.....	141
7.4 Conclusion.....	158
Chapter 8 Conclusions and Prospects.....	159
References.....	165
List of Publications.....	180
Resume.....	181



LIST OF TABLES

Table 2.1	Basic properties of polymers used for base substrate. (Note: PET: Polyethylene terephthalate; PEN: Polyethylene naphthalate; PC: Polycarbonate; PES: Polyethersulphone; PAR: Polyarylate; PCO: Polycyclic olefin; PI: Polyimide.).....	10
Table 2.2	WF of the elements. The numbers refer to the WF (eV) of the elements in polycrystalline form.....	17
Table 2.3	WF and sheet resistance of the transparent conducting electrode materials. (Note: Indium tin oxide (ITO); Fluorine-doped tin oxide (FTO); Aluminum-doped zinc oxide (AZO); poly(3,4-ethylenedioxythiophene)-poly(styrene-sulfonate) (PEDOT:PSS); vapor-phase polymerization poly(3,4-ethylenedioxythiophene)-Fe(III)-tosylate (VPP-PEDOT-Tos); Single-walled carbon nanotube (SWNT); Multi-walled carbon nanotube (MWNT).).....	18
Table 3.1	Overview CLEVIOS™ general properties. (Note: The previous trade code of CLEVIOS productions was named Bytron.).....	48
Table 4.1	Dependence of relative surface imide content of PI films and surface morphology of Ni-NPs/ PI films on treatment time with KOH.....	65
Table 4.2	Relative surface imide content on polyimide throughout process.....	67
Table 4.3	Contact angles and surface energies of pristine PI and different stages of modification of PI.....	69
Table 4.4	Surface resistances and tape adhesion testing results of bare PI and metalized PI.....	72
Table 5.1	Sheet resistances and transmittances of the PEDOT:PSS films.....	92
Table 5.2	Atomic percentages of PEDOT and PSS and PEDOT-to-PSS ratios (from XPS data, calculated using the Shirley method).....	102
Table 5.3	Performance of PEDOT:PSS/P3HT:PCBM/Ca/Al photovoltaic devices with various active areas under illumination of AM 1.5 (100 mW cm ⁻²).....	107
Table 6.1	Contact angles and surface energies obtained after performing the inverted fabrication process.....	116
Table 6.2	Sheet resistances and conductivities of PEDOT:PSS, ITO, and NiPI films.....	125
Table 6.3	Performance of PSCs under AM 1.5 illumination (100 mW cm ⁻²).....	128
Table 7.1	Effect of substrate on CuPc film morphology. (Note: ITO: Indium tin oxide glass treated with a plasma cleaner. PITO: PEDOT:PSS films (ca. 50 nm) coated on ITO. AITO: Au layers (ca. 20 Å) deposited by TE on ITO.....	147

Table 7.2 Calculated values of surface energy for polymers.....151

Table 7.3 Performance of CuPc films in photovoltaic cells. All devices were measured under illumination of AM 1.5 (100 mW/cm²). (Note: **PHJ**: Planar heterojunction structure. **h-BHJ**: Horizontal-rod-based bulk heterojunction structure. **m-BHJ**: Mixture of horizontal- and vertical-rod bulk heterojunction structure. **v-BHJ**: Vertical-rod-based bulk heterojunction structure.....157



LIST OF FIGURES

Chapter 1 Introduction

- Figure 1.1 Progress of research-scale photovoltaic device efficiencies, under AM 1.5 simulated solar illumination for a variety of technologies (as compiled by Larry Kazmerski, National Renewable Energy Laboratory).....2
- Figure 1.2 Schematic flow chart showing the important processes in organic solar cells. Recombination of excitons can be radiative or non-radiative.....3

Chapter 2 Literature Review

- Figure 2.1 Schematic diagram of roll-to-roll process of OSC modules (from Konarka Technologies, Inc.).....10
- Figure 2.2 Development of flexible printed circuit boards.....12
- Figure 2.3 Schematic diagram of the mechanism for direct metallization of a polyimide film surface using an ion-doped precursor layer. (A) Reduction of copper ions via self-oxidative decomposition of DMAB in aqueous solution. (B) Formation of copper atoms followed by protonation of the remaining carboxylate anion groups. (C) Ion-exchange reaction between protons and copper ions through the generation of a concentration gradient of these ions in the precursor layer, and further reduction of copper ions at the film surface.....14
- Figure 2.4 Effect of DMAB reduction temperature on the peel strength of the resulting copper film formed on the surface-modified polyimide film.....14
- Figure 2.5 Transparency of a 30-nm-thick nanotube film with 200 Ω /sq. sheet resistance, together with the transparency of ITO on glass 15 Ω /sq.....17
- Figure 2.6 Metal-insulator-metal (MIM) picture of organic diode device function. (a) Closed circuit condition: under illumination photogenerated charges drift toward the contacts. (b) Flat band or open circuit condition: the current becomes zero. (c) Reversed bias: photogenerated charges drift in strong electric fields, the diode operates as a photodetector. (d) Forward bias larger than V_{OC} : the injection increases and the diode opens up.....20
- Figure 2.7 Schematic representation of general excitonic mechanism for photoenergy conversion in organic solar cells.....22
- Figure 2.8 Schematic representation of elementary steps in the process of photoinduced charge separation for a donor (D) and an acceptor (A): (1) Photoexcitation of the

donor; (2) diffusion of the exciton and formation of an encounter pair; (3) electron transfer within the encounter pair to form a geminate pair; (4) charge separation.....	23
Figure 2.9 Schematic diagrams of built-in potential in metal/polymer/metal structures.....	25
Figure 2.10 Open-circuit voltage (V_{oc}) of different bulk-heterojunction solar cells plotted versus the oxidation potential/HOMO position of the donor polymer used in each individual device.....	25
Figure 2.11 Current – voltage curve of (P3HT)/PCBM solar cell measured in the dark (solid line) and field-driven photocurrent (dotted line). The built-in potential VBI is given by $ELUMO(PCBM) - EHOMO(P3HT) (-4.3 V - (-5.1 V) = 0.8 V)$..	25
Figure 2.12 Schematic diagrams of different types of excitons in organic semiconductors...	27
Figure 2.13 Several solution processible conjugated polymers and a fullerene derivative used in organic solar cells. Upper row: the p-type holeconducting donor polymers MDMO-PPV, P3HT and PFB. Lower row: the electronconducting acceptor polymers CN-MEH-PPV and F8BT and a soluble derivative of C60, PCBM (1-(3-methoxycarbonyl) propyl-1-phenyl[6,6]C61).....	28
Figure 2.14 Several small molecular materials used in organic solar cells. Donor (p-type) materials: ZnPc, CuPc, Me-PTCDI, Pentacene and PTCDA. Acceptor (n-type) materials: C60, NTCDA and DAAQ. Exciton blocking material: BCP.....	29
Figure 2.15 The most common device architectures for organic solar cells. Material B is any organic material. A is an electron acceptor material and D is an electron donor material.....	32
Figure 2.16 Illustration of the difference between a real and an ideal I-V curve. The area of the inner rectangle corresponds to the maximal output power of the real device (at the maximum power point), whereas the area of the outer rectangle formed by the axes and the ideal I-V curve is equivalent to the maximum ideal output power.....	34
Figure 2.17 Equivalent circuit diagrams for a solar cell.....	35
Figure 2.18 Number of photons (N_{ph}) absorbed in the active layer under AM 1.5G calculated by transfer-matrix formalism (TMF), for a device having the following structure: glass (1 mm)/ITO (140 nm)/PEDOT:PSS (50 nm)/P3HT:PCBM (x nm)/Al (100 nm). The right axis represents the corresponding short-circuit current density J_{sc} at various IQE, indicated in the graph.....	38

Figure 2.19 The two most commonly used standard spectra, AM 1.5 direct and AM 1.5 global. The global spectrum comprises the direct plus the diffuse sunlight. The difference is mainly in the shorter wavelength region since molecular scattering scales with λ^4 . Water (H ₂ O), ozone (O ₃) and carbondioxide (CO ₂) are the main absorbers of the solar radiation in Earth's atmosphere.....	39
Figure 2.20 Schematic representation of the different AM sun light spectra.....	40
Figure 2.21 Schematic representation of the different AM sun light spectra.....	41

Chapter 3 Materials and Experimental Techniques

Figure 3.1 Photographs of polymer/fullerene solar cells with (A) P/ITO anode, (B) surface-modified PEDOT:PSS anode.....	52
Figure 3.2 (A)-(E) Flow chart for the fabrication of the inverted PSCs on NiPI films. (F) The photograph of the inverted PSCs on NiPI films.....	54

Chapter 4 Chemical Formation of Palladium-free Surface-nickelized Polyimide Film for Flexible Electronics

Figure 4.1 Flow chart of formation of surface-nickelized polyimide films: (a) PI film: Pristine polyimide (b) K ⁺ / PI film: K ⁺ / PAA layer on PI film, (c) Ni ²⁺ / PI film: Ni ²⁺ / PAA layer on PI film, (d) Ni-NPs/ PI film: Ni-NPs/ PAA layer on PI film, (e) Ni / PI films: Ni/ PAA layer on PI film.....	62
Figure 4.2 ATR-FTIR absorption spectra of polyimide modified with KOH for different time.....	65
Figure 4.3 ATR-FTIR absorption spectra of (a) pristine PI film, (b) K ⁺ / PI films, (c) Ni ²⁺ / PI film, (d) Ni-NPs/ PI film, (e) Ni-NPs/ PI film-310: Ni-NPs/ PI film after annealing at 310 °C for 1hr, and (f) Ni/ PI film.....	67
Figure 4.4 XRD patterns of (a) pristine PI film, (b) Ni-NPs/ PI film-110 (annealed at 110 °C for 1 hr), (c) Ni/ PI film-110 (annealed at 110 °C for 1 hr), and (d) Ni/ PI film-310 (annealed at 310 °C for 1hr).....	69
Figure 4.5 Variation of contact angle of PI surface in the alkaline hydrolysis after treatment with KOH and then ion exchange with nickel ions.....	70
Figure 4.6 Dependence of transparency and appearance of Ni-NPs/ PI films (Ni-NPs/ PI film treated with KOH _(aq.) for X min/ NiSO _{4(aq.)} for 5 min/ NaBH _{4(aq.)} for 30 min at 50 oC) on hydrolysis time (X min) during KOH treatment: (A) 0 min, (B) 5 min, (C) 10 min, (D) 20 min, (E) 30 min, (F) 60 min, (G) 120 min.....	73

Figure 4.7 AFM photographs of nanostructured Ni-NPs/ PI films (Ni-NPs/ PI film treated with KOH(aq) for 10 min/ NiSO ₄ (aq.) for 5 min/ NaBH ₄ (aq.) for 30 min at 50 °C for various hydrolysis times with KOH treatment: (A) 0 min, (B) 5 min, (C) 30 min, (D) 60 min. (left: top-view diagram; range of z is 200 nm; right: phase diagram, range of z is 200 degree).....	75
Figure 4.8 FE-SEM images of electroless-plated nickel on Ni-NPs/ PI films (Ni-NPs/ PI film treated with KOH(aq) for 30 min/ NiSO ₄ (aq) for 5 min/ NaBH ₄ (aq) for 30 min at 50 oC) at 50 oC for (A) 0 min, (B) 2 min, (C) 4 min, (D) 6 min, (E) 10 min, (F) 15 min. White bars represent 200 nm. (left: top-view, right: tilt 45o-view). XPS spectra of Ni-NPs/ PI films. (a) Ni-NPs/ PI film-d (measured directly), (b) Ni-NPs/ PI film-a (measured after one day).....	77
Figure 4.9 TEM photographs of cross section of Ni-NPs/ PI film (Ni-NPs/ PI film treated with KOH(aq) for 10 min/ NiSO ₄ (aq.) for 5 min/ NaBH ₄ (aq) for 30 min at 50 °C). The bar represents 100 nm. The A-area and B-area are outside and inside the Ni-NPs layer, respectively.....	79
Figure 4.10 TEM photographs (left) and EDX analysis (right) of cross section of surface-nickelized PI films: A-the Ni layer, B-the Ni-NPs layer, C-PI film.....	79
Figure 4.11 Variations of contact angle of two PI sides in the alkaline hydrolysis after treatment with KOH.....	82
Figure 4.12 TEM photographs of cross section of Ni-NPs/ PI film (Ni-NPs/ PI film treated with KOH(aq) for 10 min/ NiSO ₄ (aq) for 5 min/ NaBH ₄ (aq) for 5 min/ EN solution for 10 min at 50 oC). (A) A side of PI film. (B) B side of PI film.....	83
Figure 4.13 Peel strengths of two sides of Cu/Ni/PI films and Cu with various thicknesses.	84

Chapter 5 High-Conductivity Poly(3,4-ethylenedioxythiophene):Poly(styrene sulfonate) Film for Use in ITO-Free Polymer Solar Cells

Figure 5.1 Architecture and photograph of the ITO-free polymer/fullerene solar cell.....	89
Figure 5.2 Raman spectra of PEDOT:PSS films excited using HeNe laser at 632.8 nm.....	93
Figure 5.3 SEM cross-sectional images of solvent-modified PEDOT-PSS films on glass substrates. (a) P, (b) P-ET, (c) P-ME, (d) P-DME and (e) P-EG.....	94
Figure 5.4 Topographic (A, C, E) and phase (B, D, F) images of PEDOT-PSS films (P, P-ME and P-EG, respectively) obtained with tapping-mode AFM.....	96
Figure 5.5 TEM images of solvent-modified PEDOT-PSS films. (A) P, (B) P-ET, (C) P-ME, and (D) P-EG.....	98

Figure 5.6 C(1s) core level spectra before and after heat treatment of (a) P-na, (b) P, (c) P-ET, (d) P-ME, (e) P-DME, and (f) P-EG.....	100
Figure 5.7 O(1s) core level spectra before and after heat treatment of (a) P-na, (b) P, (c) P-ET, (d) P-ME, (e) P-DME, and (f) P-EG.....	101
Figure 5.8 S(2p) core level spectra before and after heat treatment of (a) P-na, (b) P, (c) P-ET, (d) P-ME, (e) P-DME, and (f) P-EG.....	101
Figure 5.9 Schematic 3D morphological models of (A) P (top-view), (B) P (side-view), (C) P-ME (top-view), (D) P-ME (side-view), (E) P-EG (topview), (F) P-EG (side-view).....	104
Figure 5.10 Current–voltage characteristics of ITO-free polymer solar cells incorporating the various solvent-modified PEDOT:PSS films: (a) P, (b) P-ET, (c) P-ME, (d) P-DME, and (e) P-EG. All devices were measured under illumination of AM 1.5 (100 mW cm ⁻²) with active area of 0.01 cm ²	107

Chapter 6 All-Solution-Processed Inverted Polymer Solar Cells on Granular Surface-Nickelized Polyimide

Figure 6.1 Architectures of polymer solar cells: (A) standard, (B) inverted (in terms of the roles of the electrodes), and (C) inverted (in terms of the alternative processing structure).....	113
Figure 6.2 Flow chart for the formation of the patterned NiPI film. (A) PI: pristine polyimide; (B) K ⁺ /PI: K ⁺ /PAA layer on PI film; (C) Ni ²⁺ /PI: Ni ²⁺ /PAA layer on PI film; (D) Ni-NPs/PI: Ni-NPs/PAA layer on PI film; (E) NiPI: Ni/PAA layer on PI film; (F) Patterned NiPI: patterned Ni/PAA layer on PI film; (G) photograph of the patterned NiPI. (a) Alkaline hydrolysis to open imide rings; (b) cation-exchange reaction leading to the incorporation of Ni ²⁺ ions; (c) reduction of Ni ²⁺ ions by aqueous NaBH ₄ ; (d) Ni electroless plating using an EN solution; (e) patterning of Ni through photolithography.....	114
Figure 6.3 (A) Photoelectron spectrum of NiPI film. (B) XPS spectrum of NiPI surface. (C) SEM image of NiPI surface. (D) Schematic representation of the energy levels of an ITO-free inverted PSC on PI.....	120
Figure 6.4 (A) S(2p) core level spectra of P3HT:PCBM film (1:0.8 w/w) with plasma treatment for various seconds. (B) Architecture of an inverted PSC featuring an inverted sequence on NiPI as the back contact electrode. (C) Optical image of an inverted PSC on NiPI. (D) TEM cross-sectional image of an inverted PSC on	

NiPI. Scale bars, 500 nm.....	123
Figure 6.5 (a, c, e, g) Topographies (including cartoon representations) and (b, d, f, h) phase images of NiPI and TIPD-modified NiPI films. (a, b) NiPI: pristine NiPI film; (c, d) T0NiPI: TIPD (0.94 wt%) on NiPI film; (e, f) T3NiPI: TIPD (3.75 wt%) on NiPI film; (g, h) T15NiPI: TIPD (15 wt%) on NiPI film. Scale bars, 500 nm.	129
Figure 6.6 I–V characteristics of inverted PSCs under AM 1.5 illumination (100 mW cm ⁻²)	130
Figure 6.7 SEM images (Top-view) of different structure of cathodes. (A) AlPI: planar AlPI, (B) NiPI: granular NiPI. (C) Reflective UV-vis spectra of films on different structures of cathodes. (a) AlPI: planar AlPI, (b) NiPI: granular NiPI, (c) PT3/AlPI: P3HT:PCBM/TIPD(3.75 wt%)/AlPI, (d) PT3/NiPI: P3HT:PCBM/TIPD (3.75 wt%)/NiPI, (e) PT3AlPI Device: PEDOT:PSS/PT3/AlPI, (f) PT3NiPI Device: PEDOT:PSS/PT3/NiPI.....	133
Figure 6.8 (A) Reflection haze factors for different structure of cathodes and the EQE spectra of inverted PSCs on different structure of cathodes. Cartoon representations for inverted PSCs illuminated on different structure of cathodes. (B) Planar AlPI, (C) Granular NiPI.....	134
 Chapter 7 Morphological Control of CuPc and its Application in Organic Solar Cells	
Figure 7.1 Organic donor–acceptor heterojunctions: (a) planar, (b) mixed DA, (c) thermodynamically driven bulk, and (d) ideal bulk heterojunctions.....	139
Figure 7.2 SEM images of TE-grown CuPc films on (a) ITO, (b) PITO, (c) AITO (top-view), and (d) AITO (side-view) substrates. The cartoon images (a)-1~(c)-1 represent the morphologies in (a)~(c), respectively.....	142
Figure 7.3 SEM images of vertical rod-like CuPc films grown on Au substrates at thicknesses (measured using a quartz crystal microbalance) of (a) 100, (b) 200, (c) 300, and (d) 500 Å. (e) Cartoon representation of an ideal BHJ of CuPc films. All scale bars are 100 nm.....	144
Figure 7.4 GIXRD spectra of CuPc powders and films deposited on various substrates at various substrate temperatures: (a) AITO (T _{sub} = 25 °C), (b) AITO (T _{sub} = 100 °C), (c) PITO (T _{sub} = 100 °C), (d) ITO (T _{sub} = 100 °C), and (e) CuPc powders.....	145
Figure 7.5 (a) SEM (top-view) image of a thin layer of Au on an ITO substrate. (b)–(d) TEM images and (e) EDX analysis of CuPc rods deposited on the Au substrates at	

Tsub = 100 °C. (b) Bottom section of CuPc rods. (c) CuPc rods. (d) HR-TEM images of the upper section of CuPc rods.....	147
Figure 7.6 AFM images [topographic (a) and phase (b)] of the PITO surface. SEM images [top-view (c) and estimate (d)] of CuPc rod-like film on the PITO. (e) S(2p) core level spectra of the PITO surface.....	150
Figure 7.7 (A) Schematic representation of the energy levels of the devices. (B) UV–Vis spectral transmittance of fully processed solar cells incorporating various films: (a) ITO, (b) AITO, (c) rod-like CuPc (200 Å)/AITO, (d) C60 (300 Å)/CuPc:C60 (1:1) (100 Å)/ rod-like CuPc (200 Å)/AITO. (C) Cross-sectional image of the device having the structure AITO/CuPc (200 Å)/CuPc:C60 (100 Å)/C60 (300 Å)/BCP (75 Å)/Al.....	153
Figure 7.8 (A) Cartoon representations of four types of DA interfaces in solar cells. (B) J–V curves of devices possessing the configuration anode/CuPc (200 Å)/CuPc:C60 (1:1) (100 Å)/C60 (300 Å)/ BCP (75 Å)/Al under illumination (100 mW cm ⁻²), featuring various CuPc morphologies formed under various annealing temperatures.....	156

Chapter 8 Conclusions and Prospects

Figure 8.1 Schematic energy level of tandem cells on granular NiPI.....	162
---	-----

Chapter 1

Introduction

1.1 Background

Supply of energy is one of the main concerns of our society. Because of growing economy and modern lifestyle, consumption of energy rises drastically. The world's fossil energy resources are still ample for the next coming years –yet, the extraction costs for this kind of energy is still under debate. The current oil prize instability reveals the vulnerability of our economy towards higher energy prizes, not mentioning the political and economical unrest predominant in several main oil producing countries. Because our world highly depends on those supplies, there is a risk of slipping into an energy crisis someday soon. Therefore, over the past several decades, there are a lot of countries to invest large amount of capitals and time in developing the renewable sources of energy. Among the developments of power producing, the direct conversion of solar energy to electricity by photovoltaic (PV) is emerging as a leading contender for next-generation green power production. Conversion into electrical power of even a small fraction of the solar radiation incident on the Earth's surface has the potential to satisfy the world's energy demands without generating CO₂ emissions. The progress in the efficiency of research-scale PVs over the past several decades is shown in **Figure 1.1**. [1]

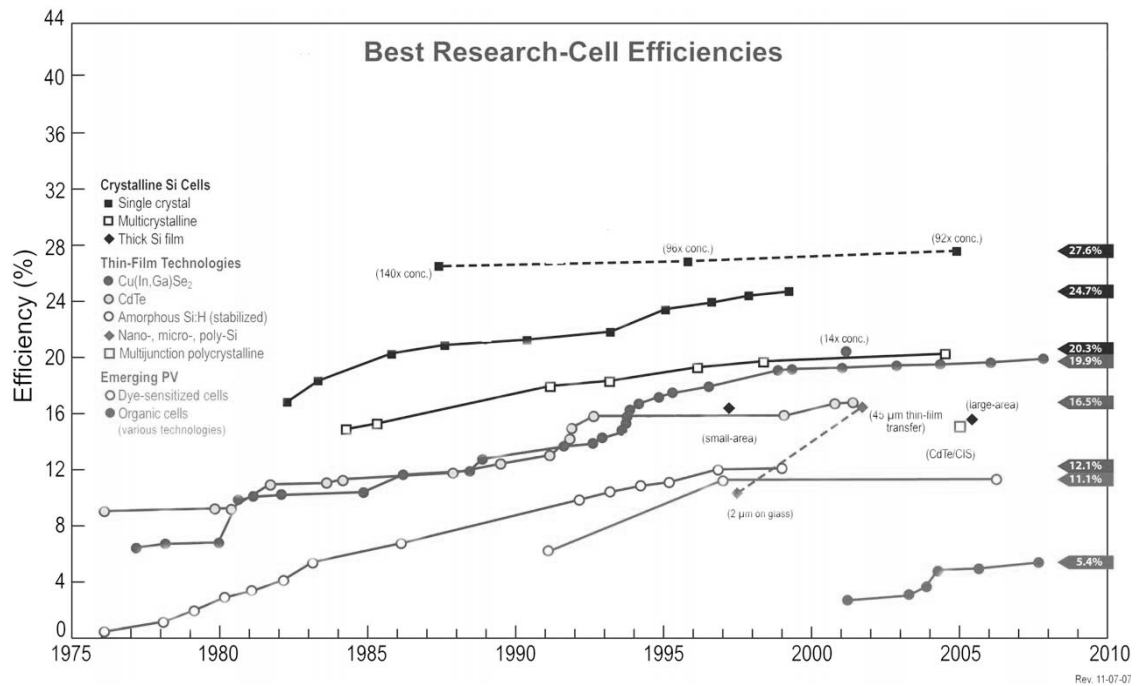


Figure 1.1 Progress of research-scale photovoltaic device efficiencies, under AM1.5 simulated solar illumination for a variety of technologies (as compiled by Larry Kazmerski, National Renewable Energy Laboratory).

Current PV technology is not yet fulfilling this promise, largely due to the high cost of the electricity produced. Although the challenges of storage and distribution should not be underestimated, a major bottleneck lies in the PV devices themselves. Improving efficiency is part of the solution, but diminishing returns in that area mean that reducing the manufacturing cost is absolutely vital, while still retaining good efficiencies and device lifetimes. Although the PV technology platforms of silicon-based PV and thin-film PV are now undergoing a rapid expansion in production and the power conversion efficiency can easily approach 15% [1], their high costs of fabrication and of raw materials have yielded limited commercial applications. Recently, the next generation PV—organic solar cells (OSCs)—could soon be playing a major role with the advantages of low-cost, large-area, lightweight and shatterproof. The challenge here is that absorbing light in an organic material produces a coulombic bound exciton that requires dissociation at a donor–acceptor heterojunction. A thickness of at least 100 nm is required to absorb the

incident light, but excitons only diffuse a few nanometres before decaying. The problem is therefore intrinsically at the nano-scale: the composite devices with a large area of internal donor–acceptor interface are needed, but where each carrier has a pathway to the respective electrode. Following this is the separation of charges which is mostly induced by the field generated from the difference in work functions of the electrodes. The following scheme shows the important processes in OSCs (Figure 1.2). At each one of these steps, recombination of the electron and hole can occur, preventing their contribution to the current. In addition to the fundamental restrictions of the device, such as how much light can be absorbed, these recombination losses limit the overall maximum efficiency of energy conversion that can be attained. So that the issues on how to overcome the problems from each step in OSCs are widely investigated.

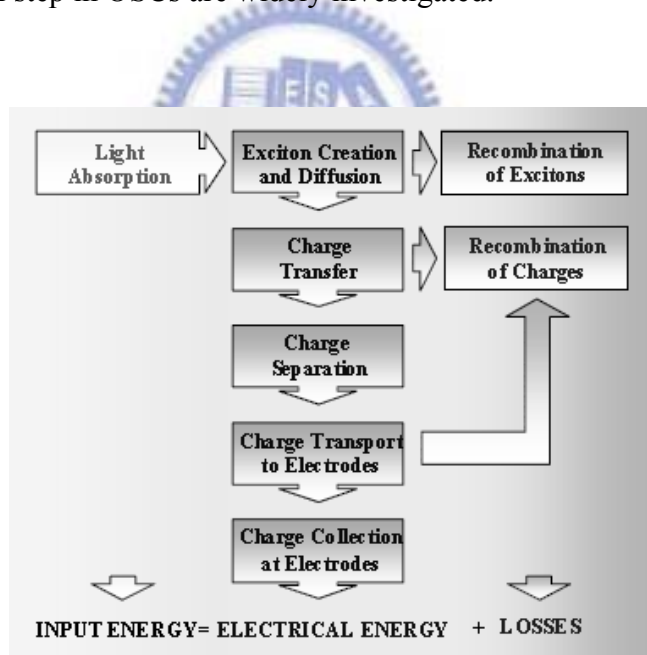


Figure 1.2 Schematic flow chart showing the important processes in organic solar cells. Recombination of excitons can be radiative or non-radiative.

Flexible electronics are increasingly being used in a number of applications which benefit from their low production cost, light weight, favorable optical and electrical properties. However, despite these advantages, the range of practical, high-volume,

applications for flexible electronics will remain limited in the future unless a number of challenges related to electrical performance and stability on flexible substrates are compared to the standard devices. Although researchers generally investigate the OSCs on rigid ITO/glass substrates, the final developing objective of OSCs is fabricated on flexible substrates to exhibit the advantages of OSCs. In the developing field of production technologies of flexible electronics, the highest productivity at lowest process costs is gained from roll-to-roll processing. The manufacture of the flexible electronics can be integrated several printing techniques (such as inkjet, screen, flexographic and gravure printings) into the roll-to-roll process to enhance the throughput of products [2-5]. Based on the previous considerations, in this thesis, I will develop several techniques of solution processes to produce the roll-to-roll suitable circuits and electrodes and apply those methods in the flexible OSCs.



1.2 Aims and Objectives

It will be demonstrated in this thesis that several investigations of key technologies of circuits and electrodes for applying in flexible electronics, especially in OSCs. In the present work, I will develop an all-solution method for fabricating thin Ni films on PI (NiPI) with high adhesion and conductivity and it will be suitable for roll-to-roll manufacturing processes in flexible printed circuits. Furthermore, I will devise a simple method to enhance the conductivity of PEDOT:PSS films through spin-coating with various surface-modified compounds, and then apply the PEDOT:PSS films as anodes to the preparation of ITO-free polymer solar cells (PSCs). The ultimate goal is to prepare all-solution-processed inverted polymer solar cells (PSCs) incorporating two solution-processed electrodes—NiPI films as cathodes and high-conductivity PEDOT:PSS films as anodes—on flexible substrates.

Another developing field of electrodes will be studied to control the morphology of active layers in the small molecular solar cells, and therefore I will investigate the rod-like CuPc structures on indium–tin oxide (ITO), PEDOT:PSS and Au substrates to demonstrate an ideal bulk heterojunction structure using the self-assembly of CuPc as the donor material and fullerene as the acceptor.

The objectives of this thesis are as follows:

- To study and review relevant literatures on surface-metalized PI films.
- To develop a simpler way to fabricate a metal thin film (as the conducting and diffusion barrier layer) on PI films, and excellent adhesion between the metal and PI phases will be obtained.
- To study and review relevant literatures on the solution-processed transparent conducting layers.

- To investigate the origin effect of conductivity enhancement of PEDOT:PSS films from the comprehensive analysis results.
- To demonstrate the ITO-free PSCs with the high-conductivity PEDOT:PSS films and understand the limits for larger area cells.
- To study and review relevant literatures on inverted PSCs and the solution-processed techniques of PSCs.
- To investigate the interface problems of fabricating inverted PSCs on NiPI films.
- To inspect the optical properties occurring in NiPI-based PSCs and recommend how to improve the performance in the next generation of PSCs.
- To study and review relevant literatures on small molecular solar cells.
- To investigate the morphological control of CuPc and its application in organic solar cells.
- To calculate the surface energy difference of PEDOT and PSS phases, and recommend how to improve the performance in the next generation of small molecular solar cells.

1.3 Brief Structures of this Thesis

This thesis comprises eight chapters. Contents of each chapter are detailed as follows:

Chapter 1 provides the background of this study, stating the reason why the study is conducted. In addition, the aims and objectives of this thesis are outlined in this chapter.

Chapter 2 is literature review of research in the field of circuits, electrodes and organic solar cells. Key area focuses on the fabrication of all-solution-processed electrodes for application of flexible printed circuits and organic solar cells (such as polymer solar cells and small molecular solar cells).

Chapter 3 is a short overview of the materials used and the experimental details that we developed for reproducible device preparation will be presented.

Chapter 4 represents the theory and formation of surface-nickelized polyimide films using a wet chemical process. This investigation will synthesize nickel nanoparticles as seeds (catalysts) and a Ni metal layer as an adhesion-promoting layer on the surface of a polyimide film, and excellent adhesion between the nickel and polyimide phases was observed. It can reduce the cost of the catalyst and simplify the process of coating the adhesion-promoting layer on the PI film.

Chapter 5 describes the goal and experiment methodology to develop a simple method for modifying the electrical conductivity of PEDOT:PSS films intended for use as electrodes in ITO-free solar cells. The high-conductivity PEDOT:PSS films could be obtained simply through spin-coating of a solvent onto pre-coated PEDOT:PSS films. We employed the comprehensive analysis results to determine the origin of the conductivity enhancement.

We found that the performance of the PPVs was related to the surface morphologies, chemical structures, and electrical conductivities of the PEDOT:PSS films. We performed a comprehensive investigation of the effects of alcoholic and ethereal solvents, including methoxyethanol, ethanol, and 1,2-dimethoxyethane, to determine the driving force for the conductivity enhancement of the PEDOT:PSS films.

Chapter 6 reports the fabrication of all-solution-processed inverted PSCs featuring granular NiPI as the cathode material (back contact electrode) on flexible substrates; combining with the techniques in chapter 4 and chapter 5, these devices have the following configuration: PI/Ni (cathode)/ titanium(diisopropoxide)bis (2,4-pentanedionate (TIPD)/P3HT:PCBM/PEDOT:PSS (anode). Furthermore, when compared to the planar structure, the improvement of absorbance of light and good haze factors was obtained for granular structure which suggests NiPI as a better back contact electrode through enhancing the light trapping and scattering in inverted PSCs.

Chapter 7 reports the organic photovoltaic (OPV) cells possessing an ideal bulk heterojunction (BHJ) structure using the self-assembly of copper phthalocyanine (CuPc) as the donor material and fullerene (C_{60}) as the acceptor. The variable self-assembly behavior of CuPc on a diverse range of substrates (surface energies) allowed us to control the morphology of the interface and the degree of carrier transportation within the active layer.

Chapter 8 draws conclusions from the results and discussions. In addition, some prospects are made for future research.

Chapter 2

Literature Review

2.1 Polymer Substrates

Polymer has attracted a great deal of concern in the past few years because polymers can be applied to the manufacturing of various electronic and display devices. There have been extensive research activities on flexible electronics based on polymer materials. Flexible printed circuit board (FPCB), packaging, and flexible organic solar cells (OSCs) based on all polymeric materials or partial employment of polymeric materials have been developed due to low cost and ease of fabrication. It is expected that micro-electro-mechanical systems (MEMS) and semiconductor devices as well as flexible displays can be fabricated on flexible substrate for many applications. It is because that flexible electronics offer substantial coupled rewards in terms of being able to develop electronics that are thinner, lighter, robust and can be rolled away when not required. In addition, plastic-based substrates coupled with the recent developments in solution deposition and inkjet printing for laying down electronic materials open up the possibility of cost-effective processing in high volumes using roll-to-roll processing. For instance, polymer solar cells can be created using roll-to-roll manufacturing process. The roll-to-roll process is the process in which transparent electrode, printed active material, primary electrode and substrate are printed onto transparent packaging to make a solar panel. This manufacturing process is inexpensive, environmental friendly, and simple. The schematic diagram of roll-to-roll process of OSC modules is shown in Figure 2.1.

Flexible electronics can be built on metal foil, very thin glass coated with a polymer

and a variety of plastics. Therefore, to replace glass, a plastic substrate needs to be able to offer the properties of glass, i.e. clarity, dimensional stability, thermal stability, barrier, solvent resistance, low coefficient of thermal expansion (CTE) coupled with a smooth surface. This section will focus only on plastic films that have been given serious consideration as flexible substrates for flexible electronics. Based on different process temperatures and product demands, the suitable polymer substrate can be selected in further applications. The main candidates are shown in **Table 2.1** [6].

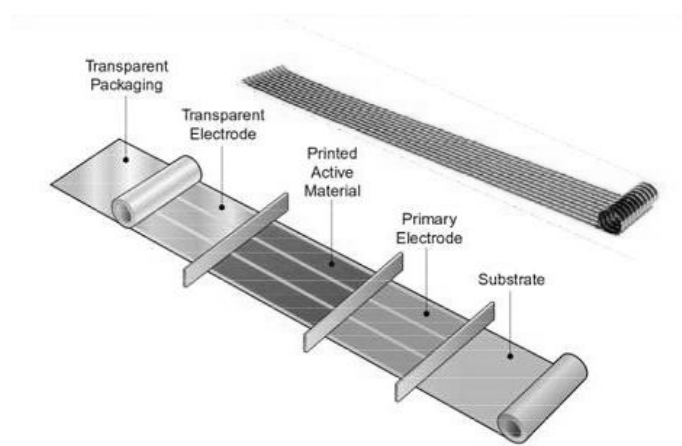


Figure 2.1 Schematic diagram of roll-to-roll process of OSC modules (from Konarka Technologies, Inc.).

Table 2.1 Basic properties of polymers used for base substrate. (Note: PET: Polyethylene terephthalate; PEN: Polyethylene naphthalate; PC: Polycarbonate; PES: Polyethersulphone; PAR: Polyarylate; PCO: Polycyclic olefin; PI: Polyimide.)

	PET	PEN	PC	PES	PAR	PCO	PI
T_g (°C)	~80	~120	~145	~220	~330	~320	~350
CTE (ppm/°C)	15	13	60-70	54	53	74	17~13
Transmission at 400-700 nm (%)	>85	>85	>90	90	90	91.6	yellow
Water absorption (%)	0.14	0.14	0.2-0.4	1.4	0.4	0.03	1.8
Young's Modulus (GPa)	5.3	6.1	1.7	2.2	2.9	1.9	2.5
Tensile strength (MPa)	225	275	60	83	100	50	231
Morphology	Biaxially oriented Semicrystalline			Amorphous			

2.2 Flexible Printed Circuit Boards

Recently, polyimide (PI) films have become generally used components for flexible electronic devices because they exhibit high glass transition temperatures, low surface roughness, low coefficients of thermal expansion (CTE), and high chemical resistance under typical fabrication conditions. Therefore, metallization of polyimide for metal lines has therefore been the subject of intense study for FPCB, [7-11] with various trials having been conducted in incorporating metal wiring layers onto dielectric polyimide, with the aim of developing high performance microchips. The base materials of FPCB and other soft electronics are copper on polyimide with or without adhesive. The former is called the three-layer mode (3L-FPCB: metal/adhesive/PI), while the latter is the two-layer mode (2L-FPCB: metal/PI). The development of FPCB with smaller line widths and increased wire density is based on the two-layer (Figure 2.2). For example, one common approach is photolithography utilizing a photoresist combined with metal coating on a polyimide substrate in an additive (area-selective deposition of metals by physical and chemical means) and/or subtractive (etching of preformed metal films) manner [7-11]. Another approach is electroless deposition combined with simultaneous or alternating laser irradiation [12, 13]. However, this process sometimes has undesired defects in the pattern due to laser-induced decomposition of the polyimide substrate. The development of a facile, direct metallization process with which metallic patterns could be directly formed onto polyimide substrates is challenging. In addition, device fabrication processes require high reliability in terms of the adhesive strength between the thin metal films and the underlying substrate. To achieve sufficient adhesion between the metal film and polyimide, most conventional metallization processes employ etching of the polyimide surface (typically several micrometers in surface roughness), leading to an increase in contact area to provide good adhesion through mechanical interlocking (anchoring). [7-11] However,

as the dimensions of pattern details drop to the several micrometer and submicrometer scales, micrometer scale anchoring is not suitable for reliable adhesion. Thus, a new adhesion method is required for realizing future generations of electronic devices.

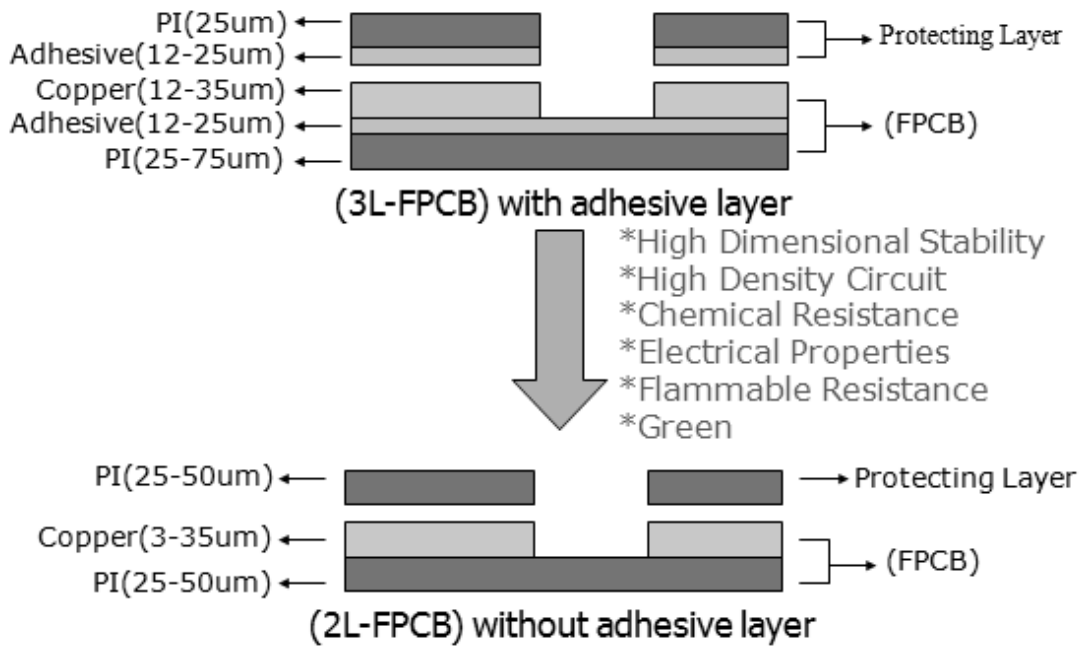


Figure 2.2 Development of flexible printed circuit boards.

Recently, Kensuke and Hidemi *et al.* reported a novel surface-modification based method for the metallization of polyimide surfaces. [14-18] The method relies on a simple alkali treatment of the bare polyimide films to introduce the active components of an ion exchange reaction (carboxylic acid groups) [19, 20] and subsequent loading of metal ions into the modified layers by ion exchange reactions. Fabrication of the metallic thin films or patterns was previously achieved through chemical reduction using NaBH_4 aqueous solution [14] and ultraviolet (UV)-light-induced photochemical reduction of the adsorbed metal ions using preadsorbed TiO_2 nanocrystals as a photocatalyst on the polyimide surface. [16] Although this process allows the polyimide surface to be metallized directly, the formation of metallic thin films is only achieved through the use of a photoresist or catalyst, and the interfacial structure between metal thin films and the underlying

polyimide is difficult to control. It is suggested that the diffusion of metal ions during the reduction process plays a key role in determining the metal/polyimide interfacial structures. The following schematic diagram showed that mechanism for direct metallization of a polyimide film surface using an ion-doped precursor layer (Figure 2.3). [18] Furthermore, when using this surface metalized Cu/PI films to apply in FPCB, the copper film side and the polyimide substrate side of the samples obtained can achieve an average adhesive strength of 1.00 kg fcm^{-1} (Figure 2.4).



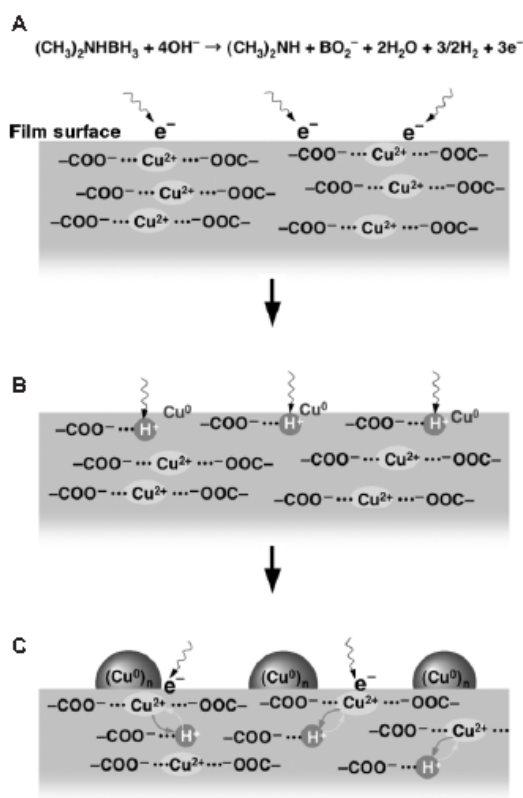


Figure 2.3 Schematic diagram of the mechanism for direct metallization of a polyimide film surface using an ion-doped precursor layer. (A) Reduction of copper ions via self-oxidative decomposition of DMAB in aqueous solution. (B) Formation of copper atoms followed by protonation of the remaining carboxylate anion groups. (C) Ion-exchange reaction between protons and copper ions through the generation of a concentration gradient of these ions in the precursor layer, and further reduction of copper ions at the film surface.

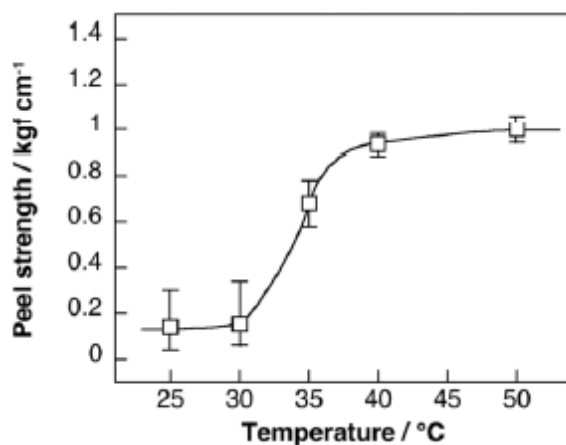


Figure 2.4 Effect of DMAB reduction temperature on the peel strength of the resulting copper film formed on the surface-modified polyimide film.

2.3 Electrode Materials

In the electronics, the work function (WF) of the electrode materials is very important since it determines together with the LUMO/HOMO and Fermi-level of the semiconductor whether the electrode forms an ohmic or a blocking contact for the respective charge carrier (holes in valance band, electrons in conducting band). In Table 2.2, the periodic table of the elements is listed with its values of WF [21]. The values in Table 2.2 are valid only for poly-crystalline materials. However, many numbers for single crystals which depend on its crystallographic orientation have also been reported [21]. The general electrode materials can be categorized as metal, inorganic semiconductor, conducting polymer and carbon nanotube (CNT) materials. Common metal electrode materials for the electron collecting contact (low WF required) of organic solar cells are Al, Ca, Ag whereas for the hole collecting contact high WF materials like Au are preferred. If the metal materials are used to apply in flexible printed circuits (FPC), the conductivity and adhesion properties of circuits are the major issues. The metals for FPC are usually selected Cu, Ag, Au (high conductivity) as the electron conduction layers and Ni, Cr, Ti as the adhesion-promoting layers [22, 23]. While indium tin oxide (ITO) materials are usually used as transparent conducting layer, which is a degenerated semiconductor comprising a mixture of In_2O_3 (90%) and SnO_2 (10%) with a band gap of 3.7eV and a Fermi-level between 4.5 and 4.9eV is widely used. The large band gap allows no absorption of wavelengths longer than about 350nm. Unfortunately, the high cost of high-quality ITO and its lack of flexibility can limit the applications of electronics incorporating it as an anode material; the limited supply of indium and the transparency of ITO toward visible light are additional problems. Recently the ITO-free conducting materials, such as PEDOT:PSS and CNT films, are widely investigated to replace ITO in the future. An additional advantage of PEDOT:PSS is that it can be manufactured through

the solution processes. CNT network films appear to be a suitable alternative: they can be prepared through solution processing, and they exhibited high conductivity and flexibility [24, 25]. Figure 2.5 shows the transparency and conductivity of single-walled carbon nanotube network films [24]. Furthermore, the stability of devices fabricated on the SWNT/PET films is much greater than devices on ITO/PET during simple bending tests. The PSCs with SWNT network films as electrode could be folded over (inducing compressive or tensile strain) down to radii of curvature of ~ 5 mm with no degradation in power efficiency and radii of ~ 1 mm with a 20-25 % loss in efficiency. Such CNT-based devices do, however, have their problems. For example, the nature of the transparent single-wall carbon nanotube (SWNT) network films is not always well defined; typically, SWNT films are mixtures of metallic and p-doped nanotubes. In addition, it is necessary to add PEDOT:PSS to adjust the work function of the SWNTs and to avoid shorting of the device. Therefore, recently the PEDOT:PSS materials are widely investigated to enhance the conductivity and then used to apply in ITO-free devices. Some transparent conducting materials are listed with their WF, sheet resistance and references in Table 2.3.

Table 2.2 WF of the elements. The numbers refer to the WF (eV) of the elements in polycrystalline form.

IA	IIA	IIIB	IVB	VB	VIB	VIIIB		VIII		IB	IIB	IIIA	IVA	VA	VIA
Li 2.9	Be 4.98											B 4.45	C 5.0	N -	O -
Na 2.75	Mg 3.66											Al 4.28	Si 4.85	P -	S -
K 2.30	Ca 2.87	Sc 3.5	Ti 4.33	V 4.3	Cr 4.5	Mn 4.1	Fe 4.5	Co 5.0	Ni 5.15	Cu 4.65	Zn 4.33	Ga 4.2	Ge 5.0	As 3.75	Se 5.9
Rb 2.16	Sr 2.59	Y 3.1	Zr 4.05	Nb 4.3	Mo 4.6	Tc -	Ru 4.71	Rh 4.98	Pd 5.12	Ag 4.26	Cd 4.22	In 4.12	Sn 4.42	Sb 4.55	Te 4.95
Cs 2.14	Ba 2.7	La 3.5	Hf 3.9	Ta 4.25	W 4.55	Re 4.96	Os 4.83	Ir 5.27	Pt 5.56	Au 5.1	Hg 4.49	Tl 3.84	Pb 4.25	Bi 4.22	Po -
Fr -	Ra -	Ac -	Th 3.4	Pa -	U 3.63										
			Ce 2.9	Pr -	Nd 3.2	Pm -	Sm 2.7	Eu 2.5	Gd 3.2	Tb 3.0	Dy -	Ho -	Er -	Tm -	Yb -

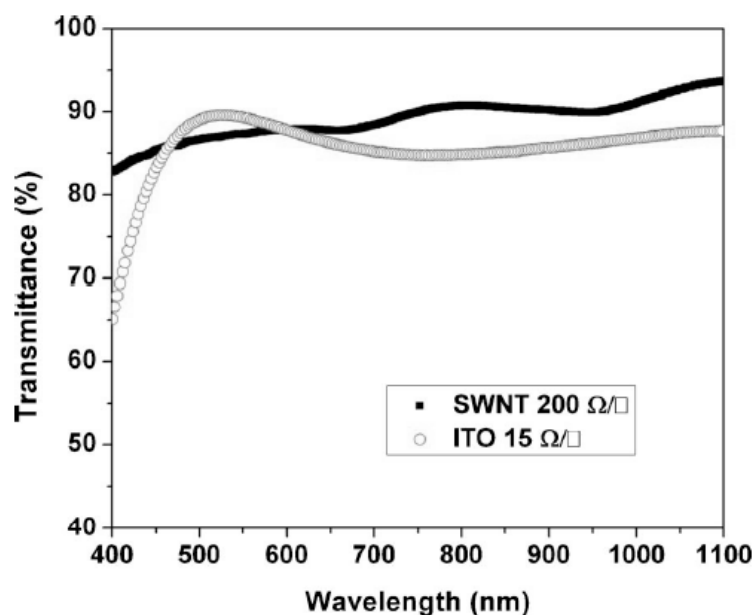


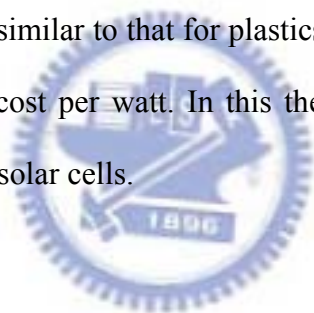
Figure 2.5 Transparency of a 30-nm-thick nanotube film with 200 Ω /sq. sheet resistance, together with the transparency of ITO on glass 15 Ω /sq.

Table 2.3 WF and sheet resistance of the transparent conducting electrode materials. (Note: Indium tin oxide (ITO); Fluorine-doped tin oxide (FTO); Aluminum-doped zinc oxide (AZO); poly(3,4-ethylenedioxythiophene)-poly(styrene-sulfonate) (PEDOT:PSS); vapor-phase polymerization poly(3,4-ethylenedioxythiophene)- Fe(III)-tosylate (VPP-PEDOT-Tos); Single-walled carbon nanotube (SWNT); Multi-walled carbon nanotube (MWNT).)

Materials	WF (eV)	Sheet Resistance (Ω /sq.)	References
ITO	4.4-4.9	5-10	[26, 27]
FTO	4.8	10	[28]
AZO	5.2	150	[29]
PEDOT:PSS	5.2-5.3	800-3000	[30]
VPP-PEDOT-Tos	4.3	20-60	[31]
SWNT	5.1	50-110	[24, 25, 32]
MWNT	5.0	900-2500	[32, 33]

2.4 Organic Solar Cells

Organic solar cells (OSCs) represent a rapidly emerging device technology with the potential for low-cost non-vacuum-processed devices. The key is that these devices combine the small molecular [34-36], polymer [37-40], organic-inorganic hybrid solar cells [41], and dye-sensitized solar cells [42-44]. In each type of OSCs the efficiency is limited by the absorption coefficient as a function of wavelength, the probability of excitation dissociation into mobile charge carriers, the transport of those charges to the anode and cathode, and the collection of the carriers at the interfaces of electrode and organic phases. Although the excitonic mechanism is different from the conventional PV mechanism, the theoretical efficiency is the same as for conventional semiconductor devices, with a cost structure similar to that for plastics processing, leading to the potential for significant reductions in cost per watt. In this thesis, I focus on the investigation of polymer and small molecular solar cells.



2.4.1 Principle of Operation

To understand the rectifying behavior of an intrinsic (nondoped) semiconductor device in the dark, the MIM (metal-insulator-metal) model is useful [45]. In Figure 2.6, a semiconductor, sandwiched between two metal electrodes with different work functions is depicted for several situations. The metals are represented by their Fermi levels, whereas for the semiconductor the valence and conduction bands, corresponding to the molecular LUMO (lowest unoccupied molecular orbital) and the HOMO (highest occupied molecular orbital) levels, are shown. In Figure 2.6(a), there is no voltage applied (i.e., short-circuit conditions). Hence, there is no net current flowing in the dark, and the built-in electric field resulting from the difference in the metals' work functions is evenly distributed throughout the device. Under illumination, separated charge carriers can drift in

this electric field to the respective contacts: the electrons move to the lower work function metal and the holes to the opposite. The device then works as a solar cell. In Figure 2.6(b), the situation is shown for open circuit conditions, also known as “flat band condition.” The applied voltage is called the open circuit voltage V_{oc} , which corresponds in this case to the difference in the metals’ work functions and balances the built-in field. As there is no net driving force for the charge carriers, the current is zero. In Figure 2.6(c) the situation is shown for an applied reverse bias and only a very small injected dark current j_0 can flow. Under illumination, the generated charge carriers drift under strong electric fields to the respective electrodes and the diode works as a photodetector. If a forward bias larger than the open circuit voltage is applied [Figure 2.6(d)], the contacts can efficiently inject charges into the semiconductor. If these can recombine radiatively, the device works as a LED. The asymmetric diode behavior results basically from the different injection of the two metals into the HOMO and LUMO levels, respectively, which depends exponentially on the energy barrier between them.

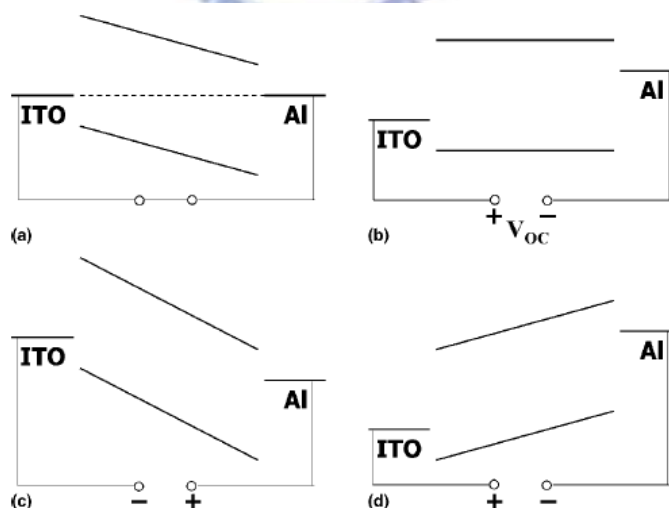


Figure 2.6 Metal-insulator-metal (MIM) picture of organic diode device function. (a) Closed circuit condition: under illumination photogenerated charges drift toward the contacts. (b) Flat band or open circuit condition: the current becomes zero. (c) Reversed bias: photogenerated charges drift in strong electric fields, the diode operates as a photodetector. (d) Forward bias larger than V_{oc} : the injection increases and the diode opens up.

Efforts to optimize the performance of polymer and small molecular solar cells should find their basis in the fundamental mechanism of operation. Figure 2.7 illustrates the mechanism by which light energy is converted into electrical energy in the devices. The energy conversion process has six fundamental steps in the commonly accepted mechanism [46]:

- (1) Absorption of light: The fraction of absorbed photons is a function of the absorption spectrum, the absorption coefficient, the absorbing layer thickness, and of internal multiple reflections at, for example, metallic electrodes.
- (2) Generation of excitons: To achieve a high efficiency of charge generation, the active material in the solar cells should absorb as large a part of the solar light as possible. Upon absorption of a photon, an exciton is created in the active layer.
- (3) Diffusion of the excitons: Ideally, all photoexcited excitons should reach a dissociation site. Since such a site may be at the other end of the semiconductor, their diffusion length should be at least equal the required layer thickness (for sufficient absorption), otherwise they recombine and photons were wasted. Exciton diffusion ranges in polymers and pigments are typically around 10 nm. However, some pigments like perylenes are believed to have exciton diffusion lengths of several 100 nm.
- (4) Dissociation of the excitons with generation of charge: Charge dissociation is known to occur at organic semiconductor/metal interfaces, impurities (e.g. oxygen) or between materials with sufficiently different electron affinities (EA) and ionisation potentials (IA). In the latter one material can than act as electron acceptor (A) while the other keeps the positive charge and is referred to as electron donor (D) - since it did actually donate the electron to A. If the difference in IA and EA is not sufficient, the exciton may just hop onto the material with the lower bandgap without splitting up its charges. Eventually it will recombine without contributing charges to the photocurrent.

- (5) Charge transport: The transport of charges is affected by recombination during the journey to the electrodes - particularly if the same material serves as transport medium for both electrons and holes. Also, interaction with atoms or other charges may slow down the travel speed and thereby limit the current.
- (6) Charge collection: In order to enter an electrode material with a relatively low workfunction (e.g. Al, Ca) the charges often have to overcome the potential barrier of a thin oxide layer. In addition, the metal may have formed a blocking contact with the semiconductor so that they can not immediately reach the electrodes.

The elementary steps involved in the pathway from photoexcitation to the generation of free charges are shown in Figure 2.8. [47, 48] The processes can also occur in an analogous fashion in the case of an excited acceptor, and the details of these mechanistic steps have been described extensively in the literature. [48] The key point is that electron transfer is not as simple as depicted in Figure 2.7. The process must be energetically favorable to form the geminate pair in step 3 of Figure 2.8 and an energetic driving force must exist to separate this Coulombically bound electron-hole pair.

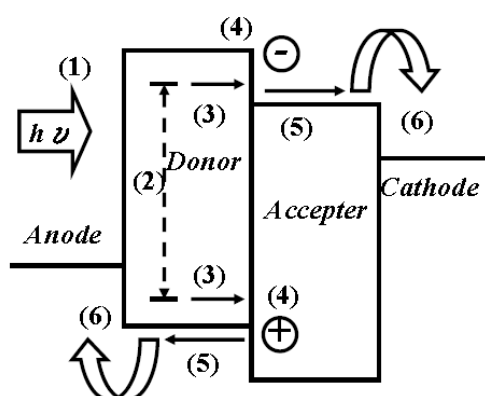


Figure 2.7 Schematic representation of general excitonic mechanism for photoenergy conversion in organic solar cells.

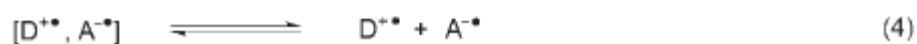


Figure 2.8 Schematic representation of elementary steps in the process of photoinduced charge separation for a donor (D) and an acceptor (A): (1) Photoexcitation of the donor; (2) diffusion of the exciton and formation of an encounter pair; (3) electron transfer within the encounter pair to form a geminate pair; (4) charge separation.

2.4.2 Built-in Potential

When applying the metal-insulator-metal (MIM) model to organic bulk heterojunction devices, the built in potential in organic semiconductor devices arises from the WF difference of the anode and cathode [49]. The schematic diagrams of built-in potential in metal/polymer/metal structures in Figure 2.9. However, even an extended MIM model was found to be insufficient for a complete explanation of the V_{oc} of bulk-heterojunction solar cells. Therefore, the effects of photocarrier distributions and chemical potential difference of energy level offsets at interfaces also require consideration in OSCs [50]. Based on the previous considerations, Markus *et al.* devised a simple relation between the energy level of the highest occupied molecular orbital (HOMO) of the polymer and the V_{oc} is derived [51], which is used to estimate the maximum efficiency of bulk-heterojunction solar cells. The results presented here can be used as a guideline for the selection and synthesis of new active materials for bulk-heterojunction solar cells. In Figure 2.10 the open-circuit voltage of different bulk-heterojunction solar cells is plotted versus the oxidation potential of the conjugated polymers used in these devices. Figure 2.10 demonstrates that for several bulk-heterojunction solar cells, a linear relation between V_{oc} and the conjugated polymer

oxidation potential is found; the open-circuit voltage of a conjugated polymer–PCBM solar cell can be estimated by

$$V_{oc} = (1/e)(| E^{Donor}HOMO | - | E^{PCBM}LUMO |) - 0.3 \text{ V}$$

where e is the elementary charge and using -4.3 eV for the PCBM lowest occupied molecular orbital (LUMO) energy. The V_{oc} and the built-in potential V_{BI} are determined by the difference between the HOMO of the donor and the LUMO of the acceptor. It is trivial to note that this is the theoretical maximum value for the V_{BI} in bulk-heterojunction systems. As discussed above and shown in Figure 2.10, deviations between the theoretical maximum V_{BI} and the V_{oc} on the order of 0.3 V are found. In Figure 2.11, the current–voltage curve of a poly(3-hexylthiophene) (P3HT)/PCBM bulkheterojunction solar cell acquired in the dark (solid line) and the idealized field-driven photocurrent (dotted line) are plotted. The open-circuit voltage of the solar cell is defined as the voltage which compensates the current flow through the external circuit (indicated by the vertical line in Figure 2.11). Figure 2.11 shows that a reduction of V_{oc} is caused by the dark current–voltage curve of the diode, which is determined by the ideality factor n and the reverse dark current I_0 of the diode. This loss has been found to be typically on the order of 200 mV . In addition, a smaller part of the V_{oc} loss ($\sim 100 \text{ mV}$ or less) originates from the fact that the photocurrent in bulk-heterojunction devices is dominantly field-driven. The open-circuit voltage depends on the slope ($= \mu\tau/d^2$) of the field-driven current around V_{BI} , where μ is the charge-carrier mobility, τ is the charge-carrier lifetime, and d is the active-layer thickness. A steeper slope moves the V_{oc} closer to V_{BI} , which is typically observed for thin-film devices where the electric field is maximized across the active layer.

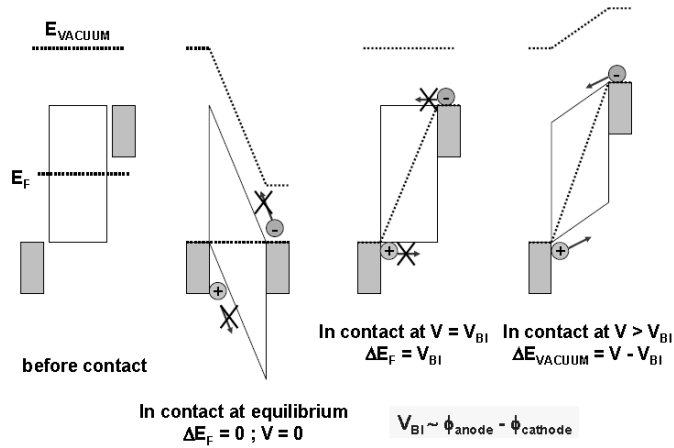


Figure 2.9 Schematic diagrams of built-in potential in metal/polymer/metal structures.

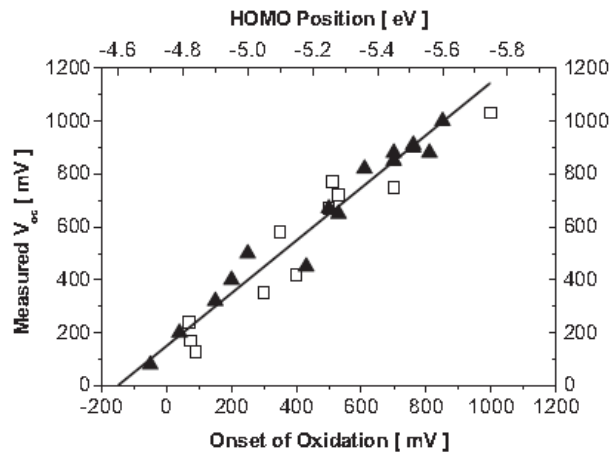


Figure 2.10 Open-circuit voltage (V_{oc}) of different bulk-heterojunction solar cells plotted versus the oxidation potential/HOMO position of the donor polymer used in each individual device.

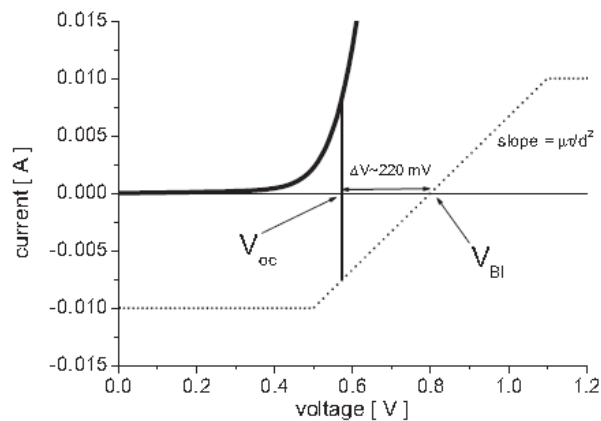


Figure 2.11 Current–voltage curve of (P3HT)/PCBM solar cell measured in the dark (solid line) and field-driven photocurrent (dotted line). The built-in potential V_{BI} is given by $E_{LUMO}(\text{PCBM})$ minus $E_{HOMO}(\text{P3HT})$ ($-4.3 \text{ V} - (-5.1 \text{ V}) = 0.8 \text{ V}$).

2.4.3 Excitons in Organic Materials

The binding energy (E_b) of excitons in organic semiconductors—in particular for conjugated polymers like PPV and its derivatives—has been subject to intense debates over the past decade. E_b values ranging from very small [52] over intermediate values (around 0.4 eV) [53-55] to very high (up to 1 eV) [56] have been proposed. As a consequence, the energy levels of the exciton are separated from the conduction band (CB) and valance band (VB) by less than about 0.2 eV which have been neglected in all band energy diagrams since the bandgaps of the materials used are between 1 and 2 eV. However, a clear offset between the HOMO and LUMO levels of the D/A material is still required for the exciton to dissociate at room temperature. In the following we give a brief description of different types of excitons (Figure 2.12):

- (a) Frenkel exciton: The electron hole pair is confined to not more than one molecular unit [57, 58].
- (b) Wannier-Mott exciton: The distance between electron and hole is much greater than the spacing between unit cell (here molecular units) [59]. Their energy levels can be described as hydrogen-like bound states, calculated with a reduced effective mass.
- (c) Charge transfer exciton: The exciton extends over only a few adjacent molecular units [60].
- (d) Inter-chain excitons: This term is used for polymeric semiconductors to indicate that the constituent charges are located on different polymer chains. It can be regarded as a charge transfer exciton.
- (e) Intra-chain excitons: This term also refers to polymeric semiconductors to indicate that the constituent charges are located on the same polymer chain. It is believed that intrachain excitons represent the main species that is formed after photoexcitation in conjugated polymers [61-63].

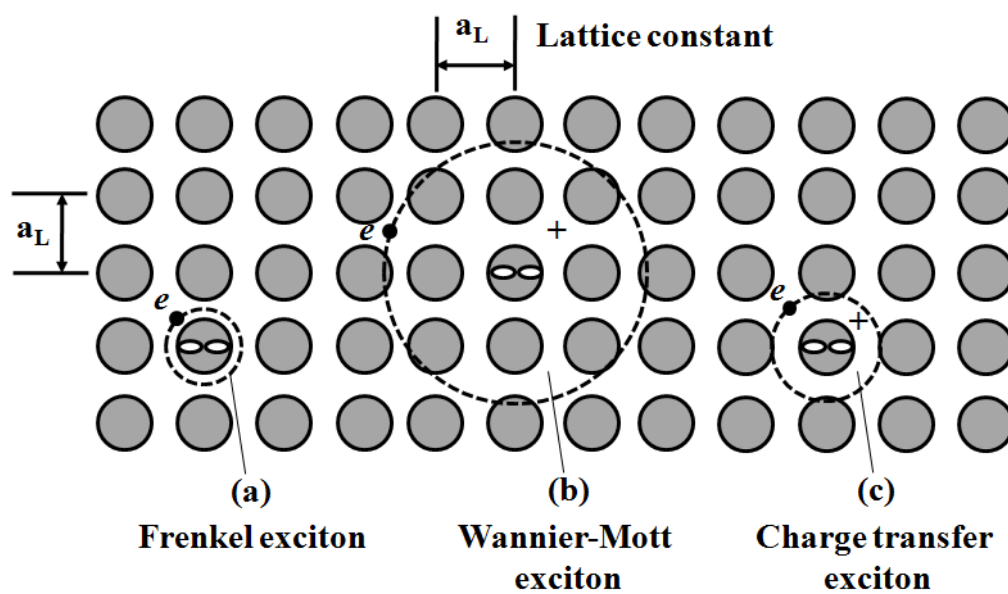


Figure 2.12 Schematic diagrams of different types of excitons in organic semiconductors.



2.4.4 Conjugated Materials for Polymer Solar Cells

Figure 2.13 shows some commonly used conjugated polymers in PSCs [64-67]. Three important representatives of hole-conducting donor type polymers are listed as below: MDMO-PPV: (poly[2-methoxy-5-(3,7-dimethyloctyloxy)]-1,4-phenylenevinylene); P3HT: (poly(3-hexyl -thiophene-2,5-diyl)); PFB: (poly(9,9'-dioctylfluorene-co-bis-N,N'-(4-butyl -phenyl)-bis -N,N'-phenyl-1,4-phenyl-enediamine)). Figure 2.13 also shows together with electron-conducting acceptor polymers like CN-MEH-PPV (poly-[2-methoxy-5-(2'-ethyl -hexyloxy)-1,4-(1-cyanovinylene)-phenylene) and F8BT (poly(9,9'-dioctylfluorene-co -benzothia-diazole) and a soluble derivative of C₆₀, namely PCBM (1-(3-methoxy -carbonyl)-propyl-1-phenyl[6,6]C₆₁).

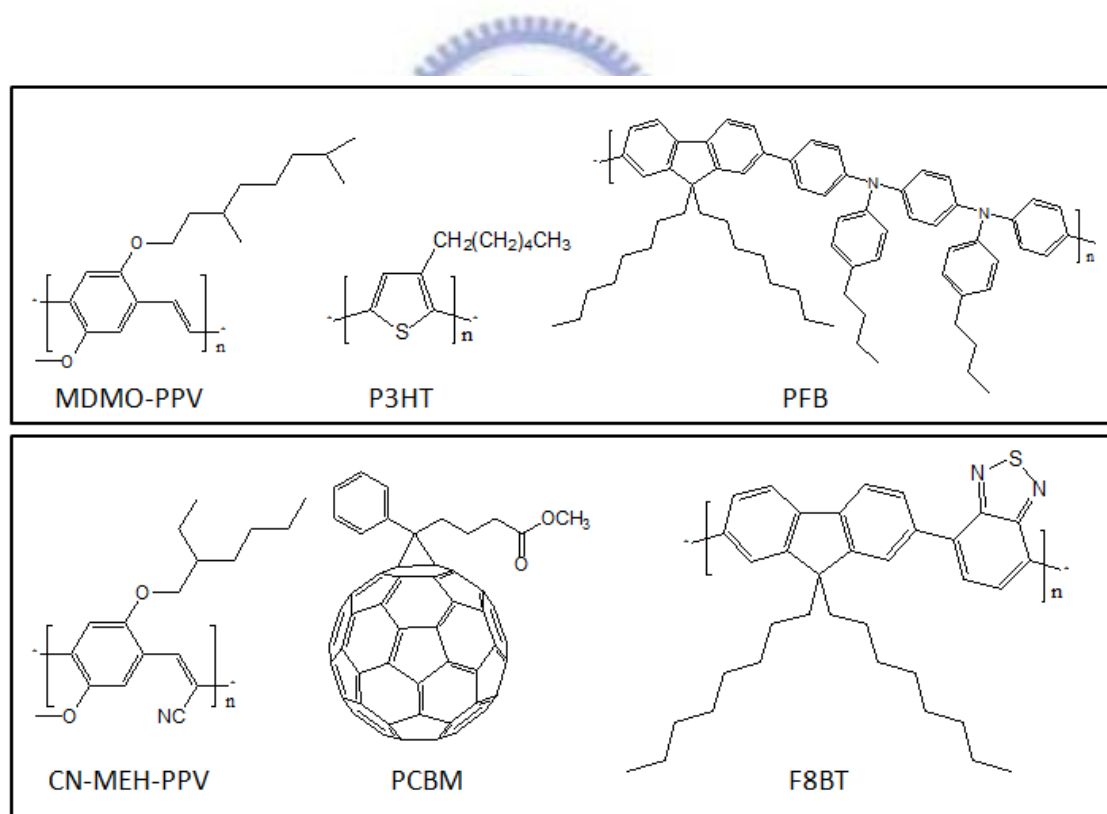


Figure 2.13 Several solution processible conjugated polymers and a fullerene derivative used in organic solar cells. Upper row: the *p*-type holeconducting donor polymers MDMO-PPV, P3HT and PFB. Lower row: the electronconducting acceptor polymers CN-MEH-PPV and F8BT and a soluble derivative of C₆₀, PCBM (1-(3-methoxycarbonyl) propyl-1-phenyl[6,6]C₆₁).

2.4.5 Small Molecular Materials for Organic Solar Cells

Figure 2.14 shows several commonly used small molecular materials in OSCs [68-72]. Five important materials of hole-conducting donor type small molecular structures are listed as below: Zinc phthalocyanine (ZnPc); Copper phthalocyanine (CuPc), N,N'-dimethylperylene-3,4,9,10-dicarboximide (Me-PTCDI); Pentacene; Perylene-3,4,9,10-tetracarboxylic dianhydride (PTCDA). The electron-conducting materials are commonly used with fullerene (C₆₀), naphthalene tetracarboxylic dianhydride (NTCDA) and 1,4-diamino-anthraquinone (1,4-DAAQ). The exciton blocking layer is general used with 2,9-dimethyl-4,7-diphenyl-1,10-phenanthroline (BCP).

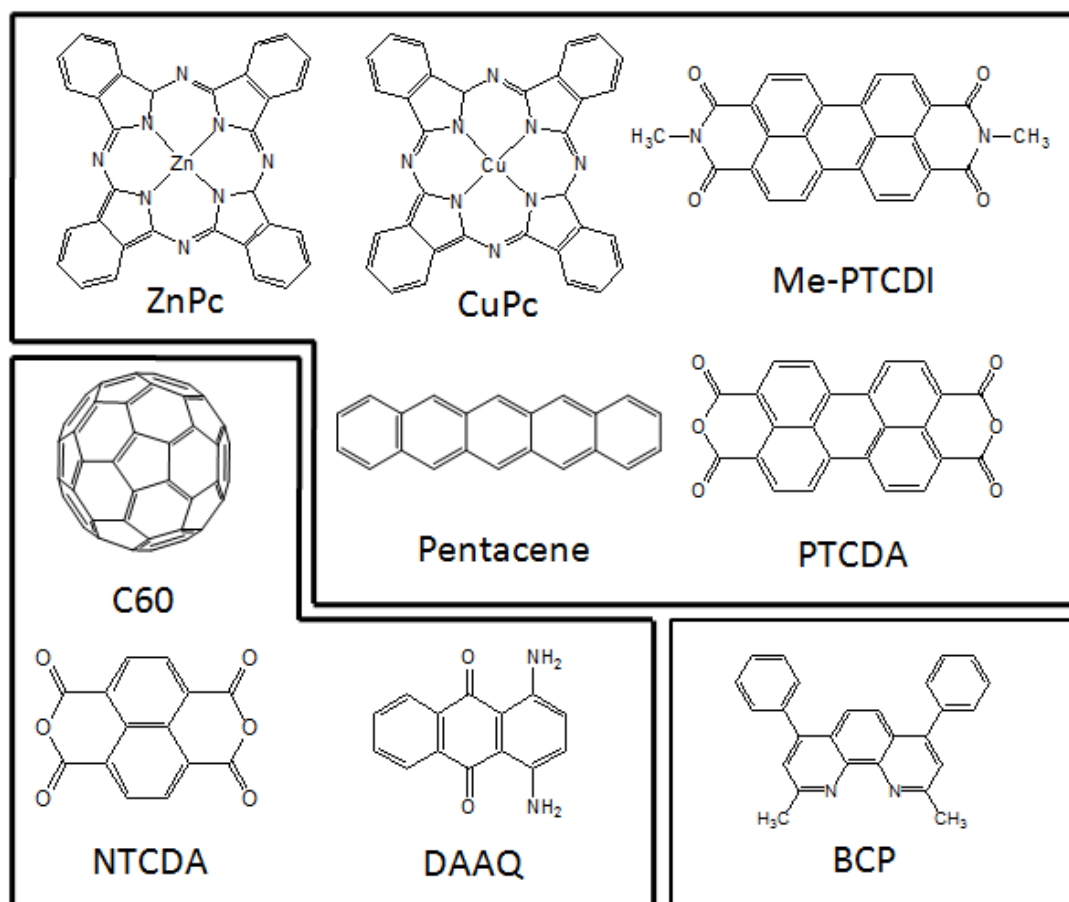


Figure 2.14 Several small molecular materials used in organic solar cells. Donor (p-type) materials: ZnPc, CuPc, Me-PTCDI, Pentacene and PTCDA. Acceptor (n-type) materials: C₆₀, NTCDA and DAAQ. Exciton blocking material: BCP.

2.5 Device Architectures for Organic Solar Cells

Photovoltaic devices based on a single layer of polymer have displayed monochromatic power conversion efficiencies below 0.1% and quantum efficiencies below 10% at low light intensities [Figure 2.15(a)] [73]. Because of the low exciton diffusion length in polymers, which are ~ 20 nm, generation of charge carriers is unlikely above a distance of greater than ~ 20 nm from the electrode. In order to create more interfaces for charge separation, bilayer devices can be constructed from a hole-transporting and an electron-transporting layer [Figure 2.15(b)]. An additional advantage of bilayer devices is that the transport of charges in two separate materials reduces the probability of recombination and the transport properties of the individual carriers can be optimized separately [74]. With the optimization of the layer thicknesses, quantum efficiencies of 23% have been reached for devices with a layer of C60 and a derivative of polythiophene [74]. However, the best devices [bulk heterojunction (BHJ) devices] so far have been fabricated with homogeneous blends of materials in which the interfaces are distributed throughout the bulk of the film [Figure 2.15(c)]. The presence of a charge transfer interface every several nanometers is the main reason why blend devices are significantly more efficient in harnessing light than single and bilayer devices. The concentration of the components in the blend is chosen to be above the percolation threshold of both components such that there are continuous pathways for the transport of both the electron and hole. Efficient charge transfer has been demonstrated in blends of poly(2-methoxy-5-(2'-ethyl-hexyloxy)-p-phenylene vinylene) (MEH-PPV) polymer and soluble derivatives of C60 [75]. In these films the quenching of the polymer photoluminescence is by a factor 10^3 compared to polymer only films, indicating that excitons have undergone either non-radiative decay or charge transfer. The presence of charged species in the photoinduced absorption spectrum attributable to a polymer cation

and a C₆₀ anion is clear evidence for charge transfer [76]. Microphase separation of the C₆₀ within MEH-PPV aids in the transport of electrons through the creation of C₆₀ pathways. Such devices have demonstrated the best solar power conversion efficiency of any polymeric device at 2.5% and peak quantum efficiency of 50% [77, 78]. Another very efficient structure is that of a modified bilayer structure in which there is a small amount of the opposite materials dispersed in each film [Figure 2.15(d)]. In this way, a large interfacial area is created and the carriers are guaranteed passage to the appropriate electrode by the presence of continuous electron or hole transporting layers. These devices with a hole-conducting and an electron-conducting polymer exhibit high quantum efficiencies at 29 % [79]. The ideal BHJ device is approximately 100-300 nm and the absorptivity of the active components should be high enough to allow for a substantial portion of light to be absorbed within this film thickness. The D and A materials are dispersed such that the interfaces for charge separation are spaced at approximately 10 nm intervals, to allow for excitons to be dissociated before they recombine [Figure 2.15(e)] [80, 81]. The domains of the hole and electron accepting materials are organized in striated units such that they form direct pathways along the applied electric field for efficient carrier transport to the electrodes. In the work described in the following chapter 7, materials and techniques are specifically chosen to enable us to apply this design.

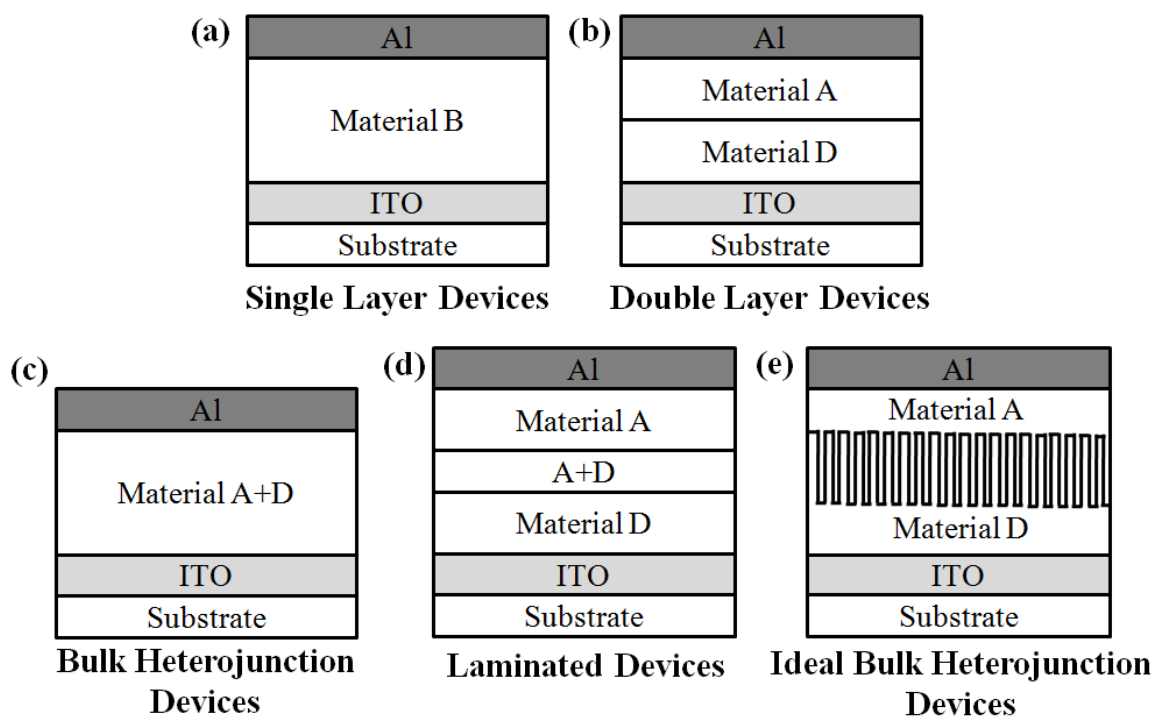


Figure 2.15 The most common device architectures for organic solar cells. Material B is any organic material. A is an electron acceptor material and D is an electron donor material.



2.6 Characterizing Efficiency

The efficiency of a photovoltaic device can be described in two ways. [82] The first is a power conversion efficiency, which states how much electrical power is produced per unit of incident radiation power. The second is the quantum efficiency (QE), which is the efficiency of a device as a function of the energy or wavelength of the incident radiation. For a particular wavelength, it specifically relates the number of charge carriers collected to the number of photons shining on the device. QE can be reported in two ways: internal quantum efficiency (IQE) and external quantum efficiency (EQE). The external quantum efficiency (EQE) expresses the number of photons that are converted to electrons. Although the EQE is important to understand the mechanisms of current generation, it is rarely given as measure of the efficiency of a commercial solar cell. More important for these commercial devices is the power conversion efficiency of the device under solar conditions. To characterize the efficiency of our devices we perform two standard experiments: current-voltage (I - V) and spectral response measurements.

2.6.1 Current-Voltage Characteristics

For commercial applications, the most important parameter is the power conversion efficiency η of a photovoltaic cell. Since electrical power is a product of the current and voltage, the power conversion efficiency is determined from measuring the current as a function of voltage. The power conversion efficiency can be expressed in terms of the power of the incoming light P_{light} and the electrical output power P_{out} of the cell:

$$\eta(\lambda) = \frac{P_{\text{out}}(\lambda)}{P_{\text{light}}(\lambda)}$$

The maximum theoretical power output is given by the product of the short circuit photocurrent I_{sc} and the open circuit voltage V_{oc} . Figure 2.16 shows both the ideal and a typical I - V curve found experimentally. [82]

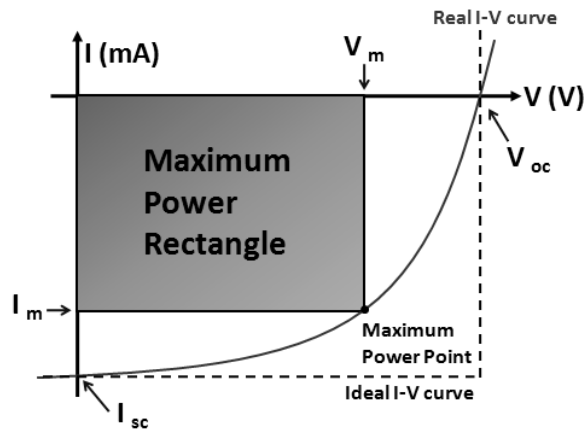


Fig. 2.16 Illustration of the difference between a real and an ideal I - V curve. The area of the inner rectangle corresponds to the maximal output power of the real device (at the maximum power point), whereas the area of the outer rectangle formed by the axes and the ideal I - V curve is equivalent to the maximum ideal output power.

Real I - V characteristics are curved and we have to maximize the product of current and voltage in order to obtain the maximum power output. The ratio between the maximum theoretical power output and the actual maximum power output is an important feature of the I - V characteristics. This ratio is called the fill factor (FF) and can be defined as:

$$FF = \frac{I_m V_m}{I_{sc} V_{oc}}$$

If we express the maximum output power of a photovoltaic cell using the fill factor, the power conversion efficiency (PCE) becomes:

$$P_m = I_m V_m$$

$$\eta = \text{PCE} [\%] = \frac{P_m}{P_{in}} = \frac{I_m V_m}{P_{in}} = \frac{FF \times I_{sc} V_{oc}}{P_{in}}$$

A large amount of information is contained within the I - V characteristics of a device. The I_{sc} is proportional to the EQE and coupled with the V_{oc} and FF, it provides all the parameters required to characterize the power efficiency of the cell.

2.6.2 Equivalent Circuit Diagrams

$$I = I_0 \left\{ \exp \left(\frac{e}{nkT} (U - IR_S) \right) - 1 \right\} + \frac{U - IR_S}{R_{SH}} - I_{PH}$$

Where I_0 is the dark current, e the elementary charge, n the diode ideality factor, U the applied voltage, R_S the series, R_{SH} the shunt resistance, and I_{PH} is the photocurrent. The corresponding equivalent circuit is depicted in Figure 2.17. The shunt resistance usually reflects the degree of leakage current which caused by pinholes through the device. It represents the overall quality of the film. The series resistance includes the resistance of the active layer, organic material/metal interface, and electrodes. It always decreases with the thickness of active layer. However, the small thickness does not absorb enough photons that can not obtain respectable power conversion efficiency. For a high FF, two things are required: (1) that the shunt resistance is very large to prevent leakage currents and (2) that the series resistance is very low to get a sharp rise in the forward current [83].

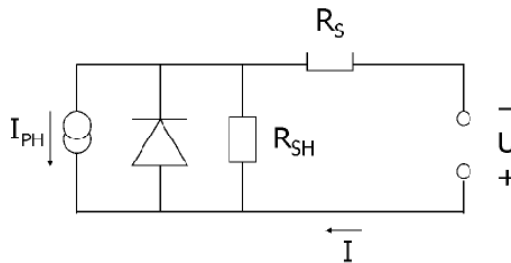


Fig. 2.17 Equivalent circuit diagrams for a solar cell.

2.6.3 Spectral Response

The EQE is defined as the number of electrons collected in the external circuit per incident photon.

$$EQE = \frac{\text{number of electrons in external circuit}}{\text{number of incident photons}}$$

The number of photons may be measured using a calibrated silicon photodiode. The responsivity of a silicon photodiode, $R_{si}(\lambda)$ (in A/W) is used to convert the measured

current on the silicon device to the intensity for a given area at a wavelength λ . In practice the incident light used to excite the sample is not perfectly monochromatic, but has a spectral width $\Delta\lambda$. This has to be taken into account when integrating over λ . [82] The responsivity of the sample at that wavelength is given by

$$R(\lambda) = \frac{J_{sc}(\lambda)}{I_{light}(\lambda)}$$

where $J_{sc}(\lambda)$ is the short circuit current density of the photovoltaic cell, under zero applied voltage. The irradiance is defined as

$$I_{light}(\lambda) = \Phi(\lambda)E_{photon}(\lambda)$$

where $\Phi(\lambda)$ is the photon flux (photons per unit area, time) and $E_{photon}(\lambda)$ is the photon energy. The number of incident photons arriving at the sample during time t in $\Delta\lambda$ is given by

$$\text{number of incident photons in } \Delta\lambda = \frac{I_{light}(\lambda)}{E_{photon}(\lambda)} \cdot A \cdot t$$

where A is the active area of the photovoltaic cell. The number of electrons collected at the electrodes during the time t in $\Delta\lambda$ is given by

$$\text{number of electrons in } \Delta\lambda = \frac{J_{sc}(\lambda) \cdot A \cdot t}{e}$$

Combining the last six equations and using $E_{photon} = hc/\lambda$, where h is Planck's constant and c denotes the speed of light in vacuum, the EQE can be expressed as

$$\text{EQE}(\lambda) = \frac{J_{sc}(\lambda) \cdot A \cdot t}{e \cdot \Phi(\lambda) \cdot A \cdot t} = \frac{J_{sc}(\lambda) \cdot E_{photon}(\lambda)}{e \cdot I_{light}(\lambda)} = R(\lambda) \cdot \frac{hc}{e\lambda}$$

The EQE is therefore proportional to the responsivity and depends on the photocurrent density of the sample and the photon flux at the sample position. So that the short-circuit current density J_{sc} is expressed by

$$J_{sc}(\lambda) [\text{A/m}^2] = \int_{\lambda_1}^{\lambda_2} \frac{I_{light}(\lambda) \cdot \text{EQE}(\lambda) \cdot \lambda d\lambda}{1240}$$

Therefore, the short-circuit current density can be calculated by using this equation

through the EQE measurement. Comparing with the J_{SC} from the PCE and EQE results, we can double check the correctness of J_{SC} in the devices. In the case of the P3HT:PCBM blend, and for an EQE of 100%, the maximum possible J_{sc} is about 18.7 mAcm^{-2} . If the average EQE is only 50%, J_{sc} would then be only about 9.35 mAcm^{-2} .

The internal quantum efficiency (IQE) for a photovoltaic cell is defined as

$$\text{IQE} = \frac{\text{number of electrons in external circuit}}{\text{number of photons absorbed in film}}$$

This quantity disregards optical loss mechanisms such as reflection and transmission. The IQE at wavelength λ can be obtained by dividing the EQE by the absorption:

$$\text{IQE}(\lambda) = \frac{\text{EQE}(\lambda)}{1 - R(\lambda) - T(\lambda)}$$

where $R(\lambda)$ and $T(\lambda)$ are the reflection and the transmission at wavelength λ respectively.

Although the IQE can express the ability of a material between two electrodes to dissociate excitons, transport and collect the charge carriers, it ignores the ability of the device to absorb light, which is one of the most important processes in light harvesting.

For instance, Figure 2.18 summarizes the number of photons (N_{ph}) absorbed in the P3HT:PCBM layer versus the thickness of this layer for an organic solar cell having the following structure: glass (1 mm)/indium tin oxide (ITO, 140 nm)/poly(3,4-ethylenedioxythiophene): poly(styrenesulfonate) (PEDOT:PSS, 50 nm)/P3HT:PCBM (x nm)/Al (100 nm) [84]. It appears, in Figure 2.18, that N_{ph} generally increases with increasing thickness, but not monotonically. If the thickness of the layers is smaller than the coherence of the light, interference occurs, because the light is reflected by the opaque electrode. About $9.5 \times 10^{16} \text{ photons s}^{-1} \text{ cm}^{-2}$ are absorbed in an active layer of 5 mm. Assuming an average IQE of 100%, this represents a J_{sc} value of 15.2 mAcm^{-2} , or approximately 20% less than in the theoretical consideration. In the case of an active layer that has a more realistic thickness of 400 nm, the maximum J_{sc} (IQE=100%) is 12.8

mAcm^{-2} . If the average IQE is lower than 100%, J_{sc} is further reduced. At 80% average IQE, J_{sc} should be around 10.2 mAcm^{-2} . Thus, despite the fact that the theoretical short-current density of a P3HT:PCBM blend could be close to 19 mAcm^{-2} , the practically achievable J_{sc} of real devices will be in the range of $10\text{--}12 \text{ mAcm}^{-2}$. Consequently, the EQE is more often used to characterize the device.

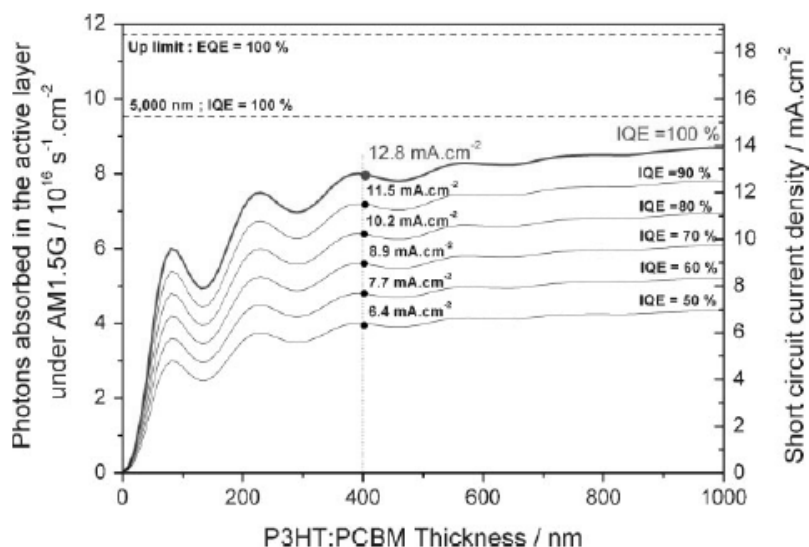


Figure 2.18 Number of photons (N_{ph}) absorbed in the active layer under AM 1.5G calculated by transfer-matrix formalism (TMF), for a device having the following structure: glass (1 mm)/ITO (140 nm)/PEDOT:PSS (50 nm)/P3HT:PCBM (x nm)/Al (100 nm). The right axis represents the corresponding short-circuit current density J_{sc} at various IQE, indicated in the graph.

2.6.4 Air Mass

Solar radiation is partially absorbed during its passage through the atmosphere, the absorption is almost entirely caused by gases of low concentration in the infrared region of the solar spectrum, by water vapor (H_2O), carbon dioxide (CO_2), laughing gas (N_2O), methane (CH_4), as well as by dust and, in the ultraviolet region of the spectrum, by oxygen and ozone. The standardised terrestrial spectra for direct and global sunlight are shown in Figure 2.19 where the global spectra comprises the direct plus the diffuse components.

Therefore, the absorption of course increases with the path length through the atmosphere. For a thickness l_0 of the atmosphere, the path length l through the atmosphere for radiation from the sun incident at an angle α relative to the normal to the earth's surface is given by

$$l = l_0 / \cos \alpha$$

The ratio of l / l_0 is called the air-mass coefficient. It characterizes the real solar spectrum resulting from the absorption of a layer of air of thickness l . In the definition, the spectrum outside the atmosphere is designated by AM0 (135 mAc m^{-2}) and that on the surface of the earth for the normal incident by AM1 (95 mAc m^{-2}). A typical spectrum for moderate climates is AM1.5, which corresponds to the angle of incidence of solar radiation of 48° relative to the surface normal (Figure 2.20) [82].

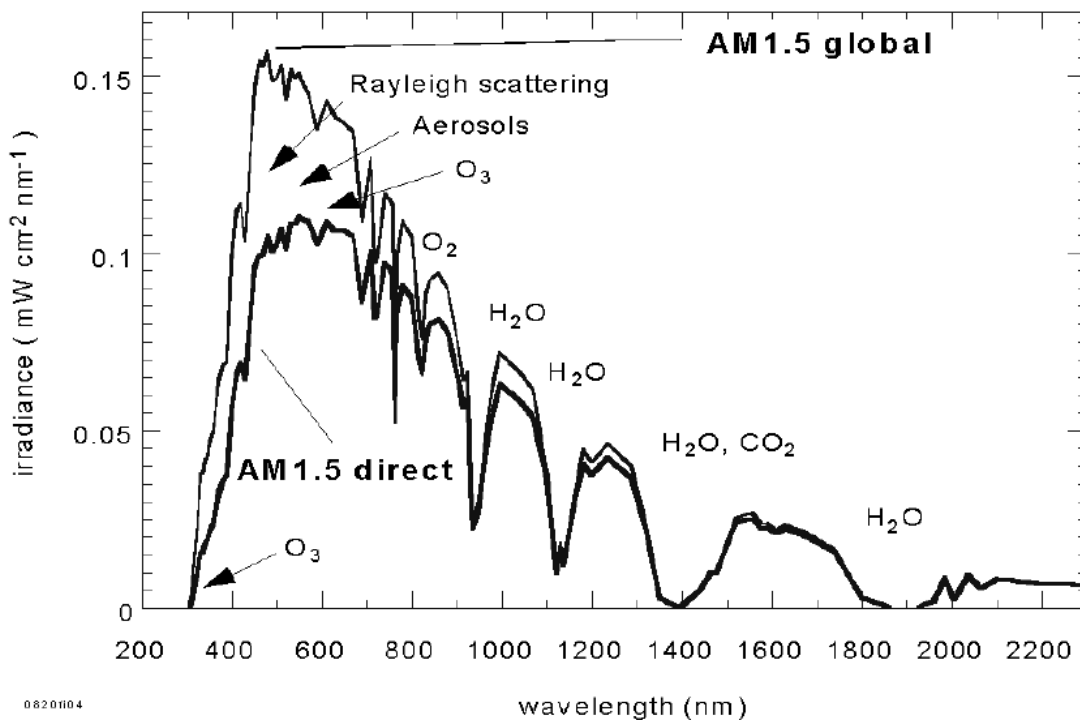


Figure 2.19 The two most commonly used standard spectra, AM 1.5 direct and AM 1.5 global. The global spectrum comprises the direct plus the diffuse sunlight. The difference is mainly in the shorter wavelength region since molecular scattering scales with λ^4 . Water (H_2O), ozone (O_3) and carbondioxide (CO_2) are the main absorbers of the solar radiation in Earth's atmosphere.

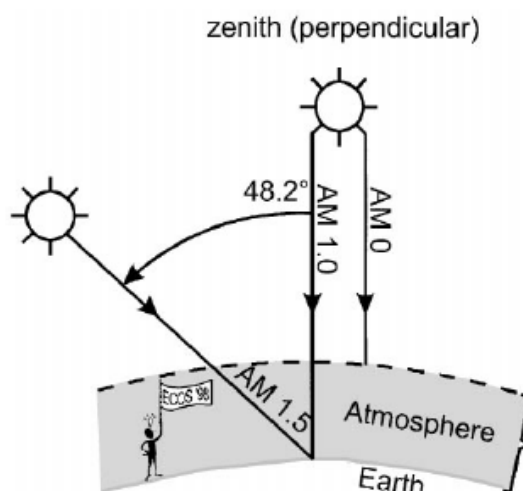


Figure 2.20 Schematic representation of the different AM sun light spectra.

2.6.5 Power Efficiencies under Solar Conditions

The power conversion efficiency can be given under monochromatic or white light illumination. Monochromatic power conversion efficiencies are not sufficient to characterize a solar cell but are a measure of the performance of the device at a specific wavelength. This is useful for the case that the device is intended for use under conditions other than solar, such as in small electronic devices and watches which function under ambient room lighting or as a power meter for laser radiation. The standard method of characterizing a solar cell is under Air Mass 1.5 or AM 1.5 conditions (sun's emission spectrum after traveling 1.5 times through the Earth's atmosphere). We measure our devices both under monochromatic and simulated solar illumination. The current-voltage (I-V) measurement of the OSC devices was conducted by a computer-controlled Keithley 2400 source measurement unit (SMU) with a solar simulator under the illumination of AM 1.5G coverage with power density of $100 \text{ mAc}m^{-2}$. Spectral irradiance data for standard solar radiation and the typical source irradiance for our solar simulator with AM 1.5G filter are shown in Figure 2.21. The spectral irradiance data of light source is similar to AM 1.5G solar spectrum (spectral mismatch $<5\%$ in the range from 350 nm to 800 nm).

The illumination intensity was calibrated through a Si reference cell with KG-5 filter. The output photocurrent was adjusted to match the photocurrent value of Si reference cell in order to obtain 100 mWcm^{-2} .

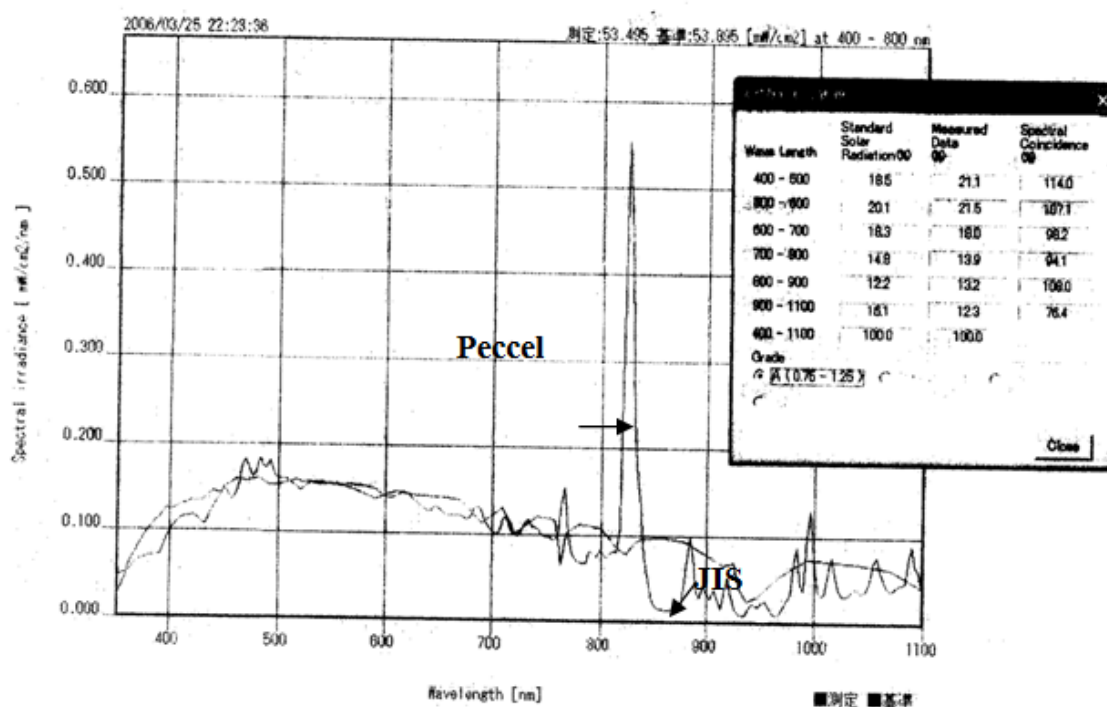
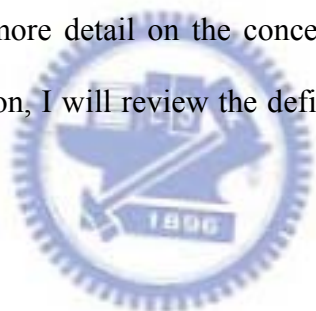


Figure 2.21 Spectral irradiance data for JIS AM 1.5 standard solar radiation and the typical source irradiance for a Peccel solar simulator with AM 1.5 G filters.

2.7 Surface Energy

Surface energies (SE) of substrate and of adsorbates concern with the interface interaction. The additional free energy at the interface between two condensed phases is known as interfacial energy. These interfacial forces determine whether the film morphology is wetted or dewetted on a substrate. Surface and interfacial energy are important properties because of their controlling influence on such practical applications as spinning, polymer adhesion, stability of dispersions and wetting of solids by liquids. In the chapter 4 of this thesis, the SE information figure out the optimum condition of KOH treatment in fabricating NiPI films. In chapter 6, the interface problems of manufacturing inverted PSCs can be solved from the SE results. Furthermore, in the chapter 7, the SE response is crucial to learn more detail on the concept for producing the CuPc rod-like films. Therefore, in this section, I will review the definition and the measuring method of surface energy.



2.7.1 Definition of Surface Energy

The specific free surface energy of a material is the excess energy per unit area due to the existence of the surface energy. In liquids, the specific free surface energy is also called surface tension, since it is equivalent to a line tension acting in all directions parallel to the surface. At a surface, surface energy derives from the unsatisfied bonding potential of molecules. This is in contrast to molecules within a material, which has less energy because they are subject to interactions with other like molecules in all directions. Molecules at the surfaces will try to reduce the free energy by interacting with molecules in an adjacent phase. As the interface between two condensed phases (i.e. solid-solid, solid-liquid and immiscible liquid-liquid interfaces) was concerned, the free energy per unit area of the interface is termed as the interfacial energy. [85, 86] The surface or

interfacial tension is expressed in J/m^2 ($\equiv \text{N/m}$) or more often in mJ/m^2 ($\equiv \text{mN/m} \equiv \text{erg/cm}^2 \equiv \text{dyne/cm}$).

The notation is the following:

γ_l : surface tension of liquid

γ_s : surface tension of solid

γ_{sl} : interfacial tension between liquid and solid

γ_{sv} : surface tension of the solid in equilibrium with the saturated vapour
pressure of the liquid

2.7.2 Surface Energy of Solids

There are three available ways to estimate the surface tension of solids (γ_s). The first method is measuring the contact angle between the solid and different liquids and applying as

$$\gamma_s = \frac{[\gamma_l(1 + \cos \theta) + \pi_{eq}]^2}{4\Phi^2 \gamma_l} \approx \gamma_l \frac{(1 + \cos \theta)^2}{4\Phi^2}$$

$$\Phi \approx \gamma_l \frac{4(V_s V_l)^{1/3}}{(V_s^{1/3} + V_l^{1/3})^2}$$

The second way is the determination of γ_{cr} according to Zisman (1964) [86], with the assumption that $\gamma_s \approx \gamma_{cr}$. The third method is the extrapolation of surface tension data of melts to room temperature. In this thesis, I usually used the first method to measure the contact angle and then got the surface energy of substrates. If no experimental datum are available for analyzing the nanophase difference of PEDOT:PSS films. I also used the calculation to give a reliable approximation by means of the group contributions to the parachor (see chapter 7). Because the surface tensions of liquids it may be expected that the relation also exists between the surface tension and the cohesive energy density of

solid polymers [87]. This proves to be so; with γ expressed in mJ/m^2 and e_{coh} in MJ/m^3 , the following empirical expression may be used:

$$\gamma \approx 0.75e_{\text{coh}}^{2/3}$$

The cohesive energy E_{coh} of a substrate in a condensed state is defined as the increase in internal energy U per mole of substance if all the intermolecular forces are eliminated:

The cohesive energy $\equiv E_{\text{coh}} \equiv \Delta U$ (J/mol)

Directly related to the cohesive energy are the quantities

Cohesive energy density: $e_{\text{coh}} = \frac{E_{\text{coh}}}{V}$ (at 298K)

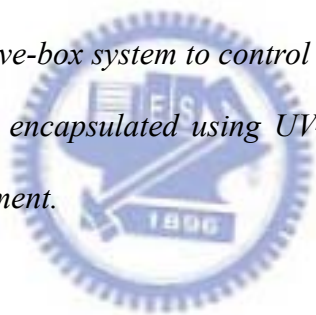
Solubility parameter: $\delta = \left(\frac{E_{\text{coh}}}{V}\right)^{1/2} \equiv e_{\text{coh}}^{1/2}$



Chapter 3

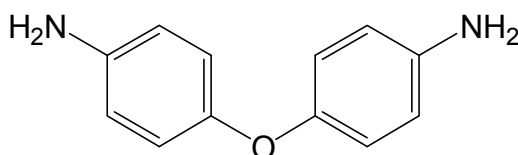
Materials and Experimental Techniques

A short overview of the materials used and the experimental details that we developed for reproducible device preparation and characterization will be presented. The operational characteristics of devices based on organic semiconductors are very sensitive with respect to the exposure to oxygen and water. Therefore, the preparation of the OSCs should be carried out in a glove-box system to control the atmosphere or in a high vacuum system. The OSCs should be encapsulated using UV-curing glue in a glove-box system before the efficiency measurement.

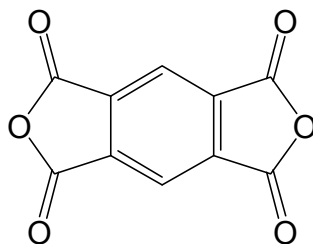


3.1 Materials

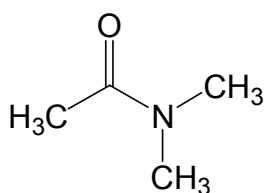
(1) 4, 4'-diaminodiphenylether (ODA, 98%) from Aldrich Chemical Co. was vacuum-dried for 3 h at 110 °C prior to use.



(2) Pyromellitic dianhydride (PMDA) from TCI was purified by recrystallization from a high-purity acetic anhydride and then dried in a vacuum oven at 120 °C for at least 14 h.



(3) N,N-Dimethylacetamide (DMAc) from Aldrich Chemical Co. was stored over molecular sieves prior to use.

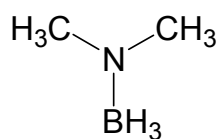


(4) KOH: Potassium hydroxide from TCI.

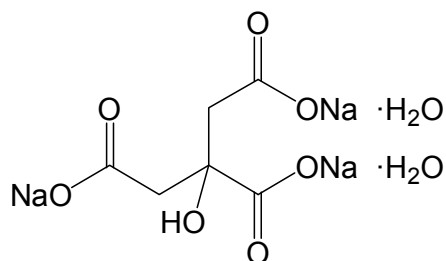
(5) Nickel(II) sulfate hexahydrate ($\text{NiSO}_4 \cdot 6\text{H}_2\text{O}$) from TCI.

(6) Sodium borohydride (NaBH_4) from TCI.

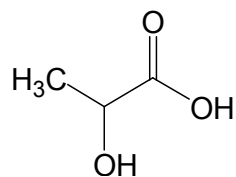
(7) Dimethylamine borane (DMAB) from TCI.



(8) Sodium citrate tribasic dihydrate from TCI.

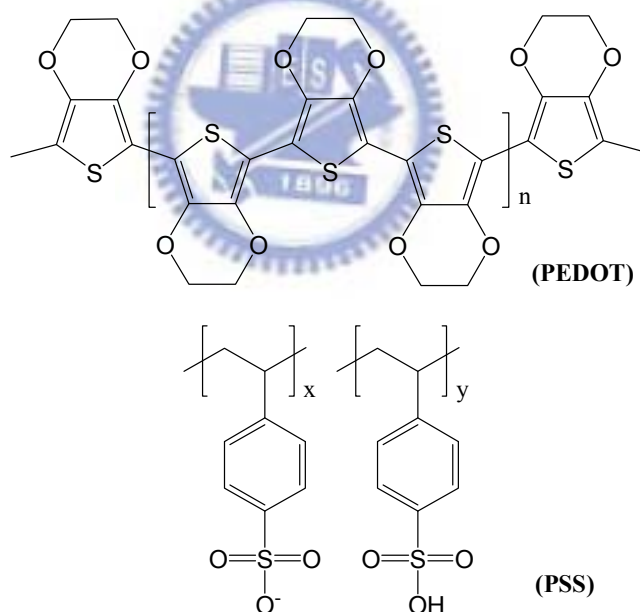


(9) Lactic acid: Lactic acid (~90%) from Fluka.



(10) Indium Tin Oxide (ITO) glass substrate: ITO glass substrates from Sanyo, Japan ($8\Omega/\text{sq.}$) were first patterned by lithograph, then cleaned with detergent, and ultrasonicated in acetone and isopropyl alcohol, subsequently dried on hot plate at $120\text{ }^\circ\text{C}$ for 5 min, and finally treated with oxygen plasma for 5 min. The thickness of ITO is ca. 200 nm.

(11) Poly(3,4-ethylenedioxythiophene)-poly(styrenesulfonate) (PEDOT:PSS) from H.C. Starck (CLEVIOS P and CLEVIOS HC V4).



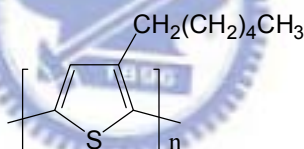
According to experience to date, CLEVIOS™ P is stable for at least 6 months when stored at $20\text{ }^\circ\text{C}$ in sealed, original containers. Once the container is opened, care must be taken to ensure that the dispersion does not dry on the walls, as the product can no longer be readily dispersed in water if dry and the optical properties of the PEDOT coating could be impaired. The general properties of PEDOT:PSS (CLEVIOS™) are listed in Table 3.1.

Table 3.1 Overview CLEVIOS™ general properties. (Note: The previous trade code of CLEVIOS productions was named Bytron.)

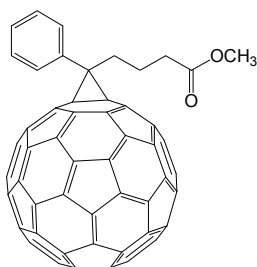
	moderate conductivity ← → high conductivity	PEDOT : PSS ratio	Viscosity at 100 s ⁻¹ [mPas]	Solid Content [%]
CLEVIOS™ P		1 : 2.5	60 – 100	1.2 – 1.4
CLEVIOS™ PH		1 : 2.5	Max. 25	1.2 – 1.4
CLEVIOS™ P AG		1 : 2.5	50 – 90	1.1 – 1.3
CLEVIOS™ P HC V4		1 : 2.5	100 – 250	1.1 – 1.4
CLEVIOS™ PH 500		1 : 2.5	8 – 25	1.0 – 1.3
CLEVIOS™ PH 510		1 : 2.5	20 – 100	1.5 – 1.9
CLEVIOS™ P HS		1 : 2.5	not specified	2.6 – 3.2
CLEVIOS™ S HT		1 : 2.5	3 -5 dPas	not specified
CLEVIOS™ S V3		1 : 2.5	15 – 200 dPas	not specified
CLEVIOS™ F CPP 105 DM		1 : 2.5	30 – 60	1.0 – 1.4
CLEVIOS™ F E		1 : 2.5	40 – 80	2.2 – 2.6
CLEVIOS™ F PVA		1 : 2.5	150 – 200	3.8 – 4.3

After addition of 5% Dimethylsulfoxid

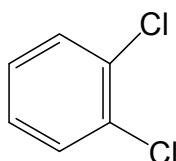
(12) Regioregular poly(3-heptylthiophene) (rr-P3HT) from Rieke Metals, Inc.. Highly regioregular Electronic Grade. Typical results are between 90% and 93% regioregularity (4002-E).



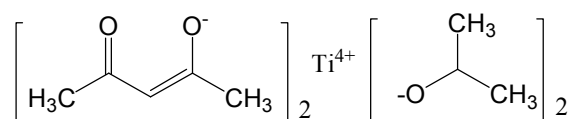
(13) [6,6]-phenyl-C₆₁-butyric acid methyl ester (PCBM) from Nano-C (99.5%).



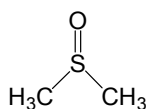
(14) o-Dichlorobenzene (DCB), anhydrous (99.8%) from Sigma-Aldrich.



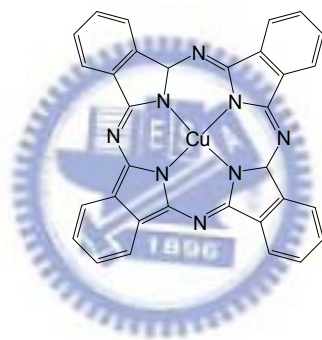
- (15) Titanium (diisopropoxide)bis(2,4-pentanedionate (TIPD) (75wt% in isopropanol) from Aldrich.



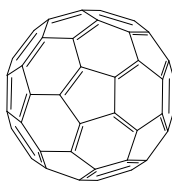
- (16) Dimethyl sulfoxide (DMSO, $\geq 99.9\%$) from Sigma-Aldrich.



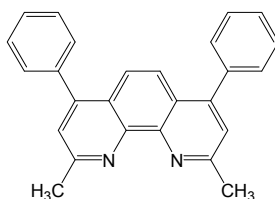
- (17) Copper phthalocyanine (CuPc), obtained from Sigma-Aldrich (sublimation grade) without further purification.



- (18) Fullerene (C₆₀), obtained from Sigma-Aldrich (sublimed, 99.9%) and used as received.



- (19) 2,9-dimethyl-4,7-diphenyl-1,10-phenanthroline (BCP) was purchased from Sigma-Aldrich (99.5%).



3.2 Experimental Techniques

3.2.1 Preparation of Polyimide Films

Poly(amic acid) (PAA) solutions were made by reacting equal molar amounts of diamine and dianhydride in solution (15% solid content (w/w) for ODA/PMDA in DMAc) under a nitrogen atmosphere. At beginning, ODA was firstly dissolved in DMAc, and then PMDA was added into the solution by five portions and it is better to ensure the completely dissolution of the prior portion before adding a fresh portion. After the dissolution of PMDA, the PAA solution was further stirred for 2 h at ambient temperature. The PI films were made by casting the PAA onto a dust free glass plate with a doctor blade, and then step-heated at 100 °C, 150 °C, 200 °C, 250 °C, 300 °C and 350 °C, each step for an hour to form PI films with 40 μ m thickness.

3.2.2 Preparation of Surface-Nickelized Polyimide Films

The polyimide (PMDA-ODA) films were first immersed in a 1 M potassium hydroxide (KOH) aqueous solution at 50 °C for several min, followed by rinsing with deionized water. The PI films with the surface opening imide rings to exchange potassium ions with Ni²⁺ ions were immersed into a 50 mM nickel sulfate aqueous solution at 50 °C for several min, followed by rinsing with deionized water. The surface Ni²⁺ ions were then reduced in a sodium borohydride aqueous solution (0.2 g/100 ml deionized water) at 50 °C for 30 min to form Ni nanoparticles on PI surface. The samples were rinsed with deionized water after reduction. The nickel nanoparticles-seeded PI films were immersed in the electroless nickel bath (EN solution) to form thin Ni layers. The EN solution was prepared from a nickel stock solution and a DMAB solution with a 4/1 volumetric proportion. The nickel stock solution was composed of 40 g/L nickel sulfate, 20 g/L sodium citrate, and 10 g/L lactic acid in deionized water, and the DMAB aqueous solution was 1 g/L DMAB in

deionized water.

3.2.3 Device Fabrication

The fabrication of the standard PSCs cells investigated in this work is summarized in the following steps:

Step No.	Step Items	Details
1.	Cleaning of ITO substrates	<p>Before the organic film could be spin coated from solution onto the substrate the latter was cleaned according to the following steps:</p> <ol style="list-style-type: none"> 1. Rubbing the ITO glass substrates with soap and water. 2. Ultrasonic cleaning in D.I. water for 10 min. 3. Ultrasonic cleaning in acetone for 10 min. 4. Ultrasonic cleaning in IPA for 10 min. 5. Blow drying by using an air gun. 6. Drying by using hot plate at 120 °C for 5 min. <p>Cleaning is essential to avoid shorts due to dust particles as well as uncontrolled impurities that might have an effect on electrical the junction between the ITO and PEDOT organic film.</p>
2.	Oxygen plasma treatment	The cleaned substrates were treated to an oxygen plasma for 3-5 minutes to remove organic matter and to render the surface of ITO hydrophilic.
3.	PEDOT:PSS film casting	PEDOT:PSS aqueous solution was filtered through a 0.45 μ m filter prior to being deposited onto cleaned glass substrates at a thickness of ca. 50 nm through spin-coating at 4500 rpm in the air. The PEDOT:PSS films were then dried at 150 °C for 1 h in a glove box.
4.	Film fabrication	A blend [0.8 : 1 (w/w), 17 mg/mL in DCB of PCBM and P3HT] was stirred overnight in a glove box, filtered through a 0.2 μ m PTFE filter, and then spincoated (450 rpm, 60 s) on top of the PEDOT:PSS layer. The P3HT:PCBM

		films were then annealed at 140 °C for 20 min in a glove box.
5.	Evaporation of electrodes	The device was completed by coating 30- and 100-nm-thick layers of Ca and Al, respectively, under pressures of less than 10 ⁻⁶ Torr.
6.	Encapsulation of devices	The cell was then encapsulated using UV-curing glue.

In the chapter 5, we mainly devised a simple method to enhance the conductivity of PEDOT:PSS films through spin-coating with various surface-modified compounds, furthermore, the phenomena occurring through conductivities, morphologies, and chemical properties of the modified PEDOT:PSS films (P) were discussed in detail. Therefore, in order to understand the origin effects in ITO-free devices by using those surface-modified PEDOT:PSS, we took the modified ITO pattern (Figure 3.1(B)) as completely electrical contacts in those ITO-free device systems, and the architecture were different from the pristine device pattern with P/ITO anodes (Figure 3.1(A)). The active area of all devices, defined through a shadow mask to limit the area of input light.

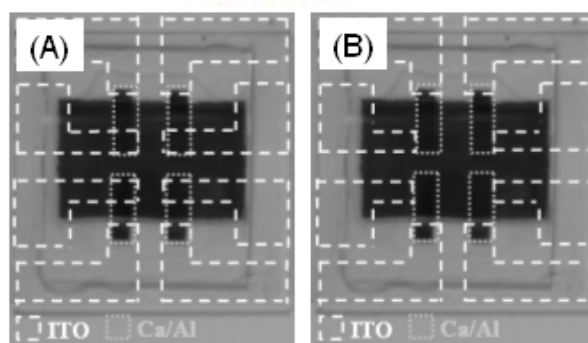


Figure 3.1 Photographs of polymer/fullerene solar cells with (A) P/ITO anode, (B) surface-modified PEDOT:PSS anode.

The fabrication of the inverted PSCs cells investigated in this work is summarized in the following steps:

Step No.	Step Items	Details
1.	Cleaning of NiPI films [Figure 3.2(A)]	Before the organic film could be spin coated from solution onto the substrate the latter was cleaned according to the following steps: <ol style="list-style-type: none"> 1. Rubbing the NiPI films in acetone using a cotton bud. 2. Ultrasonic cleaning in D.I. water for 10 min. 3. Ultrasonic cleaning in acetone for 10 min. 4. Ultrasonic cleaning in IPA for 10 min. 5. Blow drying by using an air gun. 6. Annealing by using hot plate at 150 °C for 1 h in a glove box.
2.	TIPD solution treatment [Figure 3.2(B)]	The cleaned NiPI films were pre-coated with an TIPD solution through spin-coating at 7000 rpm for 30 s.
3.	Film fabrication [Figure 3.2(B)]	A blend [0.8 : 1 (w/w), 17 mg/mL in DCB of PCBM and P3HT] was stirred overnight in a glove box, filtered through a 0.2 μ m PTFE filter, and then spincoated (500 rpm, 60 s) on top of the TIPD layer. The P3HT:PCBM films were then annealed at 140 °C for several min in a glove box.
4.	Plasma treatment [Figure 3.2(C)]	A mild oxygen plasma exposure for 5 s.
5.	PEDOT:PSS film casting [Figure 3.2(C)]	PEDOT:PSS aqueous solution was filtered through a 0.45 μ m filter prior to being deposited onto cleaned glass substrates at a thickness of ca. 50 nm through spin-coating at 4000 rpm in the air. The PEDOT:PSS films were then dried at 100 °C for 5 min in a glove box.
6.	Evaporation of metal grids [Figure 3.2(D)]	The device was completed by coating 100-nm-thick layers of Au as metal grids and masks, under pressures of less than 10^{-6} Torr.
7.	Electrical contact	After removal from the vacuum chamber, the

	[Figure 3.2(E)]	electrical contacts were using silver-epoxy glue.
8.	Encapsulation of devices [Figure 3.2(F)]	The cell was encapsulated using UV-curing glue.

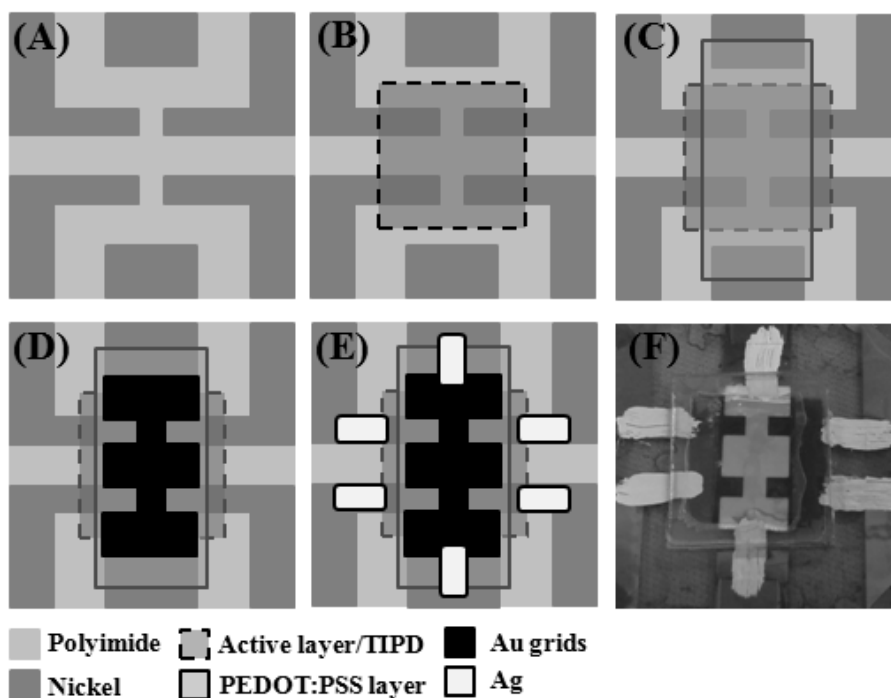


Figure 3.2 (A)-(E) Flow chart for the fabrication of the inverted PSCs on NiPI films. (F) The photograph of the inverted PSCs on NiPI films.

The fabrication of the small molecular OSCs cells investigated in this work is summarized in the following steps:

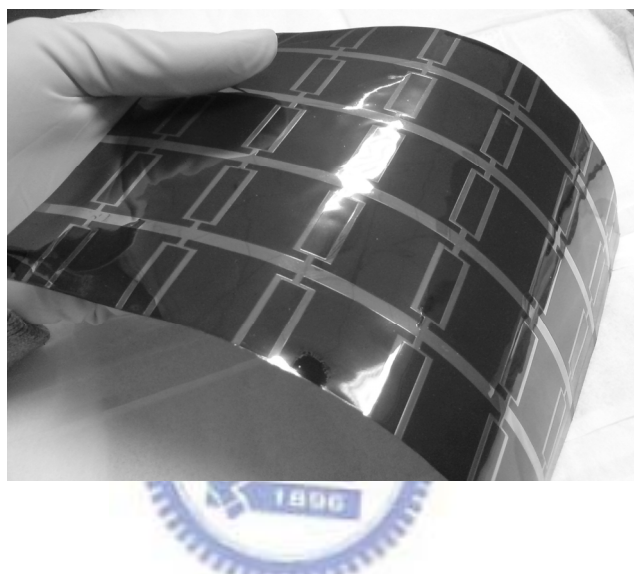
Step No.	Step Items	Details
1.	Cleaning of ITO substrates	Before the organic film could be spin coated from solution onto the substrate the latter was cleaned according to the following steps: 1. Rubbing the ITO glass substrates with soap and water. 2. Ultrasonic cleaning in D.I. water for 10 min. 3. Ultrasonic cleaning in acetone for 10 min. 4. Ultrasonic cleaning in IPA for 10 min. 5. Blow drying by using an air gun. 6. Drying by using hot plate at 120 °C for 5 min. Cleaning is essential to avoid shorts due to dust particles as well as uncontrolled impurities that might have an effect on electrical the junction between the ITO and organic film.
2.	Oxygen plasma treatment	The cleaned substrates were treated to an oxygen plasma for 3-5 minutes to remove organic matter and to render the surface of ITO hydrophilic.
3.	Substrate modification	1. ITO 2. AITO: Au (2 nm)/ITO 3. PITO: PEDOT:PSS (50 nm)/ITO
4.	CuPc rod-like film fabrication	CuPc was sublimed onto various anodes, including ITO, AITO and PITO, from a heated crucible (170 °C). The corresponding deposition rates, determined using a quartz crystal microbalance, were about 3 Ås ⁻¹ ; the morphologies of the CuPc films were controlled using various substrates at various substrate temperatures (T _{sub}).
5.	Co-evaporation of CuPc and C60	The corresponding deposition rates, determined using a quartz crystal microbalance, were about 1-3 Ås ⁻¹ , under pressures of less than 10 ⁻⁶ Torr.
6.	Deposition of C60	The corresponding deposition rates, determined

		using a quartz crystal microbalance, were about $1-3 \text{ \AA s}^{-1}$, under pressures of less than 10^{-6} Torr.
7.	Deposition of BCP	The corresponding deposition rates, determined using a quartz crystal microbalance, were about $1-3 \text{ \AA s}^{-1}$, under pressures of less than 10^{-6} Torr.
8.	Evaporation of electrodes	The device was completed by coating 150-nm-thick layers of Al, under pressures of less than 10^{-6} Torr.
9.	Encapsulation of devices	The cell was then encapsulated using UV-curing glue.



Chapter 4

Chemical Formation of Palladium-free Surface-nickelized Polyimide Film for Flexible Electronics



Flexible polyimide (PI) films for flexible electronics were surface-nickelized using a fully solution-based process and excellent adhesion between the nickel and polyimide phases was observed. Polyimide substrates were modified by alkaline hydrolysis, ion exchange, reduction and nickel electroless deposition without palladium. Atomic force microscopy and field emission scanning electron microscopy were used to follow the growth of nickel nanoparticles (Ni-NPs) and nickel layers on the polyimide surface. The surface resistances of the Ni-NPs/PI films and Ni/PI films, measured using a four-point probe, were 1.6×10^7 and $0.83 \Omega/\text{cm}^2$, respectively. The thicknesses of Ni-NPs and the Ni layer on the polyimide surface were 82 nm and 382 nm, respectively, as determined by transmission electron microscopy, and the Ni layer adhered well to PI, as determined by the adhesive tape testing method.

4.1 Introduction

Flexible aromatic polyimide (PI) films have been widely applied in soft electronics and microelectronics packages. The base materials of flexible printed circuits (FPC) and other soft electronics are copper on polyimide with or without adhesive. The former is called the three-layer mode (metal/adhesive/PI), while the latter is the two-layer mode (metal/PI). The development of FPC with smaller line widths and increased wire density is based on the two-layer mode. Several fabrication methods have been applied to the two-layer system. Popular methods are coating Poly(amic acid) (PAA) onto a copper surface; press a copper layer onto PI at high temperature, or sputtering a copper thin layer on PI followed by electrochemical copper plating. However, these methods raise problems. For instance, in the coating adhesive PAA method, the product warps after imidization. In the pressing copper layer and sputtering copper methods, the adhesion is weak at the interface between the copper and PI [88-90]. Although other methods for sputtering copper use apply plasma to increase the roughness to improve adhesion, another problem is that such approaches must be implemented in high vacuum systems, increasing the complexity of the process [91-96].

Recently, the two-layer mode (metal/PI) has been modified by using alkaline hydrolysis to open imide rings, followed by ion exchange with metal ions and the reduction of copper ions on PI [97-105]. Alkali treatments in the first step have been investigated using an aqueous solution of NaOH and KOH [106-109]. The ion exchange rate of copper and the dispersion of copper in underlying modified PI in the second step have been widely discussed [99, 101-103]. In the third step, the methods for reducing copper involve a thermally-induced hydrogen reaction, an ultraviolet (UV)-light-induced photochemical reaction (TiO₂ as photocatalysts) and a chemical reaction (dimethylamine borane (DMAB) and sodium borohydride (NaBH₄) as reductants) [99, 101-103]. On

hydrogen-induced systems, high-temperature treatment raises problems of diffusion and oxidation of the Cu nanoparticles. In ultraviolet (UV)-light-induced systems and chemical reductive systems, other problems arise, such as the elimination of TiO₂ and the difficulty of controlling interfacial structure between copper thin films and the underlying polyimide because of the ease of diffusion of copper in the polyimide. To improve Cu/PI films, a thin adhesion-promoting layer of such metals as Ni, Cr and Ti have been used to prevent Cu from diffusing into the PI substrate and also to promote interfacial adhesion [110-115]. Among these three metals, Ni is relatively environmentally harmless and cheap. Furthermore, it can be etched away by the same etchant as is used for copper. Therefore this investigation is the candidate for chemically developing Cu/PI systems with a thin Ni layer at the interface. Usually Ni electroless deposition is activated by Pd catalysts [116, 117], which easily initiate the growth of Ni electroless deposition, but are expensive. Accordingly, a cheaper catalyst with high catalytic activity is urgently required to replace Pd materials.

This investigation will synthesize nickel nanoparticles as seeds (catalysts) and a Ni metal layer as an adhesion-promoting layer on the surface of a polyimide film using a wet chemical process. It can reduce the cost of the catalyst and simplify the process of coating the adhesion-promoting layer on the PI film. This study fully explores the formation of Ni-NPs and Ni layer. The following are adopted to investigate the structures and morphologies; attenuated total reflection FTIR spectroscopy (ATR-FTIR), X-ray diffraction spectroscopy (XRD), contact angle measurements, four point probe conductivity measurements, atomic force microscopy (AFM), scanning electron microscopy (SEM), transmission electron microscopy (TEM), energy-dispersive X-ray spectroscopy (EDX) and the Scotch-tape test to determine adhesion between nickel and the polyimide films.

4.2 Experimental Details

4.2.1 Materials

4, 4'-diaminodiphenylether (ODA, 98%) from Aldrich Chemical Co. was vacuum-dried for 3 hr at 110 °C prior to use. Pyromellitic dianhydride (PMDA) from TCI was purified by recrystallization from a high-purity acetic anhydride and then dried in a vacuum oven at 120 °C for at least 14 hr. Dimethylacetamide (DMAc) from Aldrich Chemical Co. was stored over molecular sieves prior to use. Potassium hydroxide (KOH), NiSO₄ · 6H₂O, Sodium borohydride (NaBH₄), dimethylamine borane (DMAB) and sodium citrate all from TCI, and Lactic acid from Fluka were used as obtained.

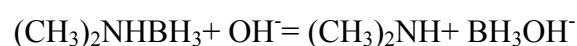
4.2.2 Preparation of polyimide films

Poly(amic acid) (PAA) solutions were made by reacting equal molar amounts of diamine and dianhydride in solution (15 % solid content (w/w) for ODA/ PMDA in DMAc) under a nitrogen atmosphere. At beginning, ODA was firstly dissolved in DMAc, and then PMDA was added into the solution by five portions and it is better to ensure the completely dissolution of the prior portion before adding a fresh portion. After the dissolution of PMDA, the PAA solution was further stirred for 2 hr at ambient temperature. The PI films were made by casting the PAA onto a dust free glass plate with a doctor blade, and then step-heated at 100 °C, 150 °C, 200 °C, 250 °C, 300 °C, 300 °C, and 350 °C, each step for an hour to form PI films with 40 μm thickness.

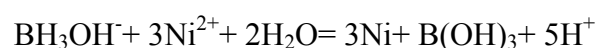
4.2.3 Preparation of the surface-nickelized polyimide films

The preparation of nickel-coated conductive films was carried out according to the Figure 4.1. The polyimide (PMDA-ODA) films were first immersed in a 1 M potassium

hydroxide (KOH) aqueous solution at 50 °C for several min, followed by rinsing with deionized water. The PI films with the surface opening imide rings to exchange potassium ions with Ni²⁺ ions were immersed into a 50 mM nickel sulfate aqueous solution at 50 °C for several min, followed by rinsing with deionized water. The surface Ni²⁺ ions were then reduced in a sodium borohydride aqueous solution (0.2 g/100 ml deionized water) at 50 °C for 30 min to form Ni nanoparticles on PI surface. Theoretically, each borohydride ion can reduce four or two nickel ions: $4\text{Ni}^{2+} + \text{BH}_4^- + 8\text{OH}^- = \text{B}(\text{OH})_4^- + 4\text{Ni} + 4\text{H}_2\text{O}$ or $4\text{Ni}^{2+} + 2\text{BH}_4^- + 6\text{OH}^- = 2\text{Ni}_2\text{B} + \text{H}_2 + 6\text{H}_2\text{O}$. The samples were rinsed with deionized water after reduction. (4) The nickel nanoparticles-seeded PI films were immersed in the electroless nickel bath (EN solution) to form thin Ni layers. The EN solution was prepared from a nickel stock solution and a DMAB solution with a 4/ 1 volumetric proportion. The nickel stock solution was composed of 40 g/L nickel sulfate, 20 g/L sodium citrate, and 10 g/L lactic acid in deionized water, and the DMAB aqueous solution was 1 g/L DMAB in deionized water. In alkaline and neutral solutions, the preceding chemical reaction of dimethylamine borane with OH⁻ ions could represent as:



DMAB has three active hydrogen atoms bonded to the boron, and theoretically can reduce three Ni²⁺ metal ions for each BH₃OH⁻ ion [118]:



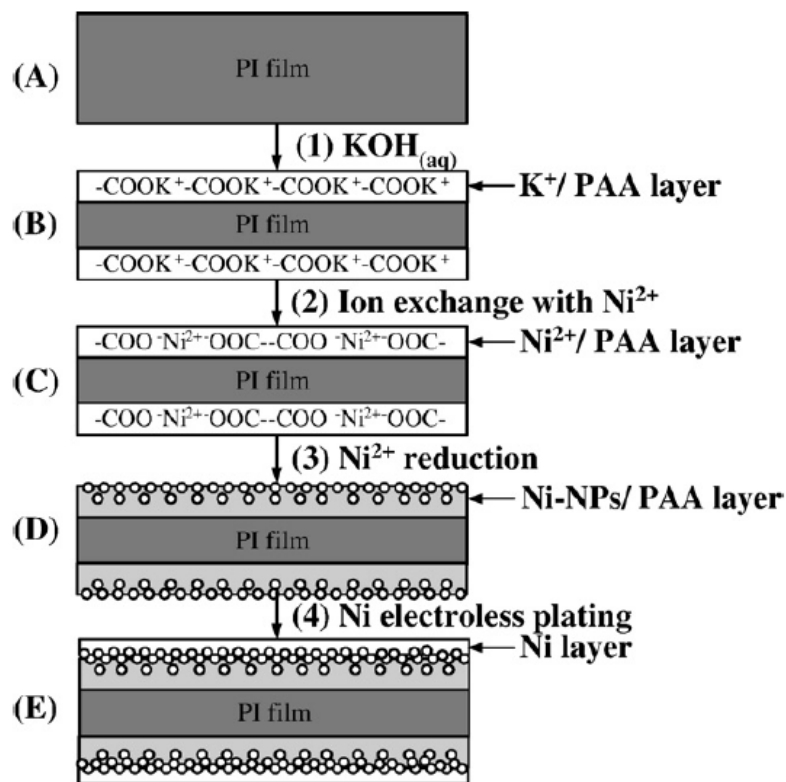


Figure 4.1 Flow chart of formation of surface-nickelized polyimide films: (a) PI film: Pristine polyimide (b) K⁺/PI film: K⁺/PAA layer on PI film, (c) Ni²⁺/PI film: Ni²⁺/PAA layer on PI film, (d) Ni-NPs/PI film: Ni-NPs/PAA layer on PI film, (e) Ni/PI films: Ni/PAA layer on PI film.

4.2.4 Measurements

FTIR absorption spectra were recorded by Perkin Elmer LEE-59 employing the attenuated total reflection (ATR) configuration. The ATR crystal, coated diamond crystal, was brazed into tungsten carbide disc. For sample of refractive index 1.5 at 1000 cm⁻¹, the depth of penetration was 2.0 μm. X-ray diffraction (XRD) spectra were obtained using a MacScience GIA model X-ray diffractometer. The equipment was operated with Cu Kα radiation, operating at 40 kV, 150 mA, with a scanning speed of 4 degree min⁻¹ at steps of 0.02°. The contact angle and surface energy were measured and calculated by Dynamic Contact Analyzer FTA-200 from a contact angle test using two standard liquids: H₂O and CH₂I₂. The surface resistance of metalized PI films was measured using four-point probe

(Napson RT-80/RG-80) and an average of the measured values was taken. The surface morphology changes of Ni-NPs/ PI films were analyzed by atomic force microscopy (AFM) (SPI 3800N Probe Station, Seiko Instruments Inc., Japan) in tapping mode (silicon tips on silicon cantilevers with a spring constant 2 N/m and the set point about 0.8-0.9) in air. Scanning electron microscopy (SEM) with JEOL JSM-6500F was used to investigate the Ni surface on the polyimide films. X-ray photoelectron spectroscopy (XPS) measurements were obtained using an ESCA PHI 1600 spectrometer working in the constant analyzer energy mode with a pass energy 50 eV and Mg K α (1253.6 eV) radiation as the excitation source. The XPS measurements were done at room temperature and pressure below 1.33×10^{-8} Pa. TEM was performed by employing a JEOL-2010 transmission electron microscope. The samples for TEM were microtomed with Leica Ultracut Uct into 90 nm thick slice and then moved onto a TEM copper grid with thick carbon layer. Elemental analysis was performed on an energy-dispersive X-ray (EDX) analyzer (OXFORD Instrument, Inc.) during TEM study. The accelerating voltage of TEM was 200 kV.

4.3 Results and Discussion

Figure 4.2 and Table 4.1 present the surface changes of polyimide modified with KOH, obtained using ATR-FTIR. In Figure 4.2(a), the characteristic peaks of bare PI (PMDA/ODA) were clearly visible at ~ 1720 , ~ 1780 , ~ 1500 , ~ 1380 and ~ 1230 cm^{-1} , corresponding to symmetric C=O stretching, asymmetric C=O stretching, benzene ring C=C stretching, imide ring C-N-C stretching and aromatic ether (Ar-O-Ar) stretching, respectively. Theoretically, after KOH treatment, the imide peak intensity at ~ 1720 , ~ 1780 , ~ 1380 and ~ 1230 cm^{-1} significantly changed but the benzene peaks at ~ 1500 cm^{-1} did not change. The obvious decline in the imide peak at ~ 1780 cm^{-1} was due to the opening of

imide rings by KOH treatment. In Table 4.1, the peak height 0.9627 of the bare imide rings at 1720 cm^{-1} divided by the peak height 0.8876 of the unchanged benzene peak at 1500 cm^{-1} was 1.0846, which was set as the standard for a surface imide content of 100%. The peak height of the bare imide rings at 1720 cm^{-1} changed from 0.9627 to 0.2778 after 10 min KOH treatment. The relative surface imide content reduced to 45.7%, indicating that 54.3% of the imide rings were cleaved to form the carboxylic acids and amides, which were further converted to the more wettable CO_2^- anions in aqueous KOH. After KOH treatment for 20 min, 30 min, 60 min and 120 min, the peak height of the residual imide characteristic peak had decreased from 18.4% to 4.6%, as shown in Table 4.1, suggesting that the proportion of cleaved imide rings increased from 81.6% to 95.4%. Extended KOH treatment could further increase the proportion of cleaved imide rings, but it became warped and crooked at high cleaved imide content. The best PI film for following surface-nickelized treatments was obtained by treating KOH for 30 min, and it had the most wettable surface and a good appearance.

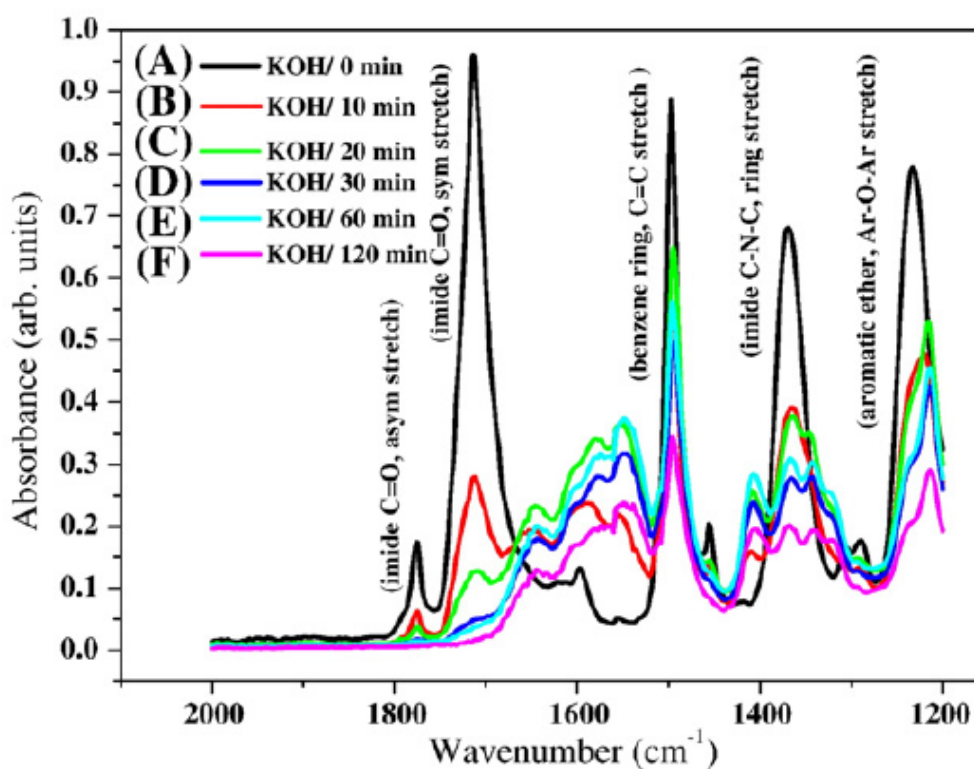


Figure 4.2 ATR-FTIR absorption spectra of polyimide modified with KOH for different times.

Table 4.1 Dependence of relative surface imide content of PI films and surface morphology of Ni-NPs/ PI films on treatment time with KOH.

KOH/ treatment time (min)	Peak Height		H_{1720}/H_{1500}	Relative Surface Imide Content (%)	Ra (Surface Roughness, nm)	D_{ave} (average Ni particle, nm)
	At 1720 cm^{-1} (imide peaks)	At 1500 cm^{-1} (benzene ring)				
(a) KOH/0	0.9627	0.8876	1.0846	100	0.89	---
(b) KOH/10	0.2778	0.5611	0.4951	45.7	23.90	269
(c) KOH/20	0.1298	0.6489	0.2000	18.4	11.64	131
(d) KOH/30	0.0520	0.4917	0.1058	9.8	14.30	161
(e) KOH/60	0.0396	0.5611	0.0706	6.5	10.00	113
(f) KOH/120	0.0172	0.3444	0.0499	4.6	5.99	---

The chemical structures of the surface-nickelized process on PI films were characterized using an ATR-FTIR spectroscope, as displayed in Figure 4.3. The characteristic peaks of imide groups in Figure 4.3(a) at ~ 1780 , ~ 1720 cm^{-1} and ~ 1380 cm^{-1} resulted from asymmetric C=O stretching, symmetric C=O stretching and imide ring C-N-C stretching, respectively. KOH treatment weakened the peak of the carbonyl stretching of imide rings, and produced new bands at 1500-1700 cm^{-1} , as shown in Figure 4.3(b). Following ion exchange, a slight increase in peak intensity at ~ 1780 and ~ 1720 cm^{-1} with imide ring reformation, a slight enhancement in intensity at ~ 1680 cm^{-1} and complex features at around 1500-1600 cm^{-1} suggested that a number of coordination states coexist within the Ni^{2+} complexes, as presented in Figure 4.3(c). The characteristic peak intensities of imide rings at ~ 1780 cm^{-1} and ~ 1720 cm^{-1} in Figure 4.3(d) were lower, because the pH of aqueous NaBH_4 was 11 and this solution reopened surface imide rings. The reopened imide rings were closed by annealing at 310°C for 1hr, as presented in Figure 4.3(e). Figure 4.3(f) shows no IR characteristic when more Ni was presented on the surface, because of the reflection or blocking of IR by the surface metal layer. Table 4.2 summarizes the clear changes in the peak height at 1720 cm^{-1} and the surface imide content following the full process. The peak height 0.9627 of the bare imide rings at 1720 cm^{-1} normalized with the peak height 0.8876 of the unchanged benzene peak at 1500 cm^{-1} is 1.0846, which value was set as the standard for a surface imide content of 100%. K^+ / PI films had only a 9.8% relative surface imide content in step (b). However, the relative surface imide content increased to 44.6% after ion exchange K^+ with Ni^{2+} at 50°C for 5 min in step (c), since more imide rings were formed in the relatively acidic (pH 6) NiSO_4 solution. In the alkaline electroless Ni plating solution (pH 11), the surface imide content declined to 7.6% in step (d), but imidization at 310°C for 1hr increased the surface imide content to 55.7% in step (e), because of ring closure during thermal treatment.

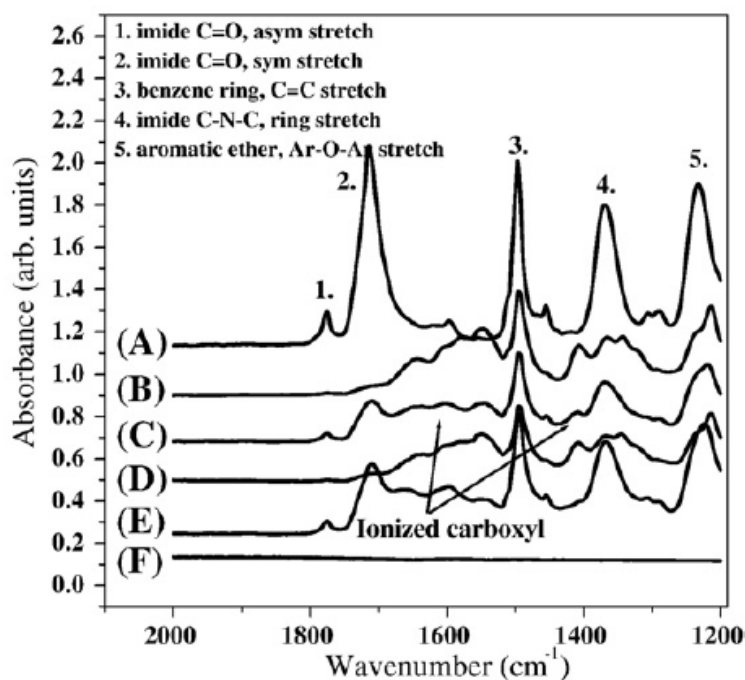


Figure 4.3 ATR-FTIR absorption spectra of (a) pristine PI film, (b) K^+ /PI films, (c) Ni^{2+} /PI film, (d) Ni-NPs/PI film, (e) Ni-NPs/PI film-310: Ni-NPs/PI film after annealing at $310^\circ C$ for 1hr, and (f) Ni/PI film.

Table 4.2 Relative surface imide content on polyimide throughout process.

Sample	Peak Height		H_{1720}/H_{1500}	Relative Surface Imide Content (%)
	At 1720 cm^{-1} (imide peaks)	At 1500 cm^{-1} (benzene ring)		
(a) PI films	0.9627	0.8876	1.0846	100
(b) K^+ /PI films	0.0520	0.4917	0.1058	9.8
(c) Ni^{2+} /PI films	0.2004	0.4166	0.4810	44.3
(d) Ni-NPs/PI films	0.0284	0.3461	0.0821	7.6
(e) Ni-NPs/PI films-310	0.3325	0.5500	0.6045	55.7
(f) Ni/PI films	---	---	---	---

(a) PI films: Bare PI films.

(b) K^+ /PI films: PI films treated with KOH aqueous solution (1 M, 30 min, $50^\circ C$, $pH=14$).

(c) Ni^{2+} /PI films: K^+ /PI films treated with $NiSO_4$ aqueous solution (50 mM, 30 min, $50^\circ C$, $pH=6$).

(d) Ni-NPs/PI films: Ni^{2+} /PI films treated with $NaBH_4$ aqueous solution (30 min, $50^\circ C$, $pH=11$).

(e) Ni-NPs/PI films-310: (d) Ni^{2+} /PI films are annealed at $310^\circ C$ for 1 hr in vacuum.

(f) Ni/PI films: Ni-NPs/PI films treated with EN solution (10 min, $50^\circ C$, $pH=7$).

---: the absorbance of functional group was not detected from ATR-FTIR.

Table 4.3 displays the contact angles and surface energies of bare PI and modified PI in different steps, measured using water and di-iodomethane. The contact angle of the PI film with water was 75.5° . KOH treatment substantially reduced the water contact angle of the K^{+}/PI film to 7.3° , because more imide rings cleaved to form wettable CO_2^{-} anions. Ion exchange with Ni^{2+} increased the water contact angle of the Ni^{2+}/PI film to 52° , because of the acidity of the $NiSO_4$ solution. The acidic solution caused the formation of more imide rings in this step, as presented in Figure 4.3(c). In the fourth step, when the Ni-NPs were formed by reducing Ni^{2+} to Ni-NPs, the contact angle of the surface increased markedly to 76° , which is presumed the result from the integral effects of Ni-NPs and bare PI films. Finally, when the nanoseeds were used to grow nickel films in EN solution, the contact angle increased further to 82.2° and the surface energy decreased to 37.2 (mN/m). In spite of the low relative surface imide content, the high relative surface wettability and the water contact angle unexpectedly increased, because the Ni-NPs surface is rough and exhibits a partial lotus effect. When the Ni/PI films were thermally aged at $110^{\circ}C$ and $310^{\circ}C$ respectively, the water contact angles were higher and the surface energy lower after the high-temperature treatment, the high-temperature aging reformed the imide ring from the polyamic acid and densified the Ni layer more effectively, as shown in Figure 4.4.

Table 4.3 Contact angles and surface energies of pristine PI and different stages of modification of PI.

Sample	Water	di-idomethane (C ₂ H ₄ I ₂)	Surface energy (mN/m)
(a) PI films	75.5	41.1	39.1
(b) K ⁺ /PI films	7.3	26.3	72.9
(c) Ni ²⁺ /PI films	52.0	33.8	49.2
(d) Ni-NPs/PI films	76	32.6	43.4
(e) Ni/PI films	82.2	45.3	37.2
(f) Ni/PI films-110	86.3	53.0	32.9
(g) Ni/PI films-310	108.0	73.9	23.7

(a) PI films: Pristine PI films.

(b) K⁺/PI films: PI films treated with KOH aqueous solution (1 M, 30 min, 50 °C).

(c) Ni²⁺/PI films: K⁺/PI films treated with NiSO₄ aqueous solution (50 mM, 30 min, 50 °C).

(d) Ni-NPs/PI films: Ni²⁺/PI films treated with NaBH₄ aqueous solution (30 min, 50 °C).

(e) Ni/PI films: Ni-NPs/PI films treated with EN solution (10 min, 50 °C).

(f) Ni/PI films-110: annealing 110 °C for 1 h in vacuum.

(g) Ni/PI films-310: annealing 310 °C for 1 h in vacuum.

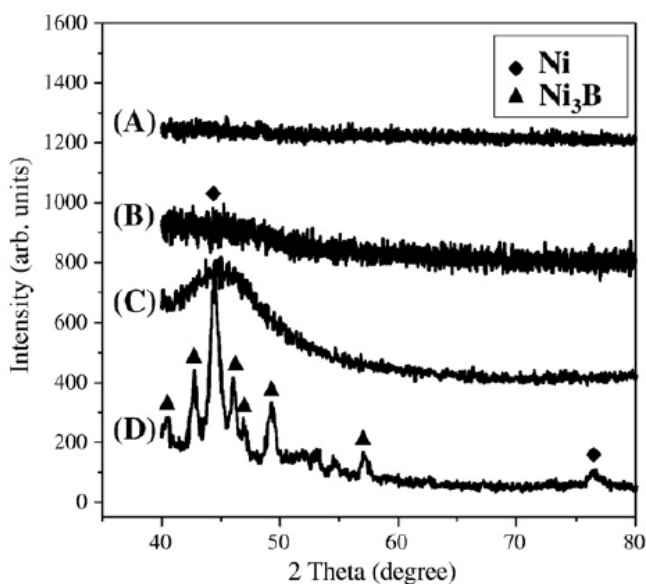


Figure 4.4 XRD patterns of (a) pristine PI film, (b) Ni-NPs/PI film-110 (annealed at 110 °C for 1 hr), (c) Ni/PI film-110 (annealed at 110 °C for 1 hr), and (d) Ni/PI film-310 (annealed at 310 °C for 1hr).

Figure 4.5 plots the optimum treatment time with KOH and $\text{NiSO}_4 \cdot 6\text{H}_2\text{O}$ aqueous solution at 50 °C. When PI films were modified with KOH for 0, 2, 4, 6, 8, 10, 15, 20, 30, 60 and 180 min, the contact angle with water sharply decreased in the first 4 min. The decline slowed down from 4 min to 30 min. Finally, the contact angle remained constant from 30 min to 180 min. However, when ring-opened PI films were ion-exchanged with $\text{NiSO}_4 \cdot 6\text{H}_2\text{O}$ aqueous solution for 0, 5, 10, 20, 30, 60, 120 and 150 min, the surface contact angle rapidly increased from 9.7° to 47.9°, and then slowly increased from 47.9° to 57.5°, revealing that the Ni^{2+} ion exchange rate is very high. Therefore, the optimum treatment time with $\text{NiSO}_4 \cdot 6\text{H}_2\text{O}$ at 50°C was 5 min.

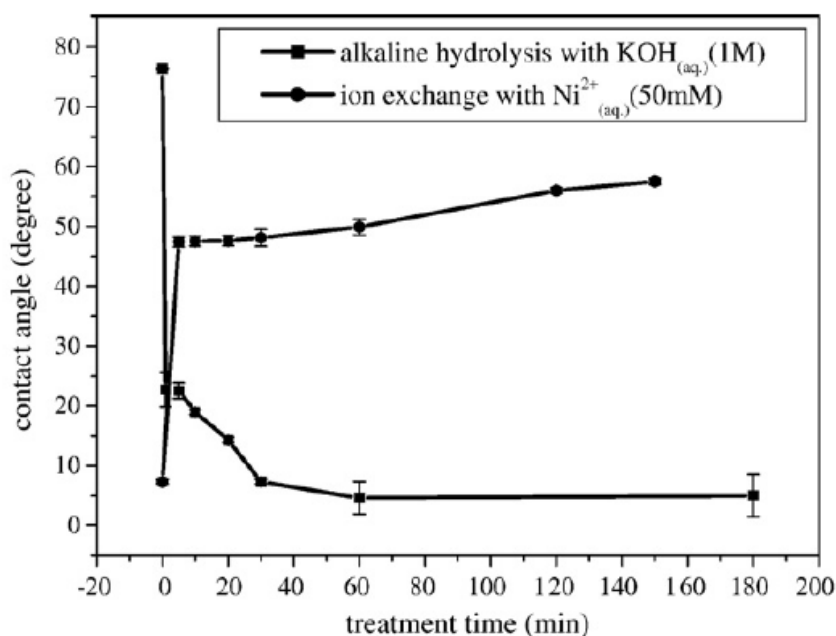


Figure 4.5 Variation of contact angle of PI surface in the alkaline hydrolysis after treatment with KOH and then ion exchange with nickel ions.

Table 4.4 presents the surface resistances and tape adhesion results for pristine PI and metalized films, measured using a four-point probe and the ASTM D3359-95 method [119]. The surface resistance of pristine PI was too high to be detected by the four-point probe instrument. The value for the Ni-NPs/ PI film (directly measured after the reduction of nickel ions) was lower, at $15.88 \text{ M}\Omega/\text{cm}^2$. However, after one day, the surface resistance of the modified Ni-NPs/ PI was undetectable. The Ni-NPs/ PI film with high surface energy was prone to be oxidized, and became less conductive, as shown in Fig. 4.8(G). In this figure, (a) the Ni-NPs/ PI film-d was measured directly after the reduction of nickel ion and (b) the Ni-NPs/ PI film-a was measured after one day using XPS. The NiO peak at 864 eV was clearly observed one day after that appeared from (a) Ni-NPs/ PI film-d. Ni/ PI films have higher conductivity, but samples that were annealed at different temperatures had different conductivities. The surface resistances of Ni/ PI films (without annealing), Ni/ PI films (annealing $110 \text{ }^\circ\text{C}/ 1 \text{ hr}$) and Ni/ PI films (annealing $310 \text{ }^\circ\text{C}/ 1 \text{ hr}$) were $6.44 \text{ }\Omega/\text{cm}^2$, $3.45 \text{ }\Omega/\text{cm}^2$ and $0.83 \text{ }\Omega/\text{cm}^2$, respectively. The higher annealing temperature corresponded to lower surface resistance. This relation is explained by the fact that high annealing temperature favored the crystallization of Ni and the restructuring of the grain boundary, as evidenced by Figures 4.4(b)-4.4(d). The surface resistance of Ni-B following electroless deposition [120] was of the same order of magnitude as observed experimentally herein. Tape adhesion test results demonstrated that no Ni-NPs/ PI film passed this test, but all of the Ni/PI films passed the Scotch-tape (ASTM D3359-95: with Scotch 610) the interfacial adhesion test between Ni and PI without any isolated spot or pit.

Table 4.4 Surface resistances and tape adhesion testing results of bare PI and metalized PI.

Sample (Mode: V/I)	Surface resistance (Ω/cm^2)	Tape adhesion performance per ASTM D3359-95
(a) PI films	---	No test
(b) Ni-NPs/ PI films-d	15.88M	No pass
(c) Ni-NPs/ PI films-a	---	No pass
(d) Ni/ PI films	6.44	Pass
(e) Ni/ PI films-110	3.45	Pass
(f) Ni/ PI films-310	0.83	Pass
(g) Ni/ Cu/ Ta/ SiO ₂ / Si-300	0.2	No test

(a) PI films: Bare PI films.

(b) Ni-NPs/ PI films-d: directly measured after modified.

(c) Ni-NPs/ PI films-a: measured after modified for over 1 day.

(d) Ni/ PI films: without annealing.

(e) Ni/ PI films-110: Ni/ PI films annealed 110 °C for 1 hr in vacuum.

(f) Ni/ PI films-310: Ni/ PI films annealed 310 °C for 1 hr in vacuum.

(g) Ni/ Cu/ Ta/ SiO₂/ Si-300: NiB film formed on Cu (100 nm)/ Ta (30 nm)/ SiO₂ (500 nm)/ Si substrate and annealed at 300 °C [120]

---: the surface resistance was not detected from four point probe.

Figure 4.6 shows the transparency and appearance of Ni-NPs/ PI films (Ni-NPs/ PI film treated with $\text{KOH}_{(\text{aq})}$ for X min/ $\text{NiSO}_{4(\text{aq})}$ for 5 min/ $\text{NaBH}_{4(\text{aq})}$ for 30 min at 50 °C) with various KOH treatment times ((A) 0 min, (B) 5 min, (C) 10 min, (D) 20 min, (E) 30 min, (F) 60 min, (G) 120 min). In Fig. 6(A), the pristine PI film is yellow-brown and very transparent. In Figs. 6(B)-(F), the Ni-NPs distributed on PI films were black and became darker as the KOH treatment time increased. In Figures 4.6(F) and 4.6(G), the samples were warped and changed color from black to silver. Samples (B)-(G) of Ni-NPs/ PI films easily underwent electroless deposition.

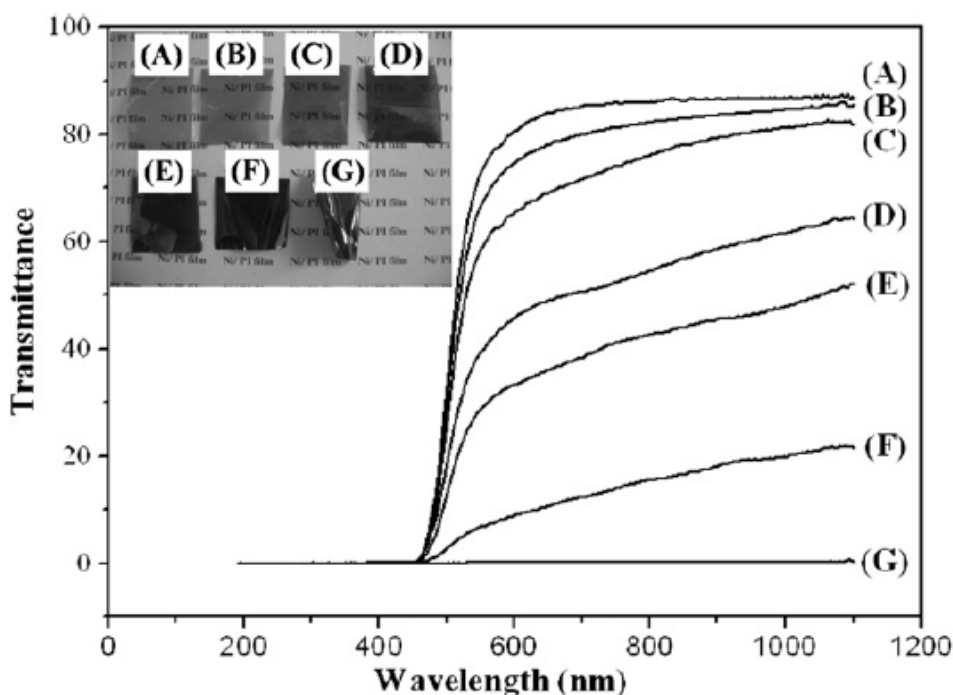


Figure 4.6 Dependence of transparency and appearance of Ni-NPs/ PI films (Ni-NPs/ PI film treated with $\text{KOH}_{(\text{aq})}$ for X min/ $\text{NiSO}_{4(\text{aq})}$ for 5 min/ $\text{NaBH}_{4(\text{aq})}$ for 30 min at 50 °C) on hydrolysis time (X min) during KOH treatment: (A) 0 min, (B) 5 min, (C) 10 min, (D) 20 min, (E) 30 min, (F) 60 min, (G) 120 min.

Figure 4.7 displays AFM topview diagrams of the nanostructured Ni-NPs/ PI films for different KOH treatment times; (A) 0 min, (B) 5 min, (C) 30 min, (D) 60 min. In Figure 4.7(A) the pristine PI film was smooth and had a uniform surface topography. After KOH treatment for 5 min, a few of nanosized nickel particles of size 85 nm were present, as observed in Figure 4.7(B). As the KOH treatment time increased, more Ni nanoparticles formed on the surface of the PI films. After a KOH treatment time of 30 min or 60 min, as display in Figures 4.7(C)-(D), the Ni-NPs were more uniform and denser. Table 4.1 presents that, the dependence of the surface roughness and average Ni particle size of Ni-NPs/ PI films on the KOH treatment time ((a) 0 min, (b) 10 min, (c) 20 min, (d) 30 min, (e) 60 min, (f) 120 min), as determined using AFM. In Table 4.1(a), the surface roughness was 0.89 nm and no Ni-NP was present on PI. In Table 4.1(b)-(e), the surface roughness was 23.90, 11.64, 14.30 and 10.00 nm, respectively, and the average particle sizes of Ni-NPs were 269, 131, 161 and 113 nm, respectively. In Table 1(f), the surface roughness was 5.99 nm and the surface of the PI film was uniformly covered with Ni particles, which formed a continuous Ni layer.

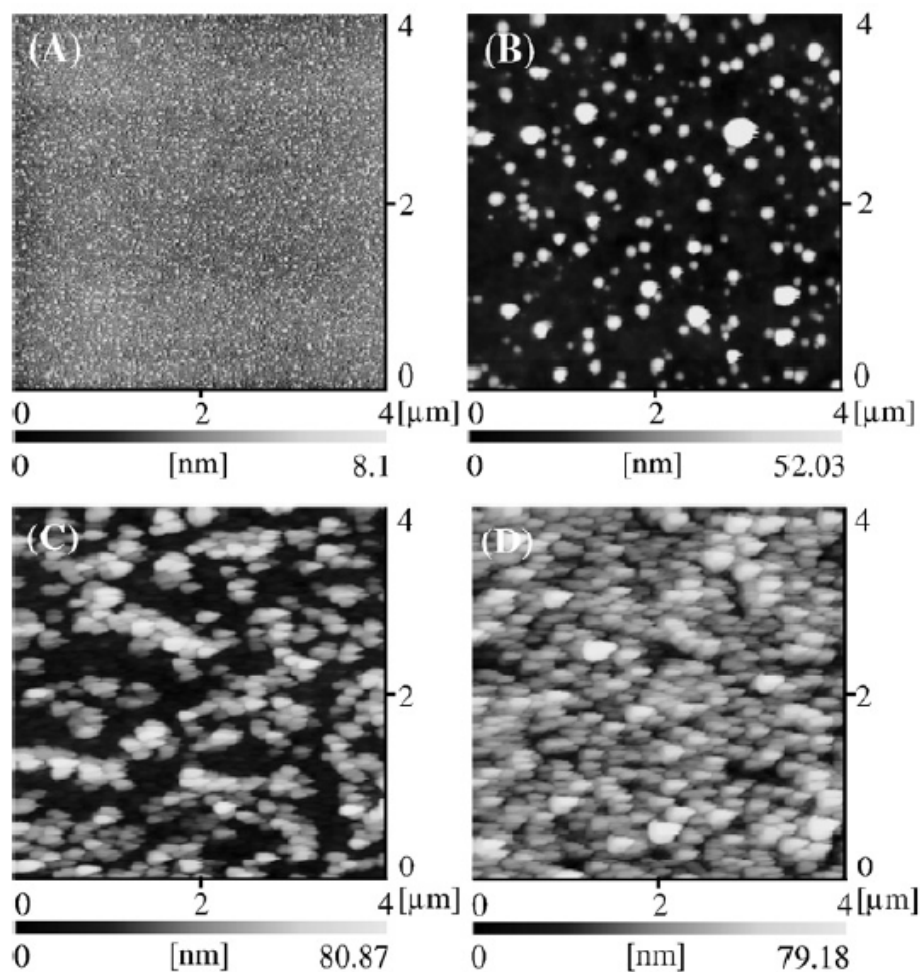
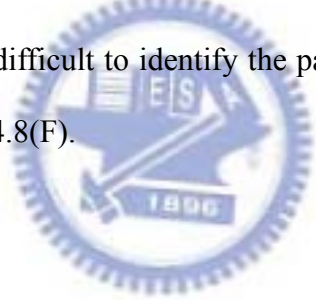


Figure 4.7 AFM photographs of nanostructured Ni-NPs/PI films (Ni-NPs/PI film treated with $\text{KOH}_{(aq)}$ for 10 min/ $\text{NiSO}_{4(aq)}$ for 5 min/ $\text{NaBH}_{4(aq)}$ for 30 min at 50 °C) for various hydrolysis times with KOH treatment: (A) 0 min, (B) 5 min, (C) 30 min, (D) 60 min. (top-view diagram; range of z is 200 nm).

Figure 4.8 presents the surface topographies of electroless nickel layers that were grown on Ni-NPs/ PI films (Ni-NPs/ PI film treated with $\text{KOH}_{(\text{aq})}$ for 30 min/ $\text{NiSO}_{4(\text{aq})}$ for 5 min/ $\text{NaBH}_{4(\text{aq})}$ for 30 min at 50 °C), obtained using FE-SEM. All scale bars in Figures 4.8(A)-4.8(F) were 200 nm, and the dipping times in EN solution were 0, 2, 4, 6, 10, 15 min, respectively. Figure 8(A) displays the original Ni-NPs deposited on modified PI surface, where the sizes of the spherical nickel nanoparticles were approximately 50 nm, which size is the same as in Figure 4.7(C). Dipping in EN solution at 50 °C for 2 min increased the size of the Ni-NPs from 50 nm to 100 nm, as shown in Fig. 8(B). Electroless nickel treatment at 50 °C for 4, 6 and 10 min increased the particle size had from 150 nm to 300 nm, and the surface morphology of the Ni/ PI films in Figures 4.8(C)-4.8(E) was denser and smoother. Finally, after it had been treated for 15 min, the nickel film had a flat and smooth surface and was difficult to identify the particle sizes and grain boundaries of the nickel particles in Figure 4.8(F).



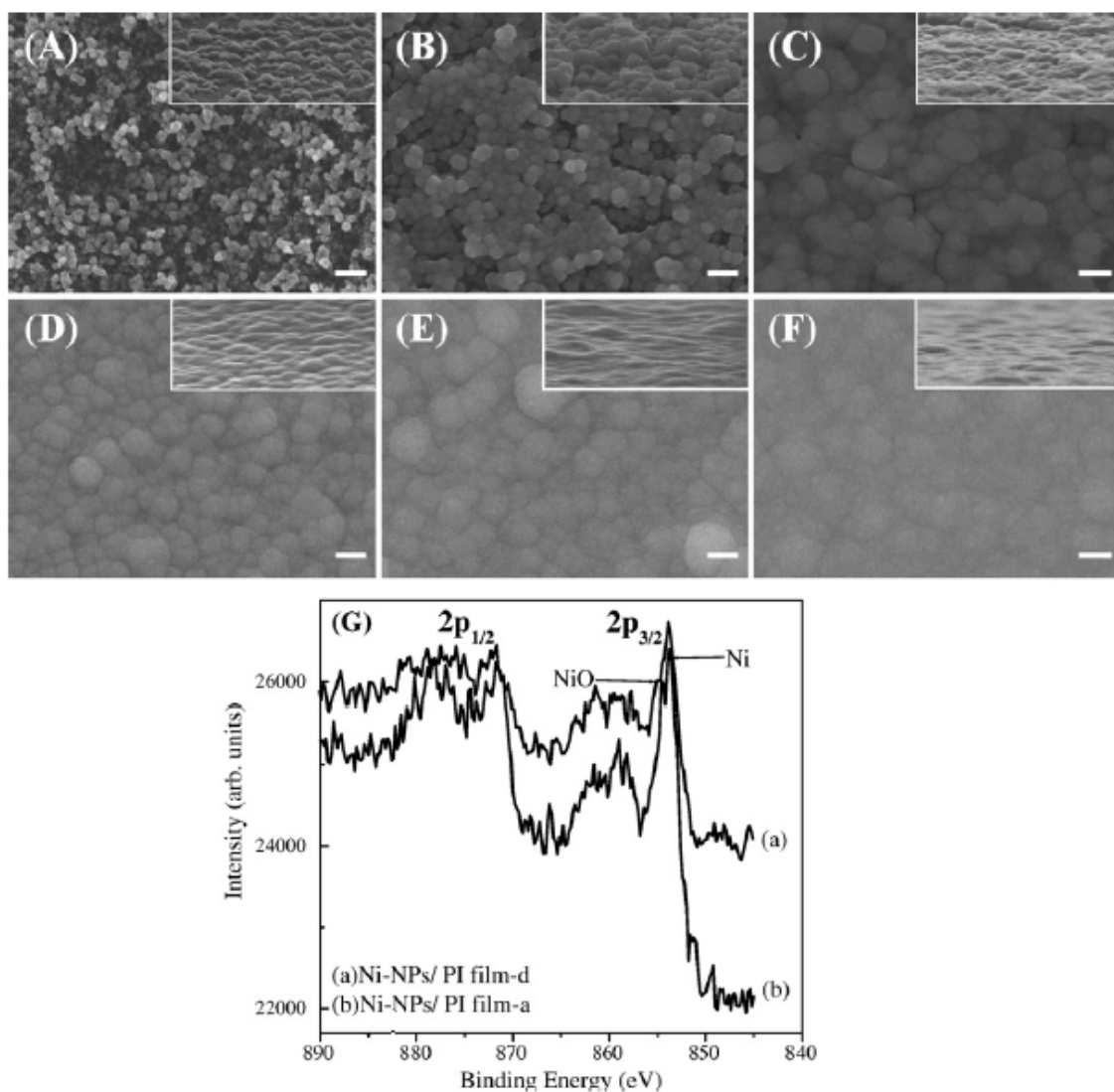


Figure 4.8 FE-SEM images of electroless-plated nickel on Ni-NPs/PI films (Ni-NPs/PI film treated with $\text{KOH}_{(aq)}$ for 30 min/ $\text{NiSO}_{4(aq)}$ for 5 min/ $\text{NaBH}_{4(aq)}$ for 30 min at $50\text{ }^{\circ}\text{C}$) at $50\text{ }^{\circ}\text{C}$ for (A) 0 min, (B) 2 min, (C) 4 min, (D) 6 min, (E) 10 min, (F) 15 min. White bars represent 200 nm. (left: top-view, right: tilt 45° -view). XPS spectra of Ni-NPs/PI films. (a) Ni-NPs/PI film-d (measured directly), (b) Ni-NPs/PI film-a (measured after one day).

Figures 4.9 and 4.10 present cross-sectional TEM images of the Ni-NPs/ PI film and the Ni/ PI film, respectively. The Ni-NPs/ PI film was treated with $\text{KOH}_{(\text{aq.})}$ at 50 °C for 5 min, underwent ion exchange with $\text{NiSO}_4 \cdot \text{H}_2\text{O}_{(\text{aq.})}$ at 50 °C for 5 min, and was then reduced by $\text{NaBH}_{4(\text{aq.})}$ at 50 °C for 30 min. The pre-treatment of the Ni/ PI film in Figure 4.10 was the same as that in Figure 4.9 and the EN solution was then used to increase the thickness of the nickel layer at 50 °C for 10 min without any annealing. Figure 4.9 shows that the thickness of the Ni-NPs layer was 82 nm. Figures 4.9(A) and 4.9(B) are TEM images of the outside and the inside of the Ni-NPs layer, respectively. Figures 4.9(A) and 4.9(B) indicate that Ni-NPs were discontinuous in the layer with particle sizes of 10 nm. In Figure 4.10, the three layers in this Ni/ PI film were the Ni layer, the Ni-NPs layer and the PI layer in that order. The TEM photographs show that in the Ni layer, the metal was continuous, but in the Ni-NPs layer, Ni-NPs were dispersed in the polymer and interlocked therewith. The thickness of the Ni layer was 382 nm and that of the Ni-NPs layer was 82 nm. EDX analysis confirmed the structure of these three layers, as shown in Figure 4.10. The EDX intensity of copper signals for each layer was from the TEM copper grid, and the oxygen and carbon signals were from PI. Accordingly, the EDX results verified that the A-area was composed of electroless plated nickel; the B-area was composed of Ni-NPs and polymer, and the C-area comprised PI without Ni.

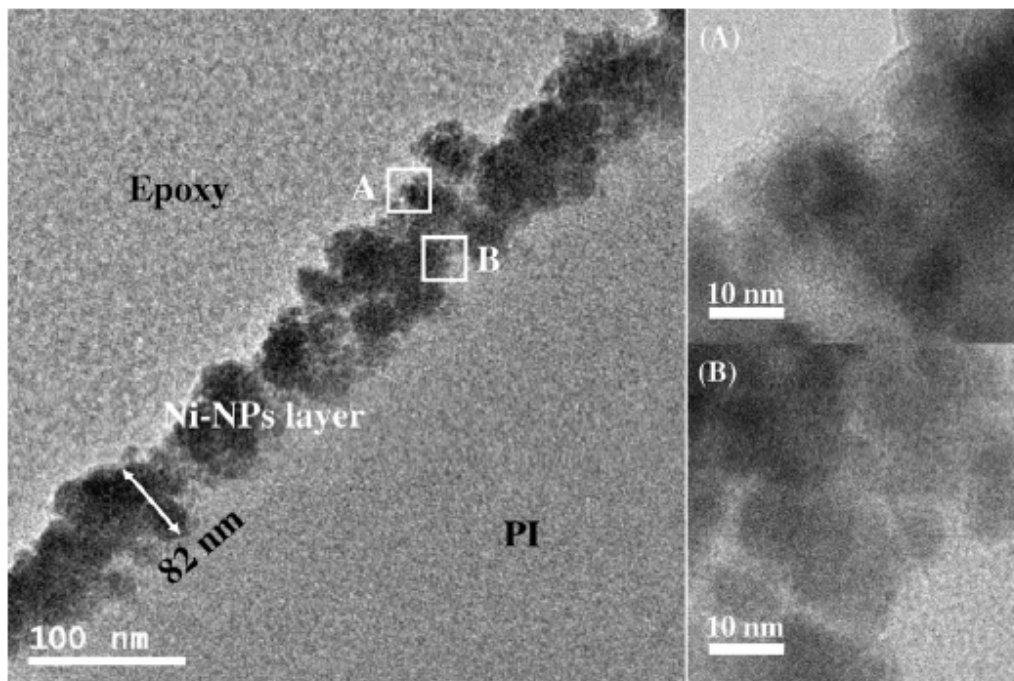


Figure 4.9 TEM photographs of cross section of Ni-NPs/PI film (Ni-NPs/PI film treated with $\text{KOH}_{(aq)}$ for 10 min/ $\text{NiSO}_{4(aq)}$ for 5 min/ $\text{NaBH}_{4(aq)}$ for 30 min at 50 °C). The bar represents 100 nm. The A-area and B-area are outside and inside the Ni-NPs layer, respectively.

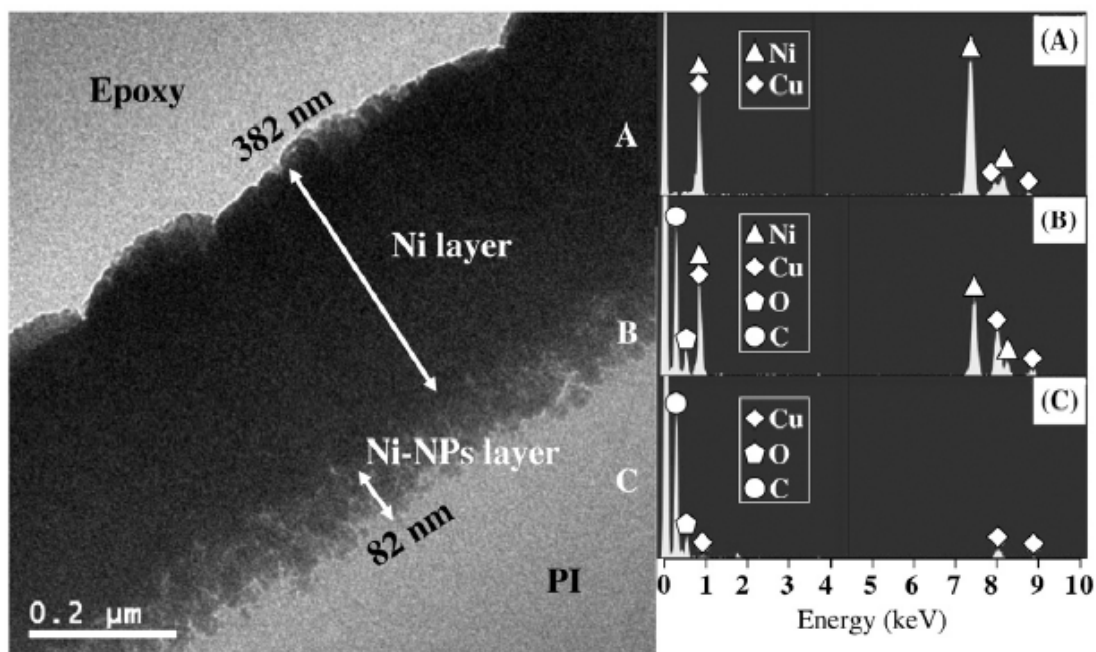
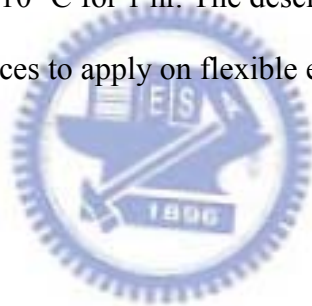


Figure 4.10 TEM photographs (left) and EDX analysis (right) of cross section of surface-nickelized PI films: A-the Ni layer, B-the Ni-NPs layer, C-PI film.

4.4 Conclusion

Conductive Ni/PI films are fabricated using a fully chemical solution-based process without Pd, and adhere strongly between polyimide and nickel phases. Unlike traditional processes, this process does not require the use of Pd catalyst. Additionally, it is convenient for preparing conductive Ni on one or both sides of PI films. Ni-NPs can be homogeneously distributed on the PI surface after reduction by aqueous NaBH₄. After electroless plating, the Ni layer exhibits excellent interfacial adhesion on the PI surface and passes the Scotch-tape test. The interlocking of the nickel layer with the PI layer may contribute to the interfacial adhesion. Measurements of surface conductivity reveal that the surface resistance of Ni-NPs is $1.6 \times 10^7 \Omega/\text{cm}^2$, but that of Ni/PI film is $0.83 \Omega/\text{cm}^2$ after EN treatment and heating at 310 °C for 1 hr. The described method is good for electroplate metal onto nickelized PI surfaces to apply on flexible electronics.



4.5 Appendix

There was a latent roughness difference through fabricating PI films on rigid substrates, especially occurring in soft structure of PI films. Interestingly, the contact angle difference could be obviously observed on both sides of PI through the same condition of alkaline hydrolysis treatments, especially occurring in soft structure of PI. In order to use this technique for applying in roll-to-roll process, NiPI films were further investigated to realize the surface morphology and adhesion differences of in-situ processing Ni thin layer on two sides of PI films. In this appendix, compared to PMDA-ODA based PI, I selected the softer structure of PI to further investigate the properties differences of fabricating Ni layers on two sides of PI films. Figure 4.11 plots the contact angle difference of optimum treatment time with $\text{KOH}_{(\text{aq.})}$ (5 M) at 50 °C on both sides of PI films. When PI films were modified with KOH for 0, 1, 3, 5, 7, 10, 12, 15 and 20 min, the contact angle with water sharply decreased in the first 1 min and the decline slowed down from 1 min to 20 min on the A side. Comparison with another side, the contact angle with water slowly decreased from 0 to 10 min on the B side, and it meant the imide ring on the A side of PI could be easier to be opened than the B side. The surface-roughness of film was presumed to cause the ability of imide ring opening by AFM testing. For example, a higher ability of imide ring opening was obtained from the rougher surface of the A side ($R_{\text{ms}}= 2.21 \text{ nm}$) than the B side ($R_{\text{ms}}= 1.58 \text{ nm}$).

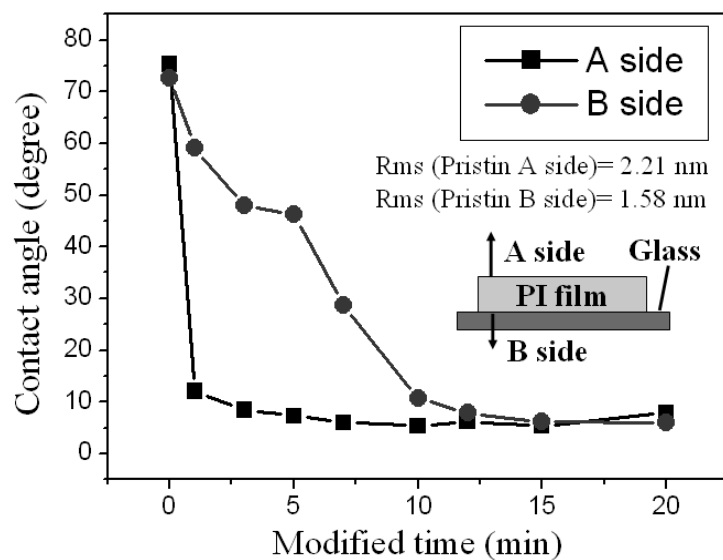


Figure 4.11 Variations of contact angle of two PI sides in the alkaline hydrolysis after treatment with $KOH_{(aq)}$.



Figure 4.12 presents cross-sectional TEM images of the Ni/PI film on both sides of PI films. The Ni-NPs layers, PI films were treated with $\text{KOH}_{(\text{aq})}$ at 50 °C for 10 min, underwent ion exchange with $\text{NiSO}_4 \cdot \text{H}_2\text{O}_{(\text{aq})}$ at 50 °C for 5 min, and reduced by $\text{NaBH}_{4(\text{aq})}$ at 50 °C for 5 min, and the EN solution was then used to increase the thickness of the nickel layer at 50 °C for 10 min without any annealing. On the A side of PI films, the TEM photographs showed that the thickness of the Ni-NPs layer was ca. 290 nm and Ni thin layer was ca. 180 nm [Figure 4.12(A)]. In addition, on the B side, it could be observed that the thickness of the Ni-NPs layer was ca. 70 nm and the Ni layer was ca. 180 nm [Figure 4.12(B)]. Based on the variation of thickness of Ni-NPs layer [composed of Ni-NPs and poly(amic acid) (PAA)], the further investigation of peel strengths in Cu/NiPI systems was important to realize whether the Ni-NPs layer would cause some interface problems.

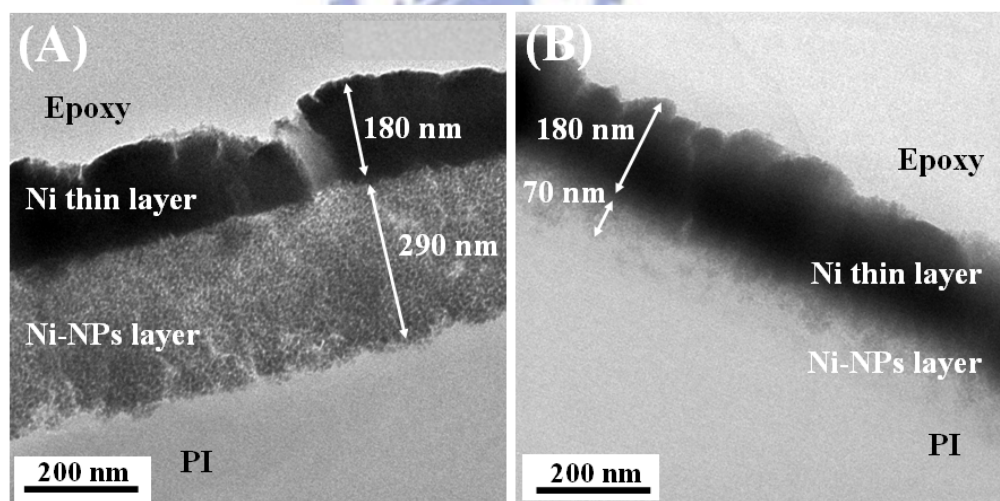


Figure 4.12 TEM photographs of cross section of Ni-NPs/PI film (Ni-NPs/PI film treated with $\text{KOH}_{(\text{aq})}$ for 10 min/ $\text{NiSO}_{4(\text{aq})}$ for 5 min/ $\text{NaBH}_{4(\text{aq})}$ for 5 min/ EN solution for 10 min at 50 °C). (A) A side of PI film. (B) B side of PI film.

Figure 4.13 shows the tendency of relative peel strengths on both sides of PI films in Cu/PI systems. The best peel strengths from A and B sides were 0.989 kg/cm and 0.955 kg/cm, respectively (Cu layer, 35-40 μ m). As the results of preliminary peel strength and TEM images responses, the NiPI film was presumed to be a better adhesion layer through forming the heterojunction interface between Ni and PI phases to enhance the adhesion property.

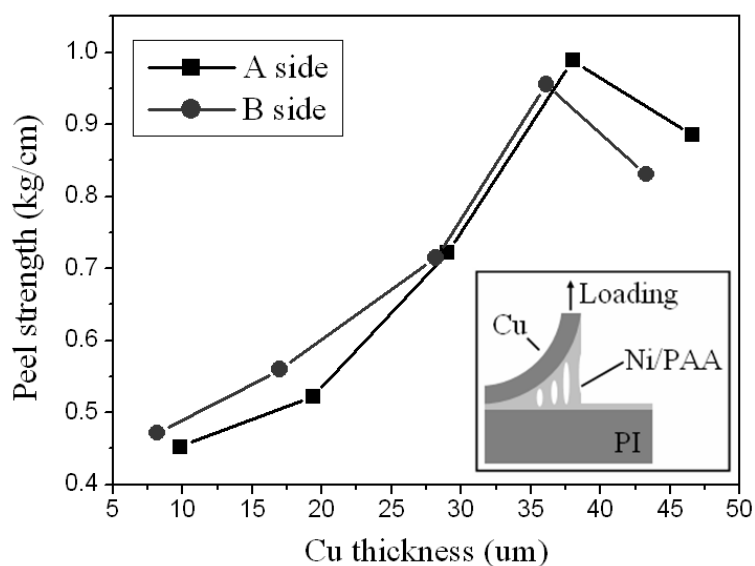
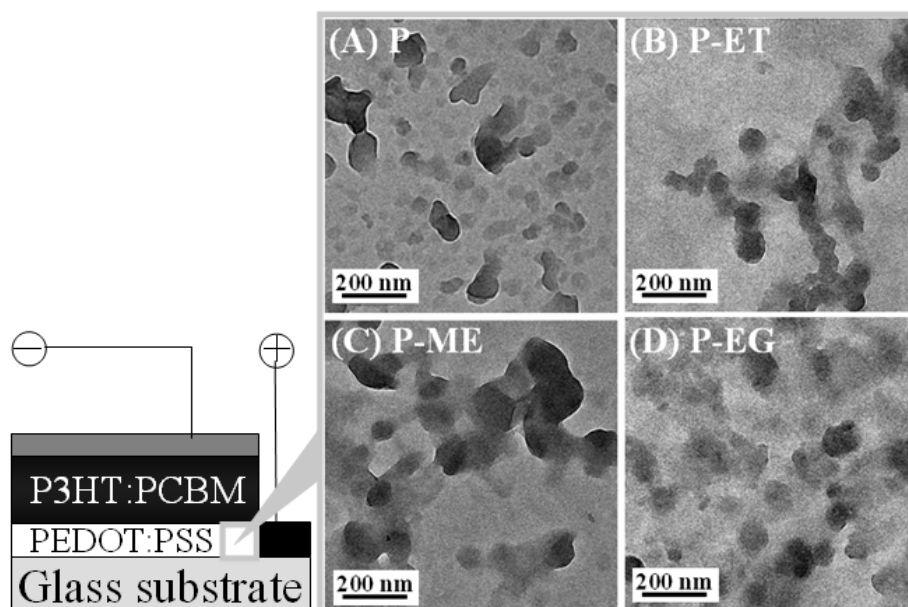


Figure 4.13 Peel strengths of two sides of Cu/Ni/PI films and Cu with various thicknesses.

Chapter 5

High-Conductivity Poly(3,4-ethylenedioxythiophene):Poly(styrene sulfonate) Film for Use in ITO-Free Polymer Solar Cells



In this study, we devised a simple method to enhance the conductivity of poly(3,4-ethylenedioxythiophene)-poly(styrene-sulfonate) (PEDOT:PSS) films through spin-coating with various surface-modified compounds, and then applied this technique to the preparation of ITO-free polymer solar cells (PSCs). The electrical conductivity of PEDOT:PSS films can be increased by more than two order of magnitudes merely by spin-coating a compound containing one or more polar groups—such as ethanol, methoxyethanol, 1,2-dimethoxyethane, and ethylene glycol—onto the films. In this paper,

we discuss the phenomena occurring through conductivities, morphologies, and chemical properties of the modified PEDOT-PSS films as determined using Raman spectroscopy, a four-point probe, scanning electron microscopy (SEM), atomic force microscopy (AFM), transmission electron microscopy (TEM), and X-ray photoelectron spectroscopy (XPS). The schematic 3D morphological model of directly solvent-modified PEDOT:PSS films is presumed for ITO-free devices. The desirable conductivity enhancements of these materials make them attractive candidates for use as anode materials in ITO-free PSCs.

5.1 Introduction

The emerging field of polymer photovoltaics (PPVs) is flourishing because these materials appear to have promising technological applications as a result of their of light weight, high flexibility, and solution-processability. [121-123] The power conversion efficiency (PCE) of PPVs has been improved up to 5% under A. M. 1.5G based on a blend film composed of poly(3-hexylthiophene) (P3HT) as the donor and [6,6]-phenyl-C₆₁-butyric acid methyl ester (PCBM) as the acceptor, [121, 122] additionally, the tandem cells with PCE of more than 6.5% were achieved by all-solution processing. [123] This encouraging progress is advancing such materials toward commercial application, where they will eventually compete with inorganic photovoltaics (PVs). Recently, the PPVs with low band gap (LBG) materials, [124-131] processing into large area, [132, 133] long-term stability [134, 135] and various transparent anodes [136-154] of devices were also widely investigated. LBG polymers were developed to harvest the solar spectrum efficiently in order to generate more photocurrent. The understanding of the complex interplay in large transporting distance and the chemistry that takes place during degradation and failure of device enable devices for large area and longer lifetime. In terms of transparent conducting materials, the choice of applied anode materials is

generally limited to indium tin oxide (ITO), carbon nanotube networks, [136, 137] silver gratings, random mesh of silver nanowires [138, 139] and poly(3,4-ethylenedioxythiophene):poly(styrene sulfonate) (PEDOT:PSS). [140-154] Unfortunately, the high cost of high-quality ITO and its lack of flexibility can limit the solar energy applications of devices incorporating it as an anode material; the limited supply of indium and the transparency of ITO toward visible light are additional problems. Carbon nanotube network films appear to be a suitable alternative: they can be which prepared through solution processing and they exhibited high conductivity and flexibility. [136, 137] Such cells do, however, have their problems. For example, the nature of the transparent single-wall carbon nanotube (SWNT) network films is not always well defined; typically, SWNT films are mixtures of metallic and p-doped nanotubes. In addition, it is necessary to add PEDOT:PSS to adjust the work function of the SWNTs and to avoid shorting of the device by having the metallic nanotubes transport electrons from the PCBM materials to the transparent anode. By using vapor-phase polymerization (VPP), the PPV device with desirable conductivity of VPP-PEDOT-Tos films have been demonstrated by Krebs et al., [148] however this material is not solution processable and work function (WF) suggested by Lindell et al. is suitable for cathode in PPV device (WF= 4.3 eV). [151] The silver grating or random mesh of silver nanowires systems were promising methods to reduce the sheet resistance as electrodes to apply in PPVs, [138, 139] however the further coating of PEDOT:PSS was needed to adjust the work function and avoid shorting. In short, the most promising material at present is PEDOT:PSS, but it remains a necessary challenge to improve the conductivity of PEDOT:PSS films up to the level exhibited by ITO. PEDOT:PSS films are already used in most organic optoelectronic devices to flatten the ITO surface and tailor the work function of the anodes for hole collection. PEDOT:PSS suffers, however, from low conductivity, which restricts its use as a true electrode material; the conductivity of commercially available PEDOT:PSS (Baytron P, Bayer Corporation),

for example, is ca. 1 S cm^{-1} , which is lower than that of ITO by three orders of magnitude.

The conductivity of PEDOT:PSS films can be enhanced through processing with certain solvents and other compounds. [140, 142-148, 150-153] Kim et al. reported that addition of a high-dielectric solvent, such as dimethyl sulfoxide or *N,N*-dimethylformamide, [141] into an aqueous solution of PEDOT:PSS can enhance the conductivity of the resulting PEDOT:PSS films by more than one order of magnitude as a result of weakening the columbic attraction between the counter ions and the charge carriers. Sorbitol, ethylene glycol, and other alcohols [140, 142-147, 150, 152, 153] comprise another set of inert secondary dopants that enhance the conductivity. Although the exact origin of the conductivity enhancement has not been determined, several mechanisms have been proposed. It is generally believed, however, that the presence of the solvent improves the morphology of the films, providing good percolating paths among the PEDOT-PSS domains (PEDOT-rich regions) and transforming the molecular structure.

Our goal for this study was to develop a simple method for modifying the electrical conductivity of PEDOT:PSS films intended for use as electrodes in ITO-free solar cells. We found that high-conductivity PEDOT:PSS films could be obtained simply through spin-coating of a solvent onto pre-coated PEDOT:PSS films. We employed Raman and UV-Vis spectroscopy, a four-point probe, scanning electron microscopy (SEM), tapping-mode atomic force spectroscopy (AFM), transition electron microscopy (TEM), and X-ray photoelectron spectroscopy (XPS) to determine the origin of the conductivity enhancement. We found that the performance of the PPVs was related to the surface morphologies, chemical structures, and electrical conductivities of the PEDOT:PSS films. We performed a comprehensive investigation of the effects of alcoholic and ethereal solvents, including methoxyethanol, ethanol, and 1,2-dimethoxyethane, to determine the driving force for the conductivity enhancement of the PEDOT:PSS films.

5.2 Experimental Details

5.2.1 Materials and Polymer Solar Cells

The high-conductivity PEDOT:PSS anodes were prepared using a two-step method. PEDOT:PSS (Baytron P V4071 from Bayer Corporation) was filtered through a 0.45 μm filter prior to being deposited onto cleaned glass substrates at a thickness ca. 50 nm through spin-coating at 4500 rpm in the air. Surface-modifying solvents, namely ethanol (with one hydroxyl group), methoxyethanol (one hydroxyl and one ether group), 1,2-dimethoxyethane (two ether groups), and ethylene glycol (two hydroxyl groups), were spin-coated onto the pristine PEDOT:PSS films, which were then dried at 150 $^{\circ}\text{C}$ for 1 hr inside a glove box. A blend [0.9:1 (w/w), 17 mg mL^{-1} in dichlorobenzene (DCB) of [6,6]-phenyl-C61-butyric acid methyl ester (PCBM) and poly(3-hexylthiophene) (P3HT; Rieke Met. Inc.) was stirred overnight in DCB, filtered through a 0.2- μm poly(tetrafluoroethylene) (PTFE) filter, and then spin-coated (450 rpm, 60 s) on top of the PEDOT:PSS layer. The device was completed by coating 30- and 100-nm-thick layers of Ca and Al, respectively, under pressures of less than 10^{-6} torr. The cell was then encapsulated using UV-curing glue (Nagase, Japan). The active area of all devices, defined through the shadow mask to limit the area of input light and the selective-area sizes of masks were 0.01 and 0.02 cm^2 . Figure 5.1 displays the architecture (left side; right side (under)), photograph (right side (upper)) of ITO-free polymer/fullerene solar cells.

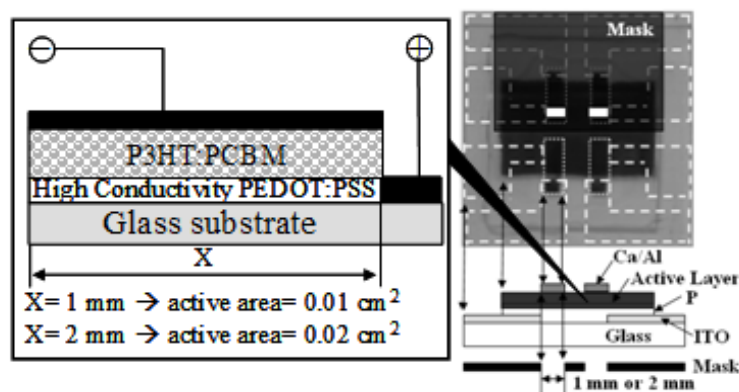


Figure 5.1 Architecture and photograph of the ITO-free polymer/fullerene solar cell.

5.2.2 Instrumentation

The sheet resistances of the PEDOT:PSS films were measured using a four-point probe; the average of the measured values is reported. The transmittance spectra were recorded using an HP8453 UV–Vis spectrometer. The Raman spectra of the polymer films were recorded using a Renishaw system 2000 micro-Raman system in conjunction with a 632.8-nm HeNe laser as an excitation source. The surface morphologies and phase changes of the PEDOT:PSS films were analyzed using a VEECO DICP-II AFM operated in tapping mode (silicon tips on silicon cantilevers with a spring constant of 2 N m^{-1} and a set point of ca. 0.8–0.9) in air. A JEOL JSM-6500F SEM was employed to investigate the thicknesses and morphologies of the PEDOT:PSS films. XPS spectra were recorded using a VG Scientific Microlab 350 spectrometer operated in the constant analyzer energy mode with a pass energy of 50 eV, with $\text{MgK}\alpha$ (1253.6 eV) radiation as the excitation source (with normal emission detected). Samples for TEM analysis were prepared through spin-casting of the PEDOT:PSS solution onto the P3HT film (on a glass substrate). The P3HT film was treated with oxygen plasma for 3 min prior to the deposition of PEDOT:PSS. The films were then floated onto THF and placed on a 200-mesh copper TEM grid (Agar Sci., Inc.). The modified PEDOT:PSS films were then prepared according to the procedures described above. TEM images were recorded using a JEOL-2010 TEM and the internal charge-coupled device (CCD) camera. XPS measurements were performed at room temperature and pressures of less than 10^{-10} torr. Current–voltage (I – V) curves of the PSC devices were measured using a computer-controlled Keithley 2400 source measurement unit (SMU) equipped with a Peccell solar simulator under the illumination of AM 1.5 (100 mW cm^{-2}). The spectral irradiance data of light source is similar to AM 1.5G solar spectrum (spectral mismatch $<5\%$ in the range from 350 nm to 800 nm). The illumination intensity was calibrated using a standard Si photodiode detector equipped with a KG-5 filter. All of these measurements were performed under an ambient

atmosphere at room temperature.

5.3 Results and Discussion

5.3.1 The Origin of Conductivity Enhancement of Surface-modified PEDOT:PSS Films

Table 5.1 lists the sheet resistances of the PEDOT:PSS films, as measured using a four-point probe. The resistance of the pristine PEDOT:PSS (P) film with annealing at 150 °C for 1 hr was ca. 1011 k Ω cm⁻². When the PEDOT:PSS films were modified with ethanol (P-ET), methoxyethanol (P-ME), 1,2-dimethoxyethane (P-DME), and ethylene glycol (P-EG) and then annealed at 150 °C for 1 hr under a nitrogen atmosphere, the sheet resistances decreased to 118.6, 7.3, 604.3, and 5.1 k Ω cm⁻², respectively. Previous reports of the solvent-doping effect have suggested [140, 142-147, 150, 152, 153] that alcoholic solvents enhance the conductivity to a greater extent than do ethereal solvents. We observed conductivity enhancement after the addition of ethanol—in direct contrast to the findings of a previous study, which suggested that alcoholic compounds containing only one hydroxyl group, such as methanol, ethanol, and heptanol, did not enhance the conductivity after they had been added into the aqueous PEDOT:PSS solution. [144, 147] We suspect that the boiling point of the additive is an important factor in such solvent-doping systems. For example, a solvent having a low boiling point would evaporate before or with water after spin-coating of the PEDOT:PSS solution; if so, then conductivity enhancement would not be observed. In our approach, however, solvent treatment following film formation would provide solvents with only one OH group, such as ethanol, the opportunity to change the conductivity of the pristine PEDOT:PSS film. The phenomenon of conductivity enhancement of solvent-modified films is discussed in detail below. If transparent electrodes are to be used in photovoltaic devices, they must have high transparency in the visible region of the spectrum. Thicker PEDOT:PSS films

will have transmittance and vertical conductivity problem. In this study, 50 nm thickness of PEDOT:PSS film was chosen and the transmittance losses of our various solvent-modified PEDOT:PSS films (50 nm thickness) on glass were similar (ca. 7%; Table 5.1).

Table 5.1 Sheet resistances and transmittances of the PEDOT:PSS films.

Anodes	b.p. of modified compound/ ^o C	Sheet resistance/ K Ω cm ²	Transmittance loss at 550 nm (%)
P	none	1011.0 \pm 58.5	7.25
P-ET	78	118.6 \pm 11.2	7.48
P-ME	124 125	7.3 \pm 0.9	7.34
P-DME	85	604.3 \pm 126.6	6.34
P-EG	196 198	5.1 \pm 1.9	7.36



To determine the mechanism for the conductivity enhancement of the PEDOT:PSS films at the molecular level, we recorded the Raman spectra of the pristine and treated PEDOT:PSS films (Figure 5.2). To clearly understand the transformation of the thiophene structures, the presented Raman spectra have been normalized with respect to the intensity of the quinoid peak at 1422 cm^{-1} . The most obvious difference between the pristine and modified PEDOT:PSS films was that the shoulder signal at 1445 cm^{-1} become weaker after solvent modification. The modified films exhibited a narrower band at 1445 cm^{-1} , relative to the broader band of P. Yang and co-workers suggested that for P films, the vibrations at 1422 and 1445 cm^{-1} represent to the quinoid and benzoid structures, respectively. [144, 147] Our Raman spectra suggest that the conductivity enhancement was due in part to the benzoid structures transforming into quinoid structures. Although the variations of their conductivities were large, the Raman spectra of the P-ME, P-DME and P-EG films were all similar. This finding suggests that the transformation of the thiophene structures was not the only factor enhancing the conductivity of solvent-modified PEDOT:PSS films.

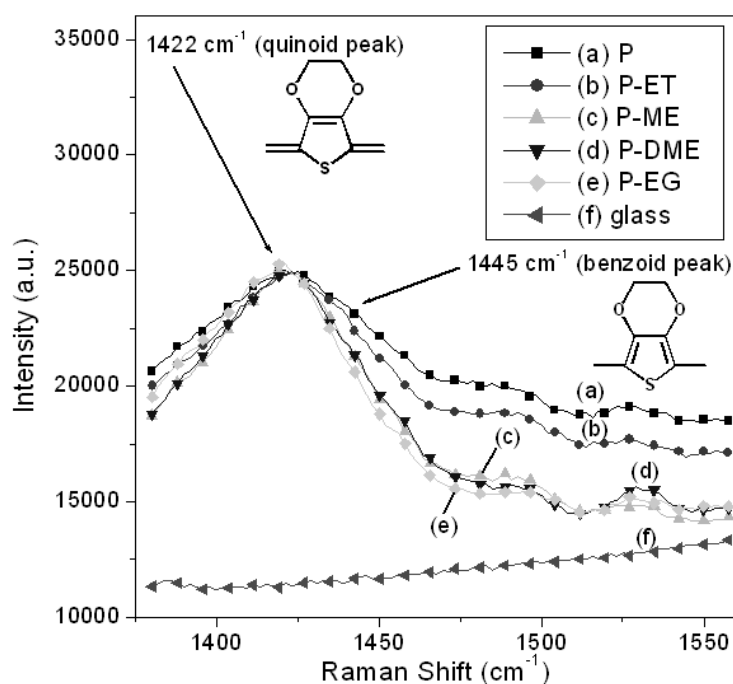


Figure 5.2 Raman spectra of PEDOT:PSS films excited using HeNe laser at 632.8 nm.

Figure 5.3 presents SEM cross-sectional images revealing the thickness and surface topography of the solvent-modified PEDOT:PSS films on glass substrates. Figure 5.3(a) indicates that the thickness of the P film was ca. 50 nm; its topography was flat and uniform. When the modifying solvent possessed fewer than two hydroxyl groups (i.e., for ET, ME, and DME), the thicknesses and topographies of the films did not change significantly after solvent modification [cf. Figures 5.3(b)–(d)]. In contrast, EG—a solvent featuring two hydroxyl groups—has a dramatic effect on the thickness and topography of the PEDOT:PSS film [Figure 5.3(e)], which became thinner and exhibited a rougher surface morphology. The PEDOT:PSS films generally swell and soften upon the addition of EG.

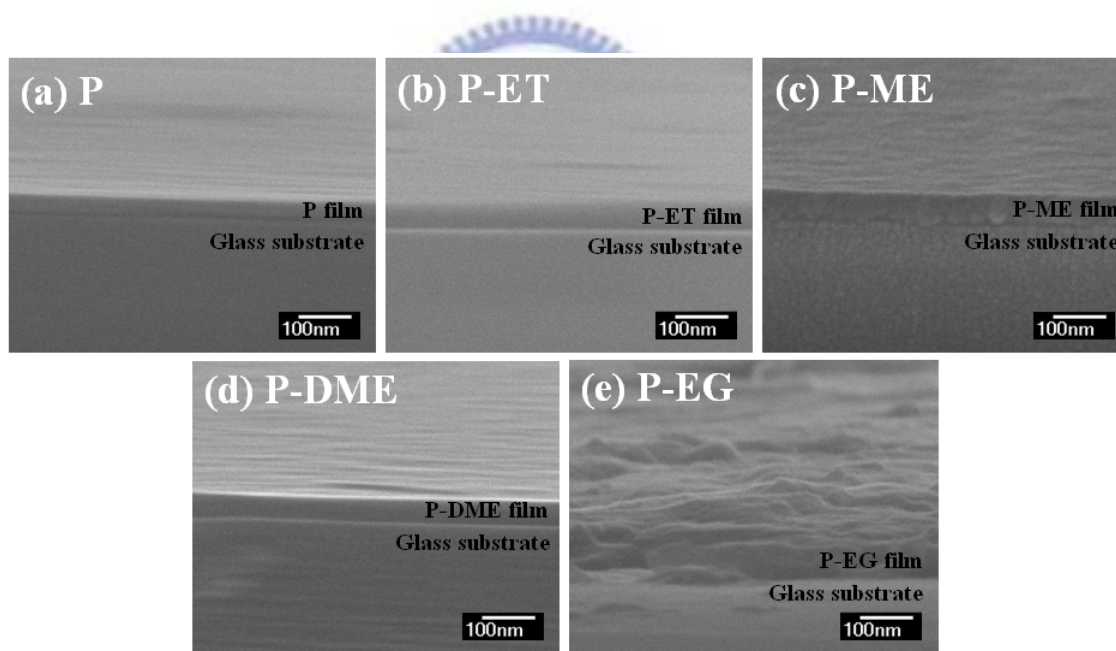


Figure 5.3 SEM cross-sectional images of solvent-modified PEDOT-PSS films on glass substrates. (a) P, (b) P-ET, (c) P-ME, (d) P-DME and (e) P-EG.

To investigate if and how any other effect was occurring, we employed AFM in the tapping mode (Figure 5.4) to characterize the origin of the conductivity enhancement through measurements of the topographies and phase diagrams of PEDOT:PSS films ($0.5 \times 0.5 \text{ m}^2$ area) coated on glass substrates. The phase image of the P film [Figures 5.4(A) and 5.4(B)] was similar to that reported by Crispin et al., [150] with separated PEDOT-PSS domains (PEDOT-rich regions) and PSS domains (PSS-rich regions); the domain sizes and elongated structures were ca. 20–30 nm. In the phase image, the hard domains appear as bright regions, which we attribute to PEDOT-PSS domains, whereas the dark regions denote the soft segments that belonged to excess PSS domains. [150] Although the P-ME and P films had similar topographic characteristics, the magnified phase images reveal some variations. We observe that ME induced a phase separation that was characterized by segregation of the excess PSS domain surrounded by a continuous PEDOT-PSS phase with higher variation of degree than the P film on phase images. These continuous PEDOT-PSS domains are better percolating pathways that result in higher conductivity. The PEDOT:PSS film had a rougher topography after treatment with EG [Figure 5.4(E)], consistent with swelling and softening of the film. The PEDOT-PSS and PSS domains were distinguishable in the phase image with lower variation of degree than the P film on phase images; indeed, the area of the PSS domains (darker regions) underwent an obvious decrease on the polymer surface [Figure 5.4(F)]. The topographic and phase images reveal that the various solvent treatment processes had quite different effects. In general, the excess PSS domains tended to aggregate, while the PEDOT-PSS domains formed continuous morphologies with the surface phase separation on PEDOT:PSS films.

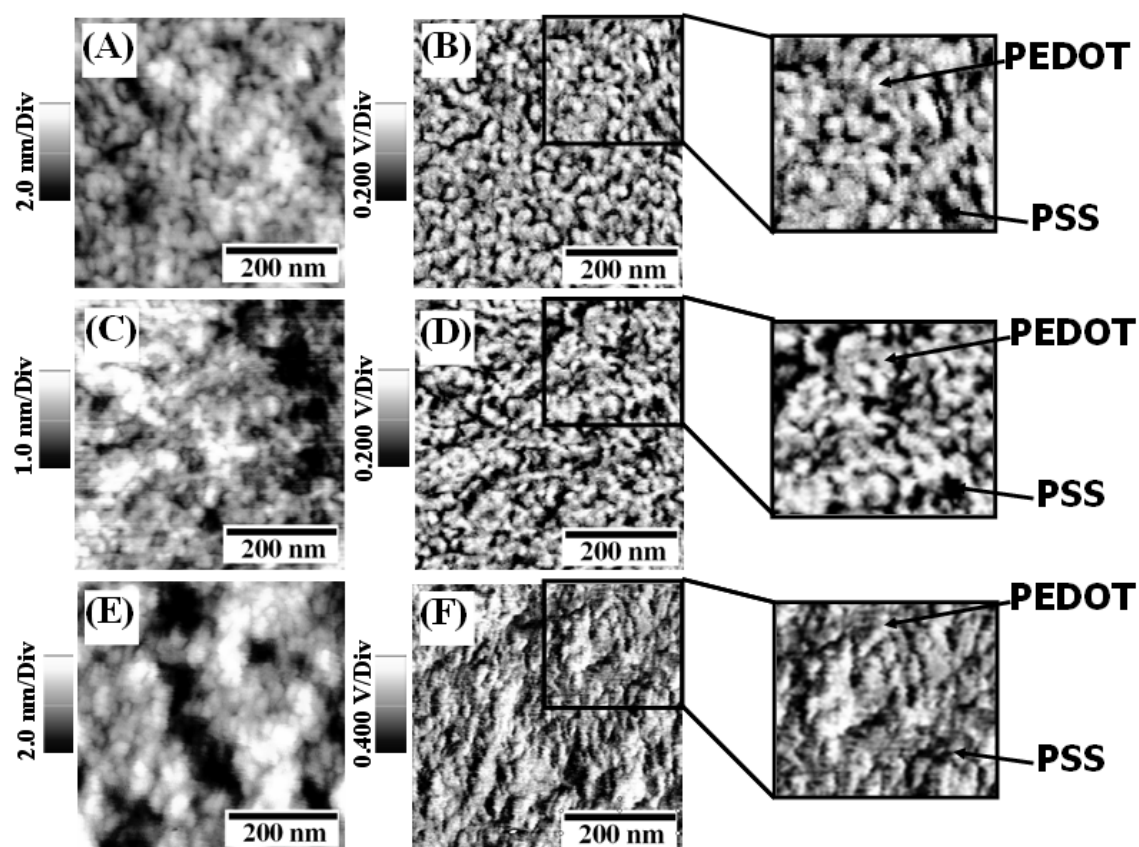


Figure 5.4 Topographic (A, C, E) and phase (B, D, F) images of PEDOT-PSS films (P, P-ME and P-EG, respectively) obtained with tapping-mode AFM.

The ability to observe morphological changes from tapping-mode AFM images is usually not straightforward because the phase image signal is affected by such factors as surface forces, tip indentation, and the bulk properties. [150] To confirm our hypothesis of a correlation existing between the morphology and the conductivity enhancement, we conducted separate TEM experiments using all of the PEDOT:PSS films. The TEM image of the P film [Figure 5.5(A)] reveals that it consisted of well-defined blends of high-conductivity, darker, isolated PEDOT-PSS domains (PEDOT-rich regions, having grain size ca. 50 nm) surrounded by low-conductivity, brighter, excess-PSS domains (PSS-rich regions). In contrast, the TEM images of the P-ET and P-ME films [Figures 5.5(B) and 5.5(C), respectively] reveal indistinct grain boundaries for the conductive PEDOT-PSS domains, having grain sizes ca. 80 and 120 nm, respectively. We suspect that the indistinct grain boundaries and the differing grain sizes caused of the variations in the conductivity enhancements; i.e., the P-ME film possessed larger PEDOT-PSS grain sizes and higher conductivity. The grain boundaries of the PEDOT-PSS domains in the P-EG film are difficult to identify in Figure 5.5(D) and it is due to the swelling degree of PEDOT-PSS domains is more obviously than P-ME film; thus, the conduction paths of PEDOT-PSS were longer, improving the interconnection of high-conductivity domains within the excess-PSS matrix. Now, through spin-coating with various surface-modified compounds on pristine PEDOT:PSS films, the grain size difference of PEDOT-PSS domains from AFM and TEM can be understood. Taking the P film into account, the inner phase separation of PEDOT-PSS domains can be observed with realer grain size ca. 50 nm (from TEM), however, the surface phase separation of PEDOT-PSS domains are having smaller grain size ca. 20–30 nm (from AFM) and that is come from detecting the top side of PEDOT-PSS domains. In the P-ME film, the inner phase separation of PEDOT-PSS domains can be observed with realer grain size ca. 120 nm (from TEM) and the surface phase separation of PEDOT-PSS domains are more continuously with undistinguished

grain size (from AFM).

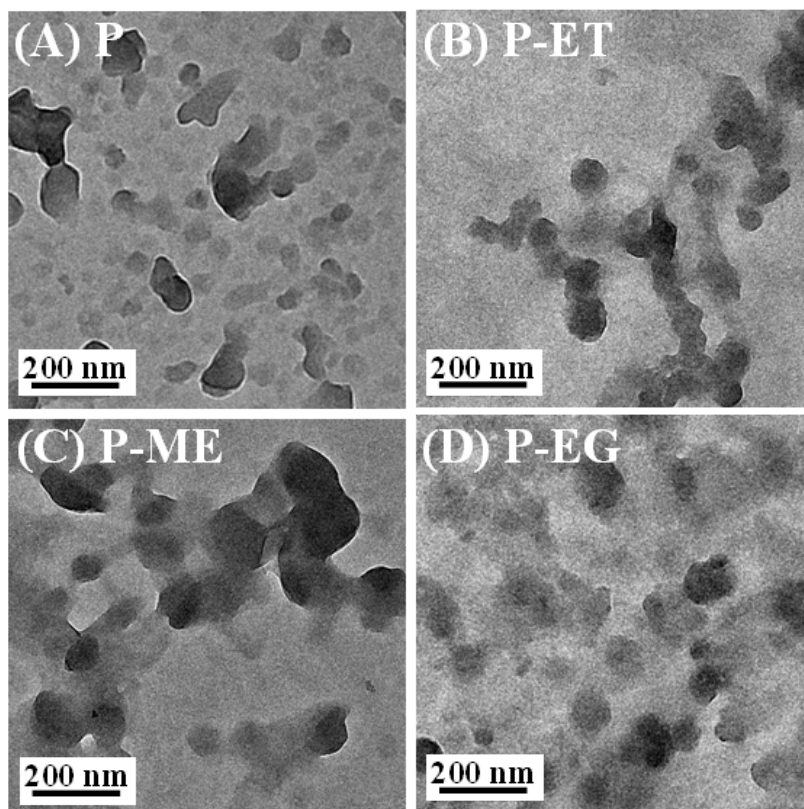


Figure 5.5 TEM images of solvent-modified PEDOT-PSS films. (A) P, (B) P-ET, (C) P-ME, and (D) P-EG.

Although Crispin et al. have used XPS measurements (with grazing emission detected) and AFM to completely investigate the phase separation on the surface of PEDOT:PSS films (with and without 5 wt% diethylene glycol), [150] in order to complement the observed morphological changes of PEDOT:PSS layer through spin-coating selective solvents, we performed XPS measurements (with normal emission detected) of these films to determine the inner compositional changes of the surface. Figures 5.6–5.8 display the C(1s), O(1s), and S(2p) core level XPS spectra, respectively. The C(1s) core level spectra of the P films before and after annealing display the same features: a strong peak at 285.0 eV (from C–C or C=C bonds in PEDOT and PSS chains) and a shoulder at 286.5 eV (from C–O–C bonds in PEDOT). We observed similar features for the P-ME and P-EG films; i.e., the insignificant changes in the C(1s) core level features suggested that no chemical changes had occurred. In contrast, when ET and DME were used to modify the PEDOT:PSS films, weak shoulders appeared at 289 eV, corresponding to C=O bonds [Figures 6(c) and 6(e), respectively]. A previous investigation into the over-oxidation of polythiophene suggested that ET and DME (each possessing one OH group) can induce partial decomposition of thiophene moieties, forming C=O bonds. [155] The O(1s) core level XPS spectra of the PEDOT:PSS films in Figure 5.7 display a shoulder at ca. 533 eV with high binding energy, corresponding to the oxygen atoms of the PEDOT chain, and a strong peak at ca. 531 eV with lower binding energy, arising from the SO₃H and SO₃⁻Na⁺ units of the PSS chains. [156] There were no obvious changes in the chemical environments of the oxygen atoms after heat or solvent treatment. The S(2p) core level spectra of PEDOT:PSS films (Figure 5.8) exhibited no obviously spin-split peaks from the PSS and PEDOT chains—a result that differs from that reported by Jönsson et al. [156] We observe that the PSS chains resulted in a strong peak at ca. 168.5 eV, while the PEDOT chains are represented by a strong peak at ca. 164 eV. To rationalize the surface changes of the PEDOT and PSS components after treatment with

heat and solvent, we used the Shirley method to calculate the peak areas of the S(2p) core level features of the PEDOT and PSS chains. Table 5.2 indicates that the PEDOT-to-PSS ratios of the pristine and annealed films were similar (0.185–0.187). After solvent modification, the PEDOT-to-PSS ratios of the P-ET and P-DME films were 0.276 and 0.217, respectively, implying that the PSS component had moved away from or was slightly washed out of the surface of the PEDOT:PSS films. After ME and EG were employed as coating solvents, the PEDOT-to-PSS ratios increased to 0.308 and 0.420, respectively. This analysis of the S(2p) core levels reveals that a higher solvent polarity resulted in lower amounts of PSS remaining on the surfaces of the PEDOT:PSS films. As a result, the PEDOT:PSS films treated this way had higher conductivity, which correlated to the PEDOT-to-PSS ratio.

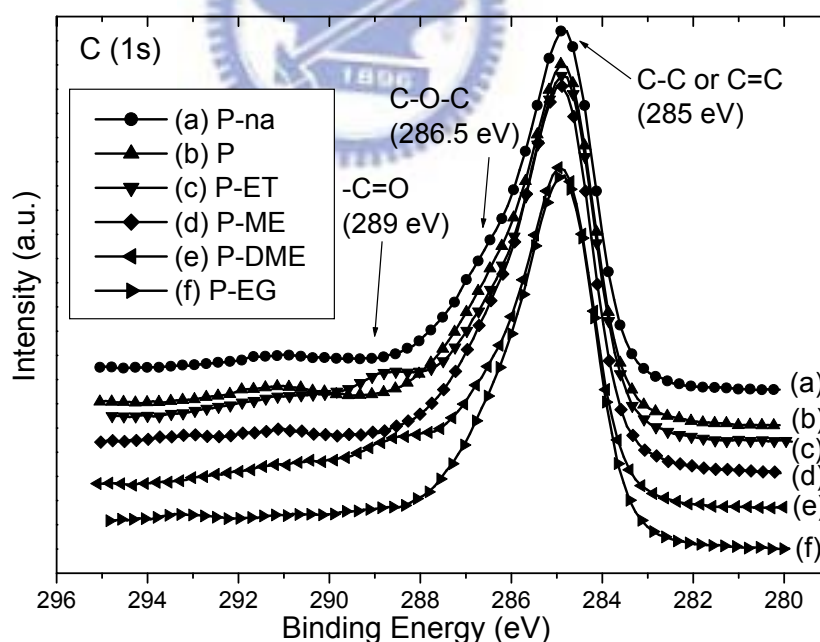


Figure 5.6 C(1s) core level spectra before and after heat treatment of (a) P-na, (b) P, (c) P-ET, (d) P-ME, (e) P-DME, and (f) P-EG.

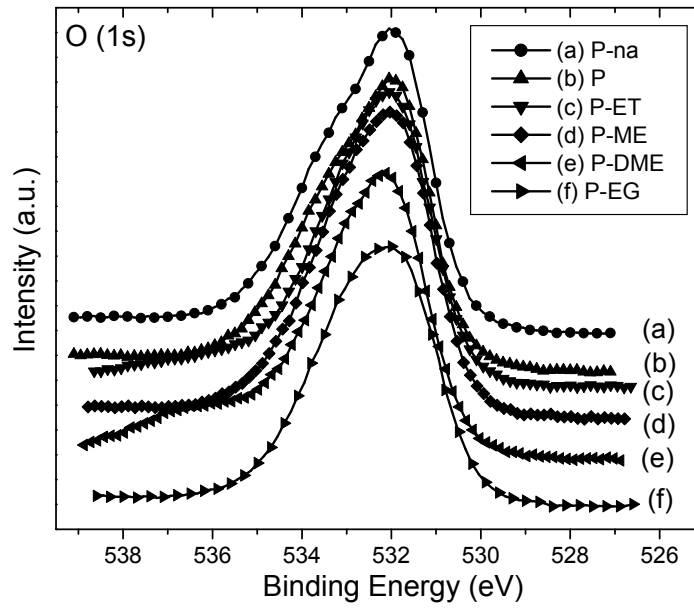


Figure 5.7 O(1s) core level spectra before and after heat treatment of (a) P-na, (b) P, (c) P-ET, (d) P-ME, (e) P-DME, and (f) P-EG.

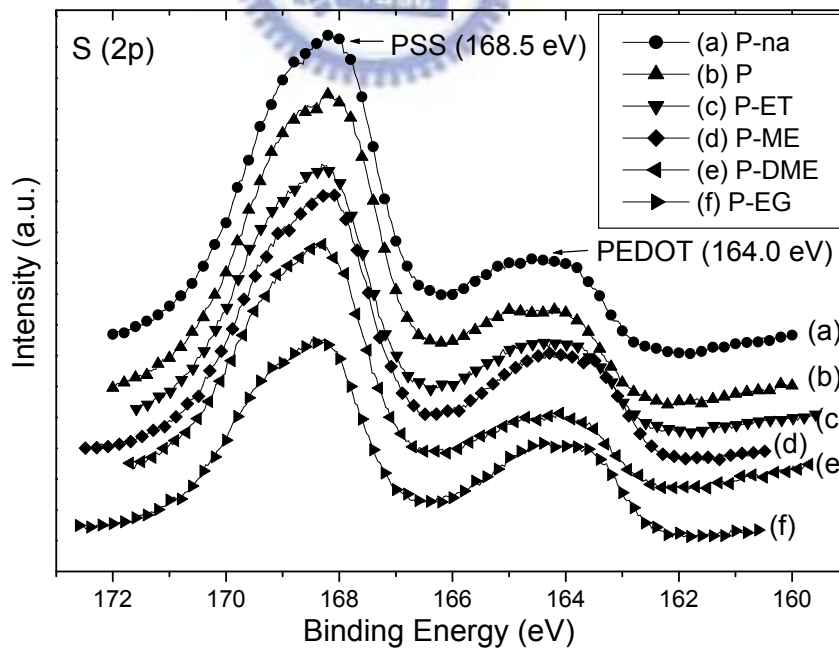


Figure 5.8 S(2p) core level spectra before and after heat treatment of (a) P-na, (b) P, (c) P-ET, (d) P-ME, (e) P-DME, and (f) P-EG.

Table 5.2 Atomic percentages of PEDOT and PSS and PEDOT-to-PSS ratios (from XPS data, calculated using the Shirley method)^{ab}

Anodes	At.% of PEDOT	At.% of PSS	PEDOT-to-PSS ratio
P-na	15.63	84.37	0.185
P-a	15.76	84.24	0.187
P-ET-a	21.66	78.34	0.276
P-ME-a	23.52	76.48	0.308
P-DME-a	17.83	82.17	0.217
P-EG-a	29.60	70.40	0.420

^a na: films with no annealing. ^b a: films with annealing at 150 °C for 1 h.



Timpanaro *et al.* have reported the grain size difference of PEDOT:PSS films through conducting AFM; [157] The separation of pancake-shaped PEDOT-PSS domains by lamellas of PSS have been revealed by Nardes *et al.* revealed through cross-sectional AFM. [158, 159] Comparison with previous reports revealing about schematic morphological models of PEDOT:PSS films, [157-159] the schematic 3D morphological model of high-conductivity PEDOT:PSS films could be concluded from SEM, AFM, TEM and XPS analysis in this study (Figure 5.9). The information of film thickness and morphology were obtained by SEM images; the AFM measurements revealed the surface phase separation of PEDOT-PSS and PSS domains; TEM images gave the perspective drawing of films with grain size and grain boundary changes. By integrating SEM, TEM and XPS results the swelling property and inner phase separation of films were obtained. The washing out of excess PSS from the surfaces of films could be concluded by comparing AFM phase images and XPS results. As shown in Figure 5.9(A)(top-view) and 5.9(B)(side-view), the morphology of P film were proposed. The pancake-shaped smaller PEDOT-PSS domains (upper layer in P film) and larger PEDOT-PSS domains (lower layer in P film) are separated by continuous PSS domains with obviously grain boundary. In P-ME film [Figure 5.9(C) and 5.9(D)], because ME may slightly diffuse into the PEDOT:PSS film and partial swell the upper layer of PEDOT-PSS domains, the PEDOT-PSS domains (upper layer in P-ME film) would rearrange in nanophase with larger grain size and partial indistinctly grain boundary. Moreover, when the thickness of P-EG film [Figure 5.9(E) and 5.9(F)] is ca. 50 nm, the degree of diffusing and swelling effects on P-EG film is apparent that the topography are non-uniform and the PEDOT-PSS domains would form longer conduction paths with indistinctly grain boundary.

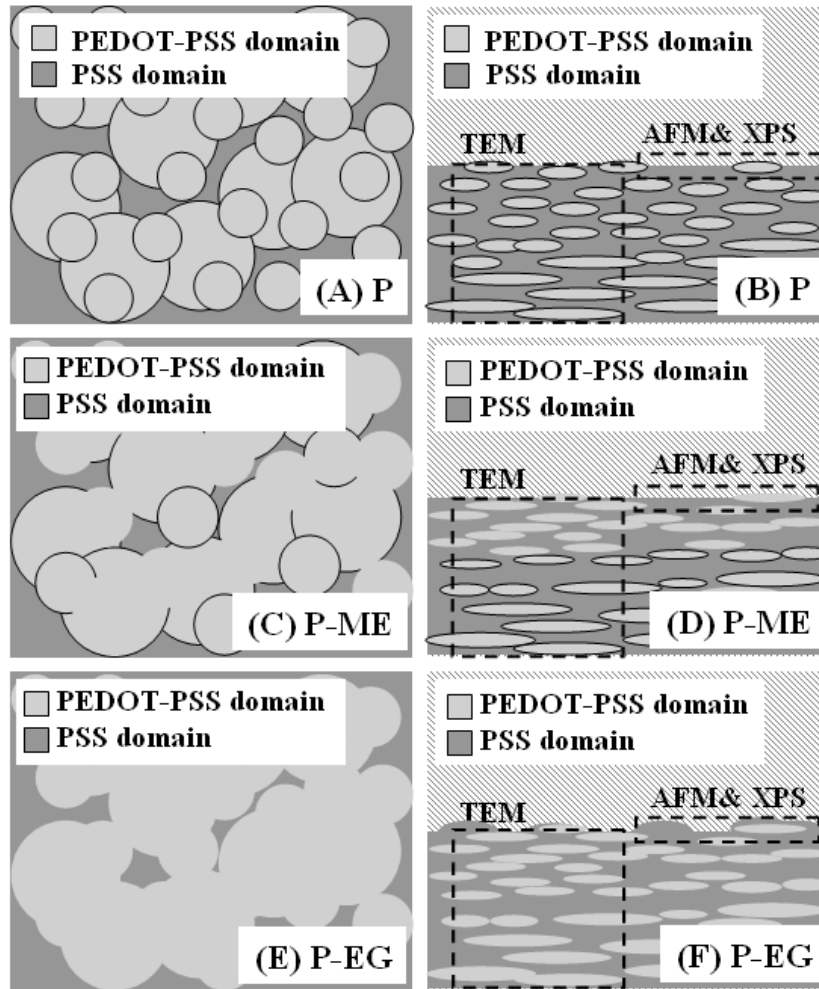


Figure 5.9 Schematic 3D morphological models of (A) P (top-view), (B) P (side-view), (C) P-ME (top-view), (D) P-ME (side-view), (E) P-EG (top-view), (F) P-EG (side-view).

5.3.2 Application of Solvent-modified PEDOT:PSS Film in ITO-free Solar Cells

Table 5.3 and Figure 5.10 summarize the device performances of ITO-free solar cells incorporating the various PEDOT:PSS films. As expected, the high-conductivity PEDOT:PSS films exhibited improved device efficiency. In general, the power conversion efficiencies (PCEs) of the ITO-free photovoltaic devices were strongly related to the sheet resistances of their PEDOT:PSS films. We observed poor current densities, fill factors, and PCEs for the devices prepared using the P, P-ET, and P-DME films as anodes. When ME and EG were used to modify the films, we obtained higher current densities, fill factors, and efficiencies. The PCEs of the P-ME and P-EG devices were 3.13 and 3.39%, respectively, under AM 1.5G (active layer area: 0.01 cm²). Table 5.3 also lists the performance behavior of P-EG and P-ME devices having larger active layer areas (0.02 cm²). The P-ET device having a small active layer area exhibited an AM 1.5G PCE of 1.16%, with an open-circuit voltage (V_{oc}) of 0.58 V, a short-circuit current density (J_{sc}) of 6.74 mA/cm², and a fill factor (FF) of 30%. Poorer performance resulted from using a larger-area active layer, with the values of the FF, J_{sc} , and PCE all decreasing significantly. We observed similar phenomena for the P-ME and P-EG systems: the small and large P-ME devices had PCEs of 3.13 and 2.11%, respectively, while the PCE of the P-EG device decreased from 3.39 to 1.72% upon increasing the area of the active layer. Table 5.3 also lists the output characteristics of the device employing an ITO glass substrate as the anode and a 50-nm-thick P film as a buffer layer. The performance of P3HT was comparable with that reported previously, [121-123] with the optimum efficiency being ca. 3.9%. The devices containing small active areas (0.01 cm²) of P-ME and P-EG exhibited similar performance in terms of their PCEs relative to that of the device based on ITO. In contrast, the performances of large-active-area (0.02 cm²) devices were poor for all of the solvent-modified systems. Even though the electrical conductivity was dramatically

enhanced through ME- and EG-modification, there is obviously a distance effect for PEDOT:PSS based ITO-free PPV devices (Figure 5.1). When using the large-active-area device, the increasing sheet resistance via PEDOT:PSS layer to electrode is observed to decrease J_{sc} .



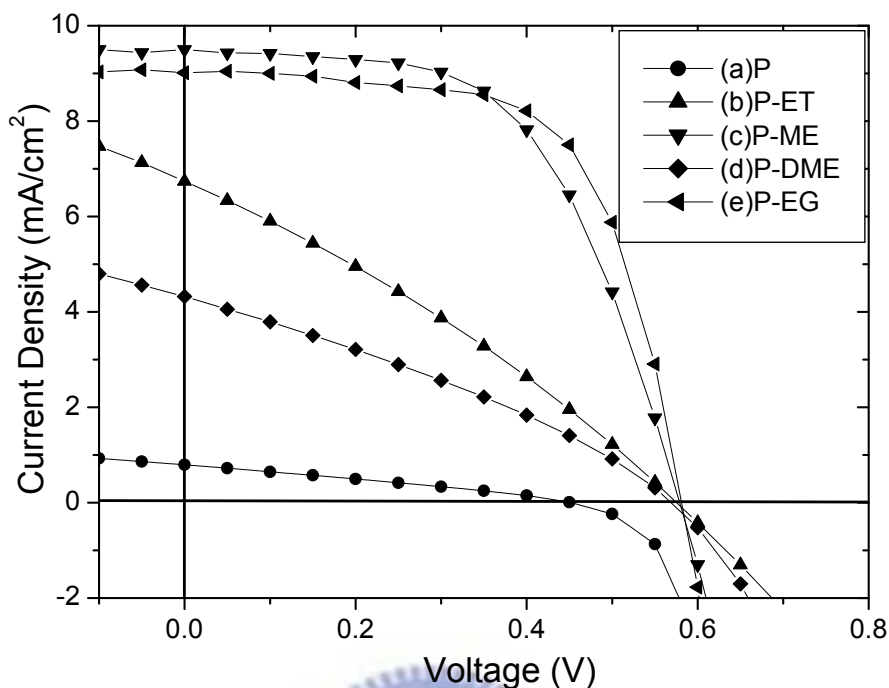


Figure 5.10 Current–voltage characteristics of ITO-free polymer solar cells incorporating the various solvent-modified PEDOT:PSS films: (a) P, (b) P-ET, (c) P-ME, (d) P-DME, and (e) P-EG. All devices were measured under illumination of AM 1.5 (100 mW cm^{-2}) with active area of 0.01 cm^2 .

Table 5.3 Performance of PEDOT:PSS/P3HT:PCBM/Ca/Al photovoltaic devices with various active areas under illumination of AM 1.5 (100 mW cm^{-2})

Anode	$J_{sc}/\text{mA cm}^{-2}$	V_{oc}/V	FF	PCE (%)
P ^a	0.79	0.45	0.29	0.10
P-ET ^a	6.74	0.58	0.30	1.16
P-ET ^b	3.11	0.56	0.30	0.52
P-ME ^a	9.50	0.58	0.57	3.13
P-ME ^b	9.10	0.58	0.40	2.11
P-DME ^a	4.32	0.57	0.32	0.78
P-EG ^a	8.99	0.59	0.64	3.39
P-EG ^b	6.75	0.57	0.45	1.72
P/ITO	10.6	0.62	0.58	3.80

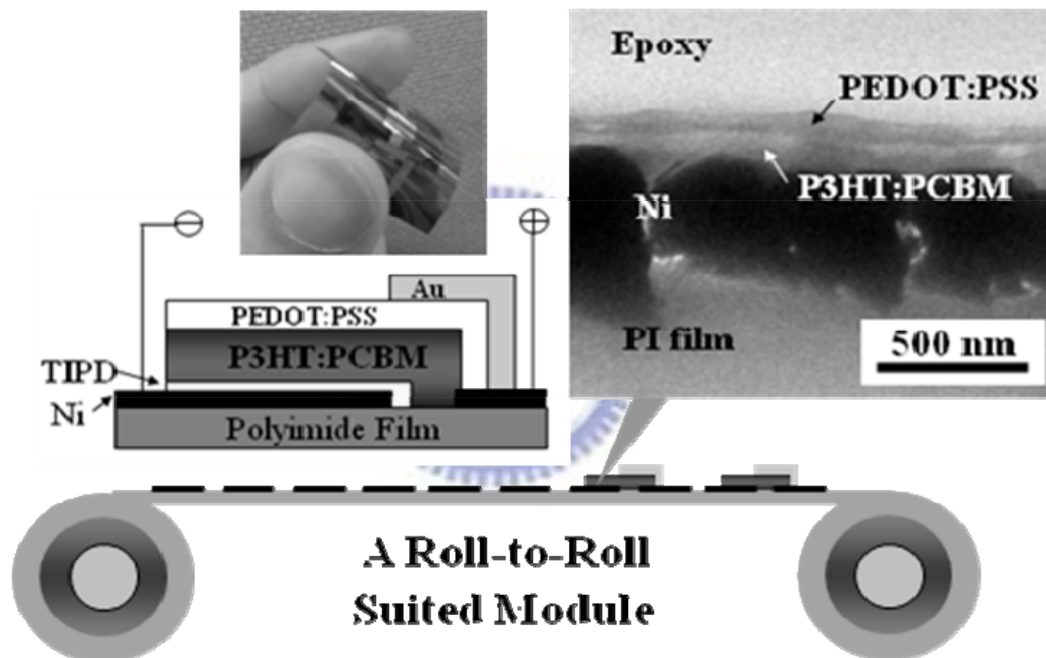
^a Active area of 0.01 cm^2 . ^b Active area of 0.02 cm^2 . P/ITO: P-coated ITO anodes annealed at $150 \text{ }^\circ\text{C}$ for 1 h (active area: 0.04 cm^2).

5.4 Conclusion

We have employed Raman and UV–Vis spectroscopy, SEM, tapping-mode AFM, TEM, and XPS to investigate the origin of the sheet resistance decrease of solvent-modified PEDOT:PSS films. The spin-coating of directly solvent-modified PEDOT:PSS films led to transformation of the chemical structure of PEDOT (from Raman spectroscopic analysis), phase segregation of PEDOT-PSS and PSS domains (from SEM, AFM, TEM and XPS analyses), and washing out excess PSS from the surfaces of the PEDOT:PSS films (from XPS analysis). From a comparison of the variation in conductivity of the modified films, we conclude that phase segregation enabled the formation of longer conduction paths of PEDOT-PSS domains. This phenomenon was the major influence on the conductivity enhancement; the transformation of the PEDOT structure and the decrease in the content of PSS domains on the polymer surface were secondary effects. ITO-free solar cells fabricated using these high-conductivity PEDOT:PSS films as anodes exhibit a high performance. The PCEs of the solar cell devices incorporating ME- and EG-modified PEDOT:PSS films reached 3.13 and 3.39%, respectively, under illumination of AM 1.5 (100 mW cm^{-2}).

Chapter 6

All-Solution-Processed Inverted Polymer Solar Cells on Granular Surface-Nickelized Polyimide



In this study, we prepared all-solution-processed inverted polymer solar cells (PSCs) incorporating two solution-processed electrodes—surface-nickelized polyimide films (NiPI films) as cathodes and high-conductivity poly(3,4-ethylenedioxythiophene)/poly(styrene-sulfonate) (PEDOT:PSS) films as anodes—and an active layer with a bulk heterojunction morphology of poly(3-hexylthiophene) (P3HT) and [6,6]-phenyl-C61-butyric acid methyl ester (PCBM). The granular Ni thin films, which exhibited good adhesion and high conductivity (ca. 2778 S cm^{-1}) on the polyimide (PI) substrates and

possessed a work function different from that of pure Ni metal (WF, 5.4 eV). Using ultraviolet photoelectron spectroscopy, we determined that the WF of the NiPI films was ca. 3.9 eV. Prior to the coating of the photoactive layer, the surface of the NiPI films were treated with titanium(diisopropoxide)bis(2,4-pentanedionate) (TIPD) solution to facilitate the deposition of high-quality active layer and further as a hole blocking layer. The solution processed anodes (solvent-modified PEDOT:PSS films) were further coated and subjected to mild oxygen plasma treatment on the active layer. Short exposure (5 s) to the plasma improved the quality of the surface of the active layer for PEDOT:PSS deposition. These inverted PSCs on flexible granular NiPI films provided a power conversion efficiency of 2.4% when illuminated under AM 1.5 conditions (100 mW cm^{-2}). The phenomenon of light absorption enhancement in those inverted PSCs was observed as indicated in reflective UV-vis, haze factor and external quantum efficiency (EQE) responses. The resulting fill factor (FF) of 0.43 is still significantly lower than the FF of 0.64 for standard devices. When compared to the planar structure, the improvement of absorbance of light and good haze factors was obtained for granular structure which suggests NiPI as a better back contact electrode through enhancing the light trapping and scattering in inverted PSCs.

6.1 Introduction

Polymer solar cells (PSCs) have recently received considerable attention because of their low cost, light weight, high flexibility, and solution-processability. The power conversion efficiency (PCE) of PSCs has been improved to 5% under AM 1.5G conditions [160–163] when using a bulk heterojunction (BHJ) structure comprising a blended film of poly(3-hexylthiophene) (P3HT) as the donor and [6,6]-phenyl-C₆₁-butyric acid methyl ester (PCBM) as the acceptor. In addition to their improved device efficiency [160–164]

and lifetime [165, 166], PSCs possessing inverted structures have also been investigated to further reduce production costs and to facilitate high-throughput production [167–181]. Among inverted PSCs, two major structures are studied most frequently. One employs modified layers located between the active layer and the electrodes to change the energy level of the whole device, i.e., the roles of the indium tin oxide (ITO) material (as the cathode) and the metal electrode (as anode) are different from those of standard PSCs systems [ITO (anode)/PEDOT:PSS/active layer/metal (cathode)] [Figure 6.1(A)]. For this inverted system, in which the roles of the electrodes are exchanged, the use of solution processing methods results in enhanced efficiency from the collocation of appropriate energy levels for the electron- and hole-collection layers [167–173]; in addition, a roll-to-roll suited module would be achieved when introducing an inject-printed metal as the anode [Figure 6.1(B)]. The second type of inverted PSC possessing a layer sequence has great promise for use as a cost-efficient roll-to-roll suited module, i.e., starting with the metallic electron contact on a plastic substrate [175–182]. The active layer is coated on the metal layer, followed by the PEDOT:PSS layer, which forms the transparent hole contact. In this inverted system, the roles of the anode and cathode are similar to those in standard cells, but the processing method employed to build the PSCs is different [Figure 6.1(C)]. Moreover, the preparation of this second type of inverted PSC would presumably provide higher efficiency and lower device fabrication costs when using ITO-free materials. Another advantage when using this inverted PSC system [181, 182] with high topographical variations of metals is that it would lead to an imposed topography on the photovoltaic device; it could also be used to couple light into the film, increasing the optical length in the device. Based on these previous studies, we suspected that combining the technologies for all-solution processing with the high topographical variations of the metal and the high conductivity of PEDOT:PSS would allow us to obtain ITO-free inverted PSCs for high-throughput production on flexible substrates.

Recently, polyimide (PI) films have become generally used components for flexible electronic devices because they exhibit high glass transition temperatures, low surface roughnesses, low coefficients of thermal expansion (CTE), and high chemical resistance under typical fabrication conditions. Surface-metalized PIs have been developed widely using various metals, including Ag, Cu, and Ni [183–186]. In a previous study [185], we developed an all-solution method for fabricating thin granular Ni films on PI (NiPI) with high adhesion and conductivity (ca. 2778 S cm^{-1}). These NiPI films are readily fabricated through alkaline hydrolysis to open the imide rings of the pristine PI film, followed by ion exchange with Ni ions and their subsequent reduction on the PI [Figure 6.2(A)–(E)].

In this paper, we report the fabrication of all-solution-processed inverted PSCs featuring NiPI as the cathode material (back contact electrode) on flexible substrates; these devices have the following configuration: PI/Ni (cathode)/titanium(diisopropoxide)-bis(2,4-pentanedionate(TIPD)/P3HT:PCBM/PEDOT:PSS (anode). From the many reports describing the insertion of a buffer layer between the cathode and the active layer to improve device performances [163, 187–189], we chose the solution-processable TIPD as the buffer layer in this study because Tan et al. demonstrated [189] that the TIPD interface dramatically reduces the degree of interface resistance between the cathode and the active layer. Furthermore, because the energy level of the lowest unoccupied molecular orbital (LUMO) of TIPD is ca. 3.9 eV, we suspected that it would be easy to transport electrons to the NiPI film [work function (WF) = 3.9 eV]. In addition, we developed a low temperature fabrication process ($<150^\circ\text{C}$) to obtain high-conductivity PEDOT:PSS films in these inverted ITO-free PSCs. We readily obtained these high-conductivity PEDOT:PSS films (ca. 283 S cm^{-1}) through spin-coating of a solvent (methoxyethanol, ME) onto pre-coated PEDOT:PSS films [190]; this method appears to be more suitable for plastic substrates because it does not require a very high temperature ($>150^\circ\text{C}$) to remove any polyalcohol [191–196] and, thereby, decreases the likelihood of destroying the active layer. Based on

the previous report, [190] the sheet resistance of PEDOT:PSS electrode (a distance effect for PEDOT:PSS based ITO-free PSC devices) increased as the area of the device increasing, and hence decreased the device performance. The low conductivity of the PEDOT:PSS electrode is actually limited for larger area cells. Therefore, we further deposited a Au grid (thickness at 100 nm) onto the PEDOT:PSS films to efficiently collect holes and efficiently increase the sheet conductivity of the transparent electrode.

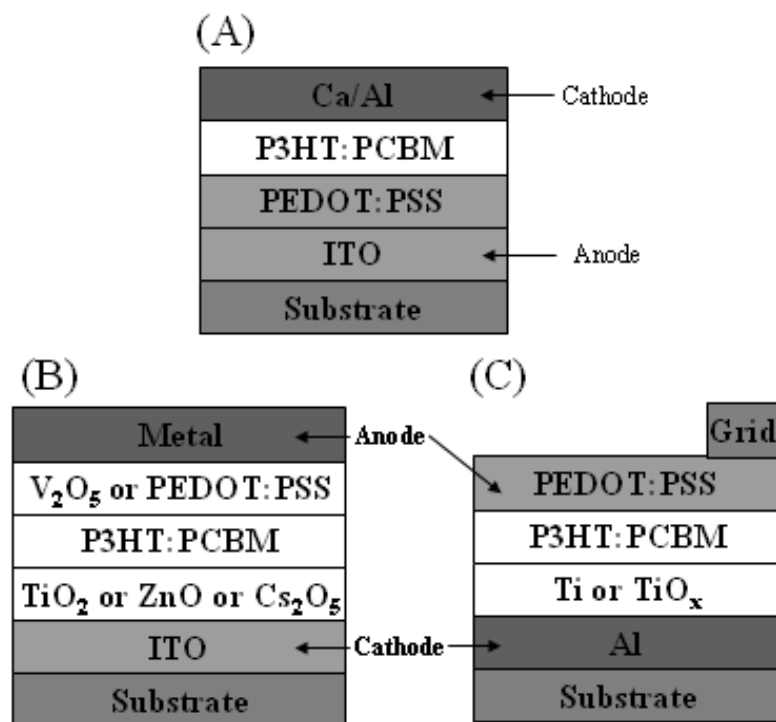


Figure 6.1 Architectures of polymer solar cells: (A) standard, (B) inverted (in terms of the roles of the electrodes), and (C) inverted (in terms of the alternative processing structure).

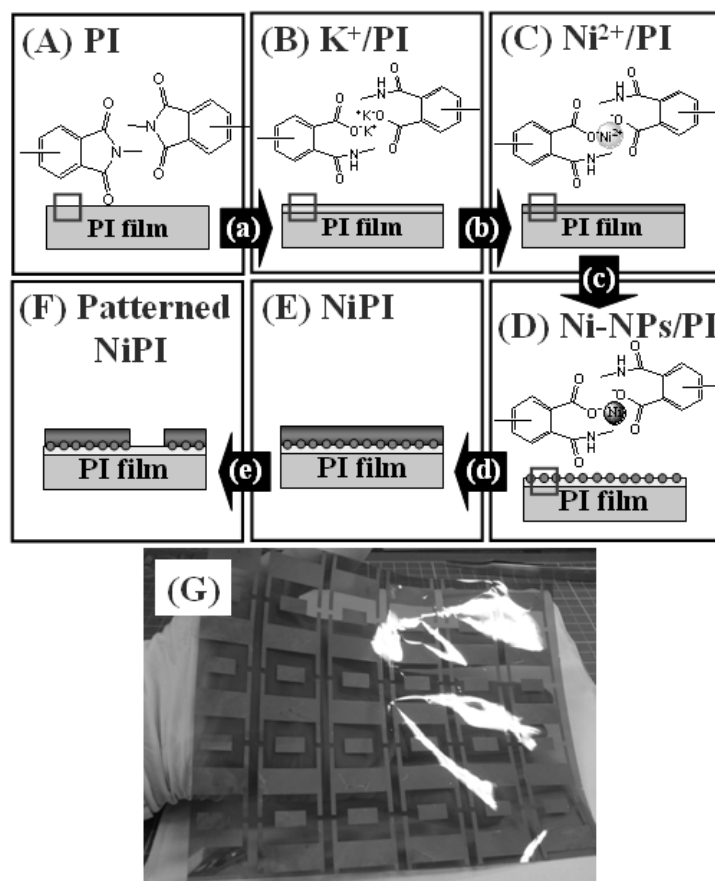


Figure 6.2 Flow chart for the formation of the patterned NiPI film. (A) PI: pristine polyimide; (B) K⁺/PI: K⁺/PAA layer on PI film; (C) Ni²⁺/PI: Ni²⁺/PAA layer on PI film; (D) Ni-NPs/PI: Ni-NPs/PAA layer on PI film; (E) NiPI: Ni/PAA layer on PI film; (F) Patterned NiPI: patterned Ni/PAA layer on PI film; (G) photograph of the patterned NiPI. (a) Alkaline hydrolysis to open imide rings; (b) cation-exchange reaction leading to the incorporation of Ni²⁺ ions; (c) reduction of Ni²⁺ ions by aqueous NaBH₄; (d) Ni electroless plating using an EN solution; (e) patterning of Ni through photolithography.

6.2 Experimental Details

6.2.1 Nickelized Polyimide Films (Cathodes and Substrates)

The process for the direct all-wet-chemical treatment of Ni-coated conductive films was performed according to the procedure outlined in Figures 6.2(A)–(F). The PI films were synthesized from pyromellitic dianhydride (PMDA; from TCI) and 4,4'-diaminodiphenylether (ODA, 98%; from Aldrich); the experimental details for fabricating the PI and nickelized PI films are available elsewhere [185]. Briefly, the PI films were first immersed in 5 M aqueous KOH at 25 °C for 7 min and then rinsed with deionized water. Next, the K⁺ counterions associated with the opened imide rings on the surface of the PI films were exchanged with Ni²⁺ ions through immersion in 50 mM aqueous nickel sulfate at 25 °C for 5 min, followed by rinsing with deionized water. The surface Ni²⁺ ions were then reduced in aqueous NaBH₄ (0.2 g/100 mL deionized water) at 25 °C for 5 min to form Ni nanoparticles on the PI surface (Ni-NPs/PI films), which were then rinsed with deionized water. The Ni NP-seeded PI films were immersed in an electroless nickel bath (EN solution) at 50 °C for 8 min to form thin Ni layers on the PI films (NiPI). The EN solution was prepared from a 4:1 (v/v) mixture of a Ni stock solution [nickel sulfate (40 g L⁻¹), sodium citrate (20 g L⁻¹), and lactic acid (10 g L⁻¹) in deionized water) and a DMAB solution (1 g L⁻¹ in deionized water). A cartoon representation and a photograph of the patterned NiPI are presented in Figure 6.2(F) and 6.2(G), respectively. The NiPI films have long-term air stability in the atmosphere. Prior to the deposition of the photoactive layer, the NiPI films were cleaned with organic solvents.

6.2.2 Active-Layer Materials

Because of the large differences in the values of the contact angles and surface energies of Ni and PI surfaces (Table 6.1), the solution-processable titanium chelate TIPD

(from Aldrich) was pre-coated as the cathode buffer layer on the patterned NiPI film surfaces to facilitate the fabrication of high-quality active layers. Next, a blend [1:0.8 (w/w), 17 mg mL⁻¹ in dichlorobenzene (DCB)] of P3HT (Rieke Met. Inc.) and PCBM was stirred overnight in DCB, filtered through a 0.2- μ m poly(tetrafluoroethylene) (PTFE) filter, and then spin-coated (500 rpm, 60 s) on top of the NiPI films.

Table 6.1 Contact angles and surface energies obtained after performing the inverted fabrication process.

Sample	H ₂ O	C ₂ H ₄ I ₂	Surface energy (mJ m ⁻²)
PI	75.5	41.1	39.1
NiPI	104.9	38.0	58.4
TNiPI	87.0	33.6	46.6
PTNiPI	108.2	60.6	37.0
PTNiPI ^a	55.8	32.7	47.4
HCV4	48.0	29.5	52.1

PI: Pristine polyimide film.

NiPI: Ni/PI film obtained after annealing at 150 °C for 30 min.

TNiPI: Sample obtained after depositing TIPD solution on the NiPI and then annealing at 70 °C for 5 min.

PTNiPI: Sample obtained after depositing the P3HT:PCBM film on the TNiPI and then annealing at 140 °C for 15 min.

HCV4: Sample obtained after depositing the PEDOT:PSS film on the glass substrate and then annealing at 100 °C for 5 min.

a: After mild oxygen plasma treatment for 5 s.

6.2.3 High-Conductivity PEDOT:PSS Films (Anodes)

The high-conductivity PEDOT:PSS anodes were prepared using a two-step method [190]. In the first step, a 95:5 (w/w) mixture of PEDOT:PSS solution (HC V4; from H. C. Starck) and dimethyl sulfoxide (DMSO; from Aldrich) was filtered through a 0.45- μ m

filter prior and then deposited (spin-coating at 4000 rpm in the air) onto the active layers with a mild oxygen plasma exposure for 5 s (plasma cleaner PDC-32G, Harrick Scientific, Ossining, NY) at a thickness ca. 50 nm. In the second step, the surface-modifying solvent, ME, was spin-coated onto the pristine PEDOT:PSS films at 3000 rpm, which were then dried at 100 °C for 5 min inside a glove box. The device was completed by coating a 100-nm-thick layer of Au as a metal grid and a mask to improve hole collection and define the active area, respectively. The cell was then encapsulated using a UV-curing glue (Nagase, Japan). The active area of each photovoltaic (PV) cell was 0.036 cm². Figure 6.4(A) displays the architecture of the inverted ITO-free polymer/fullerene solar cells.

6.2.4 Instrumentation

The NiPI films were transferred within 3 min of their formation into the sample-loading chamber of an ultraviolet photoelectron spectroscopy (UPS) system. UPS (VG ESCALab 250, HeI $h\nu = 21.2$ eV) spectra were recorded at a sample bias of -5.0 V to observe the secondary electron cutoff, from which the work function could be derived from the width of the Fermi edge of a Au substrate. XPS spectra were recorded using a VG Scientific Microlab 350 spectrometer operated in the constant analyzer energy mode with a pass energy of 50 eV and MgK α (1253.6 eV) radiation as the excitation source (with normal emission detected). The sheet resistances of the PEDOT:PSS films were measured using a four-point probe; the average of the measured values is reported. The transmittance spectra were recorded using an HP8453 UV–Vis spectrometer. Contact angles and surface energies were measured and calculated using the geometric mean approximation (GMA) and a FTA-200 dynamic contact analyzer operated with H₂O and CH₂I₂ as the two standard liquids. The crystalline phase of samples was characterized using a BEDE D1 grazing incidence X-ray diffractometer (GIXRD) and Cu K α radiation. The incident angle

of the X-ray beam was fixed at 0.5° . The surface morphologies and phase changes of the PEDOT:PSS films were analyzed using a VEECO DICP-II atomic force microscope (AFM) operated in the tapping mode (Si tips on Si cantilevers having a spring constant of 2 N m^{-1} and a set point of ca. 0.8–0.9) in the air. A JEOL JSM-6500F scanning electron microscope (SEM) was employed to investigate the thicknesses of the PEDOT:PSS films. Samples for transmission electron microscopy (TEM) analysis were prepared through microtoming with a Leica Ultracut Uct apparatus into 90-nm-thick slices that were placed onto a 200-mesh carbon-coated Cu TEM grid (Agar Sci., Inc.). TEM images were recorded using a JEOL-2010 transmission electron microscope and an internal charge-coupled device (CCD) camera. Current–voltage (I – V) curves of the PSC devices were measured using a computer-controlled Keithley 2400 source measurement unit (SMU) equipped with a Peccell solar simulator under AM 1.5 illumination (100 mW cm^{-2}). The spectral irradiance data of the light source was similar to the AM 1.5G solar spectrum (spectral mismatch $<5\%$ in the range 350–800 nm). The illumination intensity was calibrated using a standard Si photodiode detector equipped with a KG-5 filter. All of these measurements were performed under an ambient atmosphere at room temperature. All of these inverted PSCs are identified by "PTXNiPI-X", the first number denoting to the incorporating different concentrations of TIPD (wt%), the follow number denoting to the thermal annealing time (min). The absorption spectra were recorded using a Hitachi U-4100 UV–Vis spectrometer with the integrating sphere. The planar and granular substrates were characterized by Optical Spectrometry (MFS-530 commercialized by Hong-Ming Technology): the total and scattered reflectivity have been measured and the Haze factors ($H_R(\lambda)$) have been calculated for each of the substrates according to the equation, $H_R(\lambda) = R_{\text{scat}}(\lambda) / R_{\text{tot}}(\lambda)$, and these optical measurements have been performed in air.

6.3 Results and Discussion

To examine the feasibility of using NiPI as the cathode (back contact electrode), we used UPS to determine that the WF of the surface-nickelized PI (NiPI) was 3.9 eV, i.e., it differs from that of pure Ni [Figure 6.3(A)] [197]. Because this value is lower than that of the Al cathode (ca. 4.2 eV), it appeared suitable for application as the back contact electrode in inverted PSCs. To understand why there was a difference in the WFs of NiPI and pure Ni, we performed an XPS survey and then obtained the Ni/B ratio of NiPI (ca. 2.9) by using the Shirley method to estimate the peak areas of the atom contents on the NiPI surface in Figure 6.3(B). According to previous reports [185, 186] and the results of this XPS analysis, in addition to a small amount of oxygen (representing native oxides or B₂O₃) formed on the NiPI surface, we suspect that the Ni-B component, which arose from the use of dimethylamine borane (DMAB) as the reductant in the Ni electroless deposition process, was responsible for the WF of the NiPI film to differ from that of pure Ni. The SEM image in Figure 6.3(C) reveals that the granular NiPI consisted of fine particles (ca. 200–300 nm) with a continuous and interconnected network. Figure 6.3(D) provides a schematic energy level diagram. The WF of NiPI allows efficient electron transfer from the LUMO of PCBM. Based on the previously report, [189] the TIPD layer could improve the electron collection and reduce the interface resistance between the active layer and the metal cathode. From the view of energy level, the WF of TIPD matches the transport levels of the respective charge carriers for efficient charge transferring, however, other effects like oxide layers, dipole layers or the interface morphology of the photoactive layer might affect the charge injection. Table 6.1 summarizes the contact angle (CA) and surface energy (SE) data. On the surface of patterned NiPI, the difference in the H₂O contact angles of PI (CA = 75.5°) and Ni (CA = 104.9°) was dramatic. We attempted to improve the device performance through solvent annealing (slow drying) with DCB, a solvent with

a high boiling point, to enhance the degree of microcrystalline lamellar stacking in the solid state packing of the active layer [198]. We found, however, that the slow drying process had a negative effect on the quality of the P3HT:PCBM film when using the patterned NiPI as the substrate. After spin-coating the P3HT:PCBM solution onto the patterned NiPI film, droplets of P3HT:PCBM tended to aggregate on the Ni surface through slow growth and the thickness of the active layer became non-uniform. To overcome this problem, we precoated the TIPD onto the NiPI surface. The TIPD-modified, patterned NiPI film, which we refer to as TNiPI, had a contact angle of 87.0° ; therefore, droplets of the P3HT:PCBM solution covered the TNiPI surface more completely, resulting in uniform P3HT:PCBM films that we name PTNiPI.

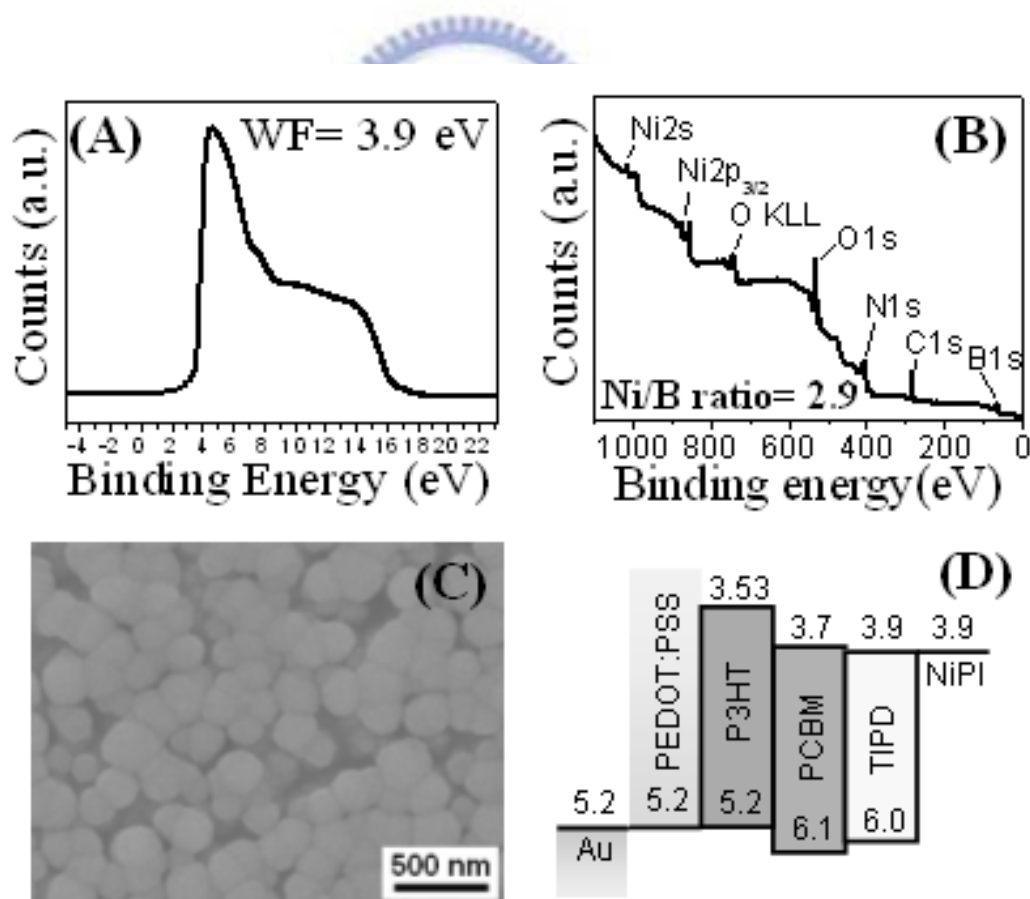


Figure 6.3 (A) Photoelectron spectrum of NiPI film. (B) XPS spectrum of NiPI surface. (C) SEM image of NiPI surface. (D) Schematic representation of the energy levels of an ITO-free inverted PSC on PI.

Because of the large variation in the values of CA of P3HT:PCBM and PEDOT:PSS (Table 6.1), the deposition of PEDOT:PSS on the highly hydrophobic P3HT:PCBM surface requires a preliminary treatment process to ensure wettability and adhesion. Chaudhary et al. [199] demonstrated that short exposure (5 s) to Ar plasma can effectively tailor the wettability of P3HT:PCBM layers for subsequent deposition of single-wall carbon nanotubes (SWNT) from an aqueous solution. In our present study, oxygen plasma treatment was more convenient than Ar plasma treatment; therefore, we subjected our PTNiPI film to a short (5 s exposure) oxygen plasma treatment to facilitate the deposition of PEDOT:PSS on the active layer. The oxygen plasma-treated PTNiPI film exhibited values of CA and SE of ca. 55.8° and 47.4 mJ m^{-2} , respectively, similar to those of the PEDOT:PSS film. To determine the influence of the 5-s oxygen plasma treatment on the surface of the active layer, we analyzed the performance of standard PSC structures (glass/ITO/PEDOT:PSS/P3HT:PCBM/Ca/Al) formed with and without plasma treatment. The variation in the PCE was less than ca. 0.1%, arising mostly from a slight loss in the current density; the values of V_{oc} and the fill factor (FF) were unaffected, as revealed by the $I-V$ characteristics (Table 6.3). The treatment of oxygen plasma might predominately destroy the P3HT phase, but not the PCBM phase. As the consequence, the electron injection interface might still be working for standard cell. However, this may significant effect the anode interface. To investigate if and how the effect through oxygen plasma treatment, we employed XPS measurements to quantitative determine the thiophene defects through oxygen plasma treatment [Figure 6.4(A)]. The S(2p) core level spectra showed that there were 96% thiophene (at 164 eV) preserved and only 4% thiophene defects (at 168.5 eV) were observed through 5-s oxygen plasma treatment on the active layer surface. In the inverted geometry, this would lead to a destruction of the anode interface; however the effect is not significant as a result of XPS spectra.

To apply PSCs in an economical roll-to-roll-suited module, the major requirement to

reduce the cost of production is substitution of a cheap material in place of the ITO electrode. In a previous report [177], Zimmermann et al. constructed an ITO-free PSC module that comprised PSCs on metal-coated plastic substrates with an inverted layer sequence. Based on their module concept, we examined the solution processing of NiPI, our surface-nickelized PI film, as the cathode/substrate and the high-conductivity PEDOT:PSS as the anode for the all-solution processing of PSCs [Figure 6.4(B)]. Figure 6.4(B)-(D) present the structure, optical and TEM images of the inverted PSC cell on NiPI. Although the TIPD layer was too thin to identify, the cross-sectional TEM image of the device clearly indicates the presence of individual layers without interlayer mixing [Figure 6.4(D)]. The PSCs had the following device structure: PI/Ni ($385 \text{ nm} \pm 77 \text{ nm}$)/TIPD/P3HT:PCBM (100 nm)/PEDOT:PSS (45 nm).



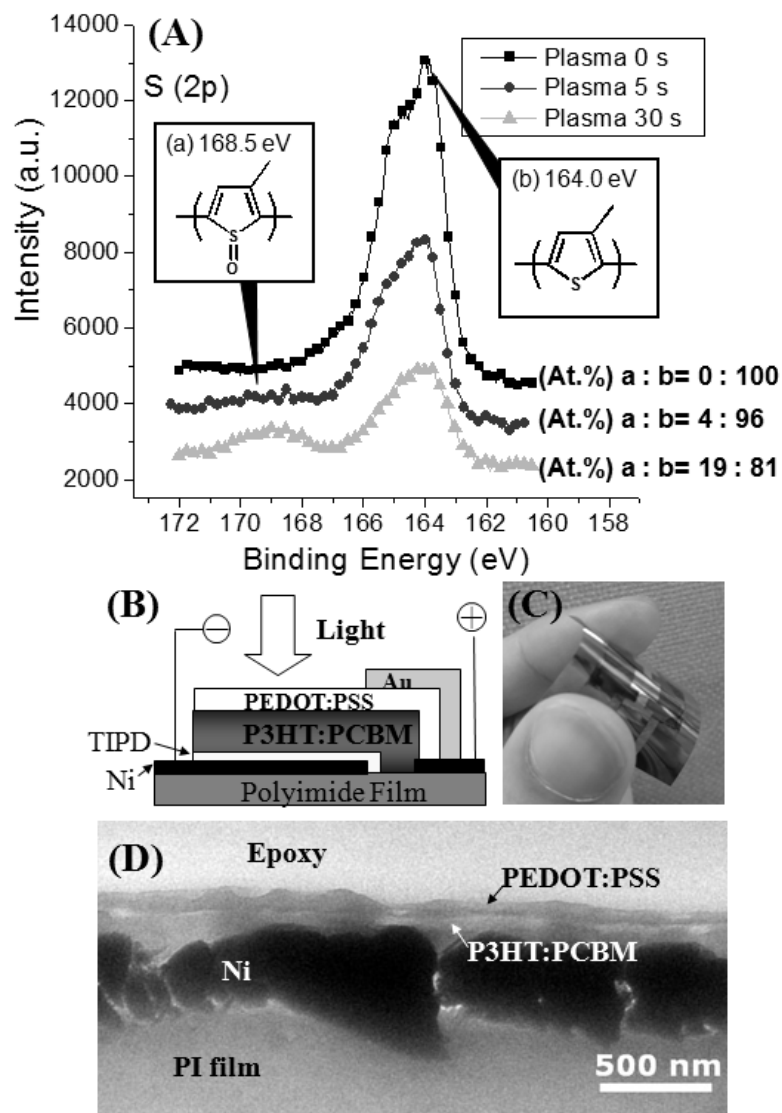


Figure 6.4 (A) $S(2p)$ core level spectra of P3HT:PCBM film (1:0.8 w/w) with plasma treatment for various seconds. (B) Architecture of an inverted PSC featuring an inverted sequence on NiPI as the back contact electrode. (C) Optical image of an inverted PSC on NiPI. (D) TEM cross-sectional image of an inverted PSC on NiPI. Scale bars, 500 nm.

The conductivity of NiPI and ITO were 2778 and 7143 S cm⁻¹, respectively (Table 6.2). The resistive loss of NiPI could be ignored for small cell device. Nonetheless, NiPI layer is actually limited for larger area cells similar to the ITO based devices. To form a transparent conducting anode, we employed the low-temperature processing of high-conductivity PEDOT:PSS. When processing with a polyalcohol, the conductivity of PEDOT:PSS films can be enhanced for their application in PSCs. Although adding a polyalcohol would obviously decrease the sheet resistance of the PEDOT:PSS films, higher processing temperatures (>140 °C) and longer thermal treatment times are necessary to remove the high-boiling-point (>200 °C) additive [191–196], which may damage the P3HT/PCBM blends in our inverted structure. Herein, we selected DMSO and ME as solvents to investigate their ability to enhance the conductivity of PEDOT:PSS at low processing temperatures. The pristine PEDOT:PSS film (**H**; HC V4 from H. C. Starck) had the lowest conductivity (5 S cm⁻¹). When we added 5 wt% DMSO into this pristine PEDOT:PSS aqueous solution, the conductivity of the **HD** film was enhanced to 170 S cm⁻¹. Furthermore, consistent with our results from a previous study [190], surface solvent-treatment of **HD** films with ME (**HDM**) led to a dramatic increase in the conductivity of the PEDOT:PSS to 283 S cm⁻¹ and a corresponding processing temperature lower than that required for the polyalcohol system.

If transparent electrodes are to be used in PV devices, they must have high transparency in the visible region. Thicker PEDOT:PSS films will lead to transmittance and vertical conductivity problems. We observed that the transmittances of the thin PEDOT:PSS films (<100 nm) of **H**, **HD**, and **HDM** on glass (each ca. 96%) were better than that of **ITO** (ca. 89.6%; Table 6.2). From a comparison of the electrical conductivities of **ITO** (same as the anode of a standard cell), and **NiPI**, we observed that the highest conductivity of PEDOT:PSS (**HDM**) was enhanced to 283 S cm⁻¹ with a order less than **ITO** and **NiPI**. We suspect that combining a suitable metal grid (such as a metal grating or

random metal nanowire mesh) with **HDM** film may be compatible with the future development of flexible PSCs [200, 201].

Table 6.2 Sheet resistances and conductivities of PEDOT:PSS, ITO, and NiPI films.

Sample	Film thickness (nm)	Transmittance at 550 nm (%)	Sheet resistance ^c (k Ω sq ⁻¹)	Conductivity ^c (S cm ⁻¹)
H	90 ^a	96.7	22.00	5
HD	45 ^a	96.9	1.310	170
HDM	45 ^a	96.4	0.785	283
ITO	200 ^a	89.6	0.007	7143
NiPI	300 ^b	–	0.012	2778

H: Thin film of PEDOT:PSS (HCV4) on the glass substrate.

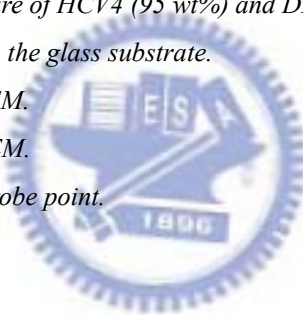
HD: Thin film obtained from a mixture of HCV4 (95 wt%) and DMSO (5 wt%) on the glass substrate.

HDM: ME-modified HD thin film on the glass substrate.

a: Film thickness identified using SEM.

b: Film thickness identified using TEM.

c: Values determined using a four-probe point.



Because TIPD was present as an ultrathin layer on NiPI [Figure 6.4(D)], it was necessary for us to determine the thickness of P3HT:PCBM on the highly topographically variant NiPI to obtain the optimized parameters for these inverted PSCs, because the effect of a thinner active layer (higher speed of coating of the P3HT:PCBM solution) on the imposed topography of the anode would increase the risk of creating short circuits (i.e., lower the efficiency of the device) [181]. If the P3HT:PCBM solution was spin-coated on TNiPI for 700 rpm, the thinner active layer film on the imposed topography of anode would increase the risk of creating short circuits to lower the efficiency of the device. As the result of the device performance and the TEM cross-sectional image, the minimum active layer film thickness was suggested to be ca. 200 nm. Thus, under the optimal conditions for spin-coating of the P3HT:PCBM solution onto TNiPI (500 rpm), we investigated the concentrations with respect to the thickness of the TIPD layer of the whole devices. Prior to the coating of the photoactive layer, the TIPD layers were treated at the temperature of 80 °C and 160 °C for 5-30 min to investigate the temperature effect of the TIPD film without a superimposed effect of the active layer. Similar cell performances were obtained as the temperature and annealing condition change. First, to understand the thermal stability of the TIPD-coated devices, we examined the device performances after employing various thermal annealing times. Table 6.3 summarizes the device performance under AM 1.5 illumination at an intensity of 100 mW cm⁻². The device formed using an interfacial layer of 3.75 wt% TIPD (**PT3NiPI-5**) and a short thermal annealing time (5 min; 140 °C), exhibited poor performance: $V_{oc} = 0.54$ V; $J_{sc} = 9.0$ mA cm⁻², FF = 0.29; PCE = 1.4%. After increasing the thermal annealing time at 140 °C to 15 min, the values of V_{oc} , J_{sc} , and FF all increased, thereby improving the value of PCE to 2.4%. When TIPD was incorporated at 1.88 wt% (**PT1NiPI-15**), we obtained similar results, i.e., improved performance after longer periods of thermal treatment; after thermal annealing for 15 min, the values of V_{oc} , J_{sc} , FF, and PCE were 0.59 V, 9.2 mA cm⁻²,

0.37, and 2.0%, respectively. Consistent with previous results, this TIPD-coated NiPI was stable to thermal annealing at 140 °C for several minutes. We suspect that this TIPD-coated NiPI would be more suitable than the corresponding ITO/PET system [202, 203] for long-time high-temperature annealing.

To compare the performance of devices incorporating different concentrations of TIPD (0.94, 1.88, 3.75, 7.5, and 15 wt%), we performed AFM measurements to determine the underlying mechanism of TIPD incorporation on NiPI. We observed interesting morphologies with high topographical variations for the pristine NiPI and TIPD-coated NiPI surfaces (Figure 6.5). After coating with TIPD at 0.94, 3.75, and 15 wt%, the root-mean-square roughness (Rms) changed from 33.8 nm for pristine NiPI to 24.6, 24.3, and 25.3 nm, respectively. Thus, coating with different TIPD concentrations did not have a significant effect on the value of the Rms. Furthermore, in the phase image of NiPI, the topographical variations of granular Ni films were expressed as a darker edge effect [Figure 6.5(b)]. After coating TIPD onto NiPI, we expected the phase changes to be more obvious at the darker edges of the granular NiPI. The previous study have been reported [176] that charge collection could be enhanced by using a thin layer of Ti/TiO_x on top of the Al electrode; in the absence of this Ti compound coating, the oxide formed on Al blocked charge transport. For our TIPD systems, even a small amount of oxygen (representing native oxides or B₂O₃) formed on the NiPI surface [Figure 6.3(B)], we suspected that a higher concentration of the coating TIPD solution (3.75 wt%) would be more effective at enabling charge collection in the inverted cells than would a coating of 0.94 wt%. From an analysis of the PSCs' performances, we found that higher concentrations of TIPD led to improved PCE, presumably because a more uniform TIPD layer on NiPI enhanced electron transport to the anode [Figure 6.5(c)–(f)]. Increasing the concentration of TIPD from 3.75 to 15 wt% decreased the current density, which led to poorer performance. Based on the similar values of V_{oc} of the **PT3NiPI-15**, **PT7NiPI-15**,

and **PT15NiPI-15** devices (Table 6.3 and Figure 6.6), it appears that exceeding the critical concentration of TIPD (3.75 wt%) led to a lower variation of the angles in the phase images [cf. Figure 6.5(g) and (h)], which would block the degree of electron transport to NiPI and, thereby, decrease the current density.

Table 6.3 Performance of PSCs under AM 1.5 illumination (100 mW cm^{-2}).

Sample	Structure	J_{sc} (mA cm^{-2})	V_{oc} (V)	FF	PCE (%)
Standard ^a	Standard	9.2	0.64	0.63	3.7
Standard-p ^a	Standard	8.8	0.63	0.64	3.6
PT1NiPI-5^b	Inverted	8.3	0.58	0.26	1.2
PT3NiPI-5^b	Inverted	9.0	0.54	0.29	1.4
PT0NiPI-15^b	Inverted	5.4	0.43	0.25	0.6
PT1NiPI-15^b	Inverted	9.2	0.59	0.37	2.0
PT3NiPI-15^b	Inverted	9.3	0.60	0.43	2.4
PT7NiPI-15^b	Inverted	5.2	0.61	0.35	1.1
PT15NiPI-15^b	Inverted	4.4	0.59	0.24	0.6

Standard: Standard PSC structure without plasma treatment.

Standard-p: Standard PSC structure with plasma treatment on the active layer.

a: Active area = 0.04 cm^2 .

b: Active area = 0.036 cm^2 .

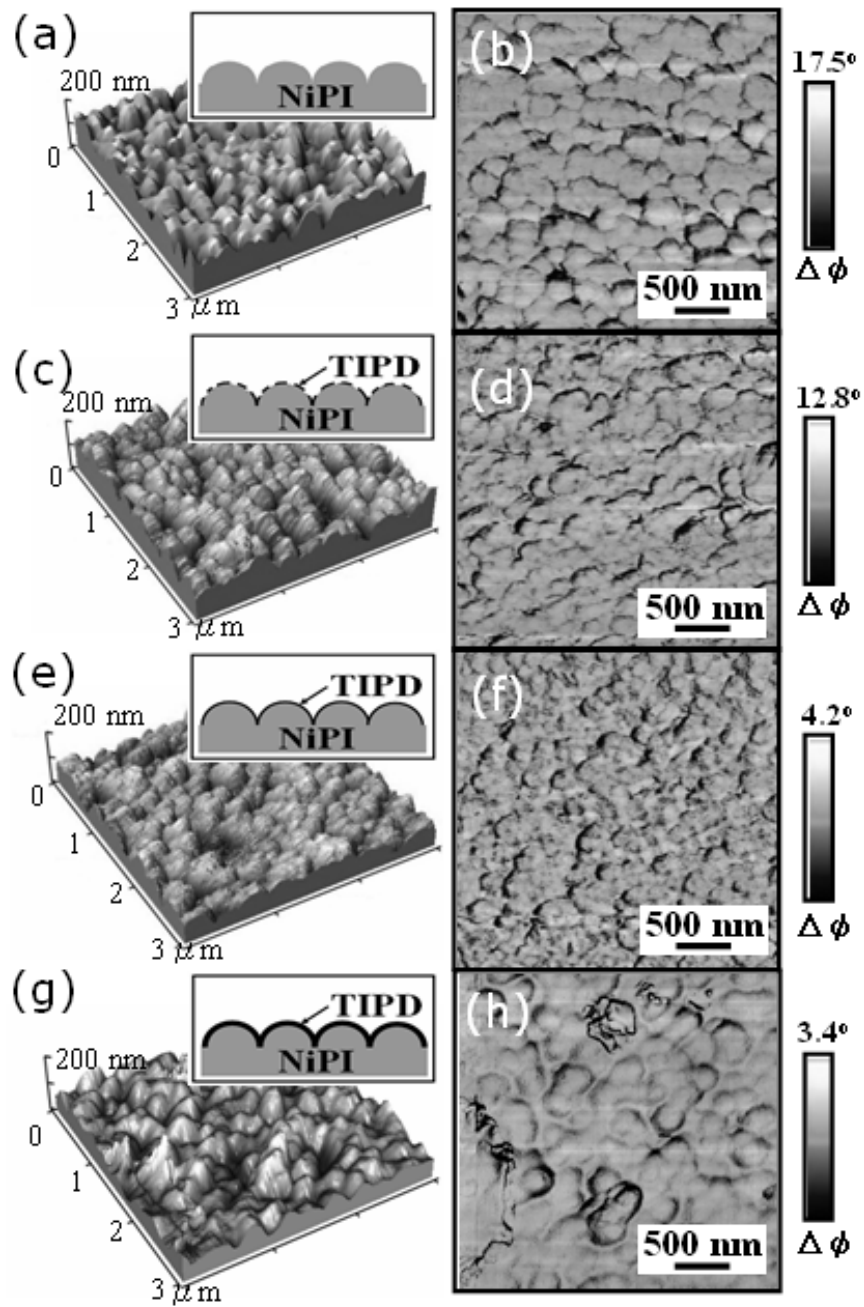


Figure 6.5 (a, c, e, g) Topographies (including cartoon representations) and (b, d, f, h) phase images of NiPI and TIPD-modified NiPI films. (a, b) NiPI: pristine NiPI film; (c, d) T0NiPI: TIPD (0.94 wt%) on NiPI film; (e, f) T3NiPI: TIPD (3.75 wt%) on NiPI film; (g, h) T15NiPI: TIPD (15 wt%) on NiPI film. Scale bars, 500 nm.

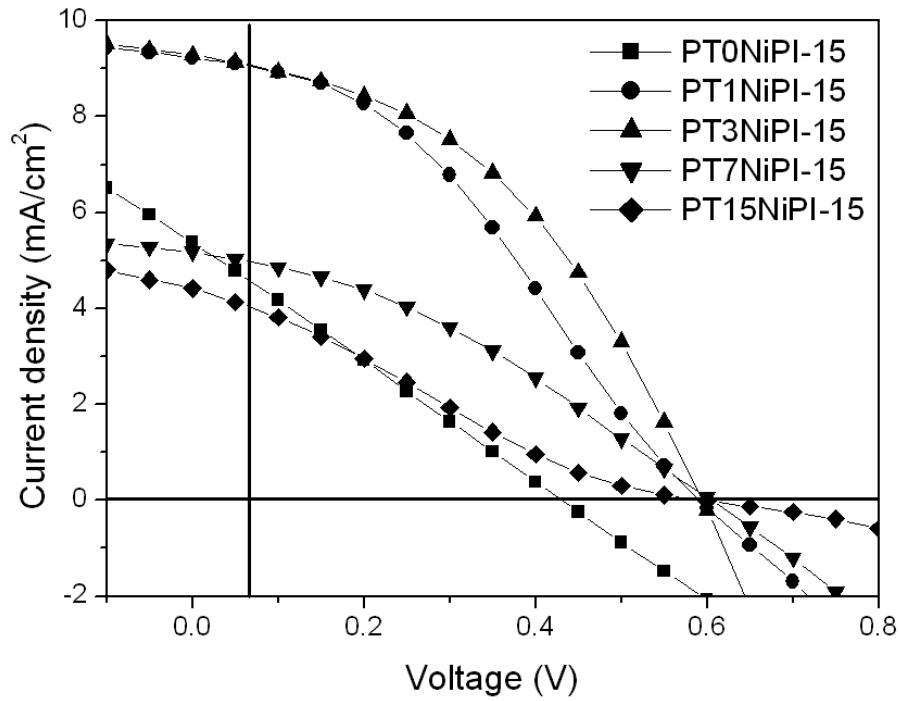


Figure 6.6 *I-V* characteristics of inverted PSCs under AM 1.5 illumination (100 mW cm^{-2}).



Roman *et al.* have reported that the light-trapping effects from active layers on the periodic Al metal nanostructures, and those structures could further enhance PSCs performance [182]. Comparing the dimension of the granular NiPI with the Al grating structure, the NiPI films were believed to have the same effect in PSCs. To complement the observed degree of light confinement in whole devices, herein, we performed reflective UV-vis, reflection haze factor (H_R) and external quantum efficiency (EQE) measurements of overall inverted PSCs process of the plane AlPI and the granular NiPI films. Figure 6.7(A) and figure 6.7(B) showed the SEM image of planar AlPI and granular NiPI films, respectively. In the reflective UV-vis spectra of absorbance, figure 6.7(C) represents that the granular NiPI films were well-adapted to improve the light-trapping in 200 nm thick P3HT:PCBM cells. Based on the previous reports, [205, 206] the refractive indices of PEDOT:PSS and P3HT:PCBM were 1.1–1.6 and 1.6–2.2, respectively, in the range 400–800 nm. The higher H_R was obtained from rougher NiPI structure through reflective haze factor measurements [Figure 6.8(A)]. The total internal reflection could occur where light travels from a P3HT:PCBM film with a higher refractive index to the PEDOT:PSS film with a lower refractive index. The absorption, haze factor and EQE analysis, Figure 6.7(C)-e, Figure 6.7(C)-f and Figure 6.8(A) show that there were more light absorptions in granular NiPI of devices (PT3NiPI Device) than the planar structures of electrode (PT3AlPI Device) in the range of wavelengths 400–650 nm. The beam of light scattering on the granular NiPI shows better light confinements than planar AlPI of devices. Therefore, a light trapping effect were presumed by the NiPI layer in the range 400–800 nm, hence the EQE of P3HT devices show enhancement in the range 400–620 nm [Figure 6.8(A)]. Although different materials of cathodes may cause to the different device performance, in this study, the comparison of haze factors and EQE results, give some information of optical path length enhancement in the active layer. The Rms of coated photoactive was ca. 5.6 nm and its surface roughness was smoother than NiPI

substrate (Rms~33.8 nm). The cross-sectional TEM image showed the thickness of the photoactive layer was ca. 200 nm and the granular NiPI film can actually be well covered by the photoactive layer. The thin film architecture of device suggests that the variation in the film thickness would not be a problem for charge carrier extraction. As shown in Figure 6.8(B) and 6.8(C), the cartoon illustration summarized the representations of light-reflection and light-scattering properties in PSCs, and the schematic representations can be presumed that, in the active layer, rougher NiPI would induce better of light trapping than planar AlPI.



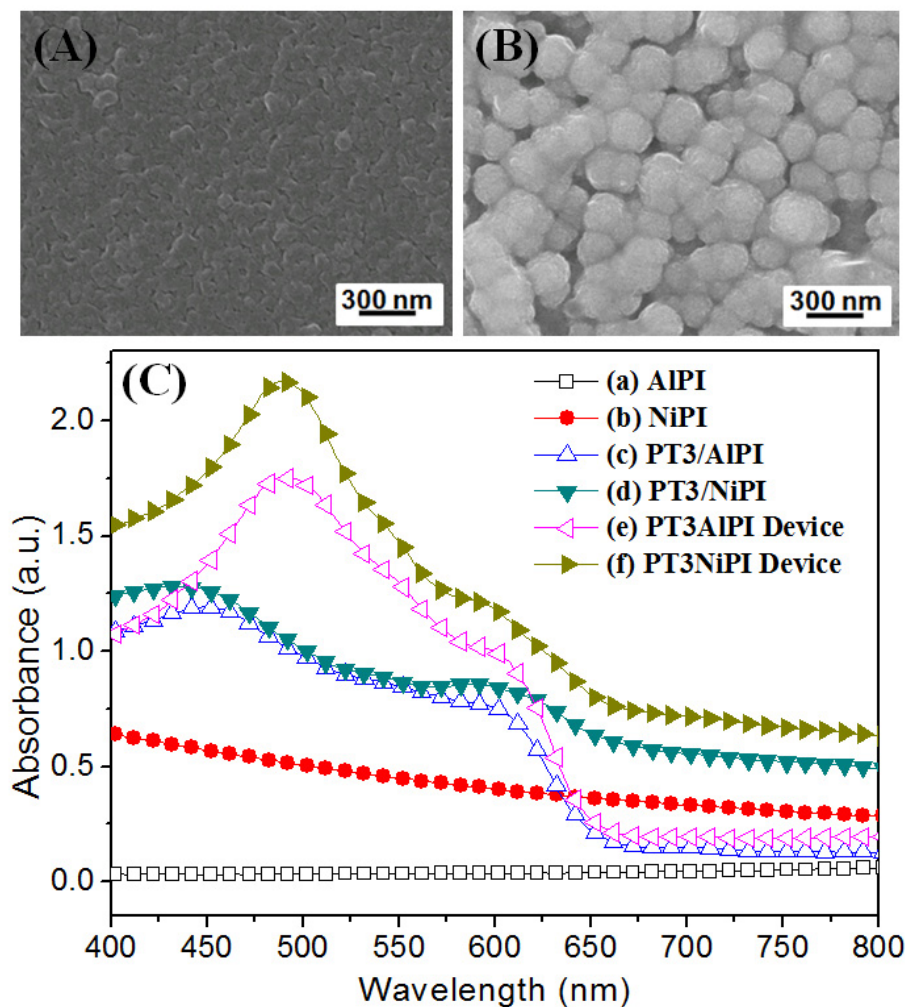


Figure 6.7 SEM images (Top-view) of different structure of cathodes. (A) AlPI: planar AlPI, (B) NiPI: granular NiPI. (C) Reflective UV-vis spectra of films on different structures of cathodes. (a) AlPI: planar AlPI, (b) NiPI: granular NiPI, (c) PT3/AlPI: P3HT:PCBM/TIPD(3.75 wt%)/AlPI, (d) PT3/NiPI: P3HT:PCBM/TIPD(3.75 wt%)/NiPI, (e) PT3AlPI Device: PEDOT:PSS/PT3/AlPI, (f) PT3NiPI Device: PEDOT:PSS/PT3/NiPI.

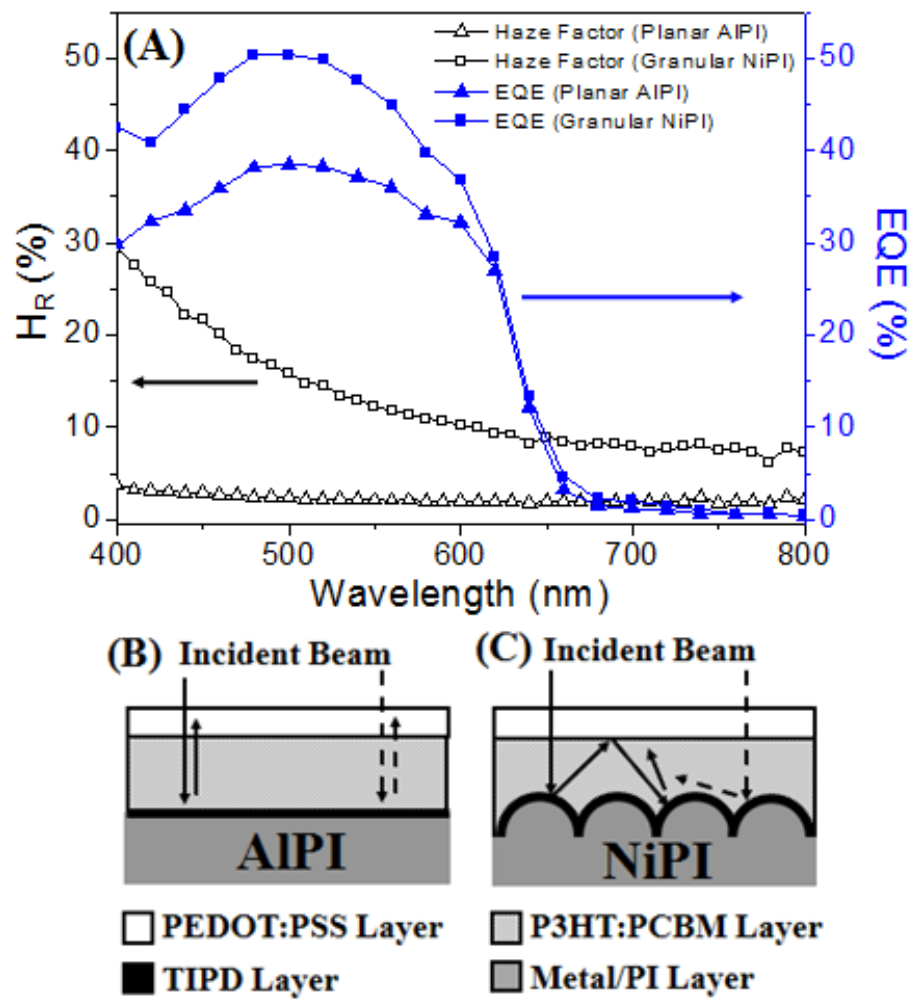


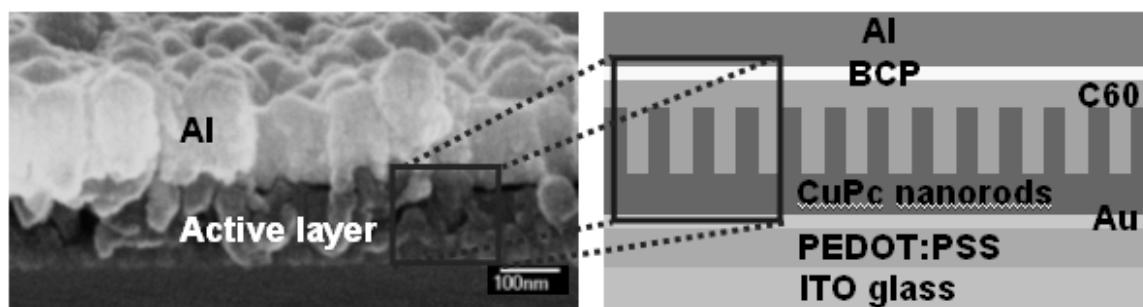
Figure 6.8 (A) Reflection haze factors for different structure of cathodes and the EQE spectra of inverted PSCs on different structure of cathodes. Cartoon representations for inverted PSCs illuminated on different structure of cathodes. (B) Planar AIPI, (C) Granular NiPI.

6.4 Conclusion

We have developed a procedure for the all-solution processing of inverted PSCs on PI substrates. In this approach, the solution processing led to the chemical formation of granular Ni thin films with high conductivity (ca. 2777.8 S cm^{-1}) and a suitable WF for use as back contact cathodes in PSCs. We used a TIPD solution to modify the surface energy of the patterned NiPI film prior to further P3HT:PCBM coating. An analysis of the values of PCE revealed that a suitable concentration of the TIPD coating led to improved PV performance. After performing a mild oxygen plasma treatment for 5 s on the P3HT:PCBM surface, the active layer was appropriately modified for further coating with PEDOT:PSS. Moreover, we further investigated the low-temperature fabrication of high-conductivity PEDOT:PSS films by employing DMSO and ME as additives; using this approach, we obtained a high-conductivity (ca. 283.1 S cm^{-1}) **HDM** film after thermal treatment at just $100 \text{ }^\circ\text{C}$ for 5 min. The ITO-free inverted PSCs incorporating **HDM** films as anodes and **TNiPI** as the modified layer/cathodes exhibited high performance, with the PCE reaching 2.4% under AM 1.5 illumination (100 mW cm^{-2}). Although the deposition of Au grids (thickness at 100 nm) was helpful for decreasing the distance effect of PEDOT:PSS layer (hole collection), the FF of 0.43 is still significantly lower than the FF of 0.64 for standard devices. It was believed that higher conductivity of NiPI films and PEDOT:PSS films still needed for further improving the device performance. As the results of the absorption, haze factor and EQE responses, the granular NiPI was presumed to be a better electrode/substrate through enhancing the light scattering and trapping in inverted PSCs.

Chapter 7

Morphological Control of CuPc and its Application in Organic Solar Cells



We have prepared organic photovoltaic (OPV) cells possessing an ideal bulk heterojunction (BHJ) structure using the self-assembly of copper phthalocyanine (CuPc) as the donor material and fullerene (C₆₀) as the acceptor. The variable self-assembly behavior of CuPc on a diverse range of substrates (surface energies) allowed us to control the morphology of the interface and the degree of carrier transportation within the active layer. We observed rod-like CuPc structures on indium tin oxide (ITO), poly(3,4-ethylenedioxythiophene)-poly(4-styrenesulfonate) (PEDOT:PSS), and Au substrates. Accordingly, the interfaces and continuing transport path between CuPc and fullerene domains could be greatly improved due to the ideal BHJ structure. In this paper, we discuss the mechanisms of producing CuPc rod-like films on ITO, PEDOT:PSS and Au. The OPV cell performance was greatly enhanced when a mixture of horizontal and vertical CuPc rods was present on the PEDOT:PSS surfaces; i.e., the power conversion efficiency was 50 times greater than that of the corresponding device featuring a planar CuPc structure.

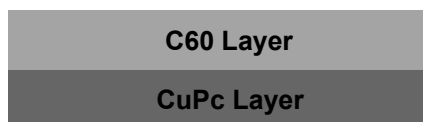
7.1 Introduction

Over the past two decades, organic photovoltaics (OPVs) have received a tremendous amount of attention because of their potential application as green energy devices [207–209]. Indeed, the study of small-molecule solar cells is among the most developed fields of OPVs [210–219]. In conventional small-molecule PV systems, the properties of planar heterojunctions (HJs), mixed donor–acceptor (DA) HJs, and thermodynamically driven HJs [Figures 7.1(a)–(c)] have been discussed widely [209, 220–222]. In typical planar HJ (bilayer DA) devices, a large degree of photogeneration is sacrificed because of the limited exciton diffusion length (LD); hence, the overall power conversion efficiency (PCE) is limited. The exciton diffusion bottleneck has been overcome through the introduction of bulk HJs through co-deposition of the D and A materials; nevertheless, poor charge transport results in low PCE. Although annealing the DA mixture at high temperature to induce phase segregation in the solid state [209] and introducing a DA mixture between D and A layers have been applied successfully to achieve a large DA interface for exciton separation [220–222], the thermodynamically driven random distribution of D and A materials and the limited size of the interfaces for charge transfer can result in inefficient PCE in both of these two cases.

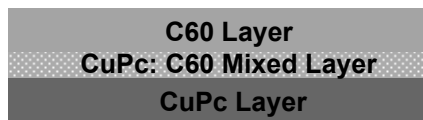
Recently, Forrest et al. used organic vapor phase deposition (OVPD) to grow copper phthalocyanine (CuPc) nanorods onto ITO substrates to form an OPV possessing an ideal BHJ structure [223–225]. This structure plays a significant role in determining the exciton diffusion efficiency, as illustrated in Figure 7.1(d). The photovoltaic performance of such devices can be improved further when the well-controlled CuPc rods are aligned vertically between the two electrodes; in this case, the quality of the interfaces between the D and A layers could be greatly enhanced, thereby reducing the number of hopping events required for efficient charge transport. For example, a high photocurrent and a low recombination

of carriers inside the active layer can be obtained when the diameter of the CuPc rods is controlled within the exciton diffusion length of CuPc (ca. 10 ± 3 nm) [210]. Nevertheless, the fabrication and well-defined vertical alignment of CuPc rods remain difficult tasks.

In a previous study, we measured the field emission properties of CuPc nanofibers formed through low-temperature self-assembly, controlling the deposition conditions using a thermal evaporator (TE) [226]. In contrast, other OVPD systems required a high evaporation temperature (>400 °C) and a carrier gas to fabricate the CuPc rod-like films [223–225]. Using these approaches, CuPc nanorods possessing small diameters (<50 nm) and high-quality vertical arrays (ideal BHJ structure) cannot be formed directly. In this paper, we present a simple method for constructing similar CuPc rod-like films using a commercially available TE. The surface energy of the substrate can be modified to control the morphology of the CuPc film at lower evaporation temperatures (<200 °C). Although a number of authors have reported various CuPc morphologies [227, 228], we currently do not have a full understanding of the mechanism of CuPc rod formation. In this study, we used scanning electron microscopy (SEM), grazing incident X-ray diffraction spectroscopy (GIXRD), high-resolution transmission electron microscopy (HRTEM), tapping-mode atomic force microscopy (AFM), X-ray photoelectron spectroscopy (XPS), and the contact angle analysis to investigate the growth mechanisms of rod-like CuPc films on Au and PEDOT:PSS films. We obtained highly controllable rod-like CuPc films through the formation of intermolecular π - π stacking interactions within a TE. We then utilized these morphologically controlled CuPc structures as ideal BHJ structures within OPV devices [Figure 1(d)]. Herein, we discuss the PV performance of four kinds of HJ structures: planar HJs (**PHJ**), horizontal rod-based BHJs (**h-BHJ**), a mixture of horizontal and vertical rod-based BHJs (**m-BHJ**), and vertical rod-based BHJs (**v-BHJ**).



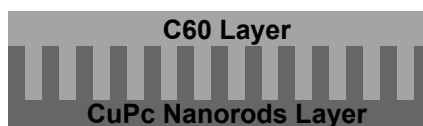
(a) Planar heterojunction



(b) Mixed DA heterojunction

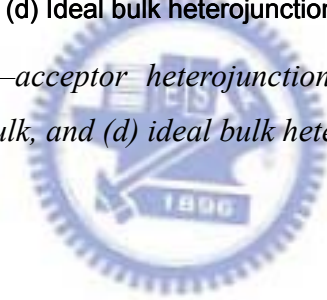


(c) Thermodynamically driven bulk heterojunction



(d) Ideal bulk heterojunction

Figure 7.1 Organic donor–acceptor heterojunctions: (a) planar, (b) mixed DA, (c) thermodynamically driven bulk, and (d) ideal bulk heterojunctions.



7.2 Experimental Details

The donor (D) material used in the devices was copper phthalocyanine (CuPc), obtained from Sigma–Aldrich (sublimation grade) without further purification; it was sublimed onto various anodes. The accept (A) material was fullerene (C₆₀), obtained from Sigma–Aldrich (Sublimed, 99.9%) and used as received. 2,9-Dimethyl-4,7-diphenyl-1,10-phenanthroline (BCP) were purchased from Sigma–Aldrich (99.5%) and used as a exciton blocking layer.

The small-molecule solar cells had the following device structure: anode/CuPc (200 Å)/CuPc:C₆₀ (100 Å)/C₆₀ (300 Å)/BCP (75 Å)/Al (1500 Å). The cells were fabricated on ITO glass (SANYO) substrates, which were cleaned with organic solvents and a plasma cleaner prior to use. The CuPc films were grown through vacuum sublimation in a thermal evaporator at a base pressure of ca. 3×10^{-6} torr. CuPc (C₃₂H₁₆CuN₈) was sublimed onto various anodes, including ITO, PEDOT:PSS-coated ITO (PITO), and Au-coated ITO (AITO), from a heated crucible (ca. 170 °C). The corresponding deposition rates, determined using a quartz crystal microbalance, were ca. 3 Å /s; the morphologies of the CuPc films were controlled using various substrates at various substrate temperatures (T_{sub}).

A JEOL JSM-6500F SEM was used to investigate the thickness and morphology of the CuPc films and the cross-section of the solar cell devices. The crystalline phase of CuPc films was characterized by GIXRD, using a BEDE D1 system and Cu K α radiation. The incident angle of the X-ray beam was fixed at 0.5°. Ultraviolet–visible (UV–Vis) spectra were measured using a Perkin–Elmer Lambda 20 UV–Vis spectrophotometer. The structures of the CuPc nanorods were imaged and analyzed using a JEOL-2010F high-resolution TEM equipped with an Oxford energy dispersive spectrometer. Contact angles and surface energies were measured and calculated using the geometric mean

approximation (GMA) from the FTA-200 dynamic contact analyzer and two standard liquids: H₂O and CH₂I₂. All devices were treated at 150 °C for 0.5 h. Current–voltage (*I–V*) measurements of the OPV devices were conducted using a computer-controlled Keithley 2400 source measurement unit (SMU) equipped with a Peccell solar simulator (AM 1.5, 100 mW/cm²). The phase diagram of the PEDOT:PSS films was analyzed using a VEECO DICP-II AFM operated in the tapping mode (Si tips on Si cantilevers; spring constant: 2 N/m; set point: ca. 0.8-0.9) in air. XPS data were obtained using a VG Scientific Microlab 350 spectrometer operated in the constant analyzer energy mode (pass energy: 50 eV; excitation source: Mg K α , 1253.6 eV). XPS measurements were performed at room temperature and at pressures of less than 10⁻¹⁰ torr.

7.3 Results and discussion

In a previous study [226], we found that the substrate temperature (T_{sub}) was an important factor controlling the dimensions and densities of the resulting CuPc nanofibers. When T_{sub} increased from 100 to 200 °C, the two competitive phenomena of absorption and desorption affected the formation of the rod-like CuPc films on these substrates. For instance, we obtained longer, wider, lower-density CuPc nanofibers on Au substrates when the value of T_{sub} was 200 °C and the heated crucible temperature was 170 °C, relative to those obtained when T_{sub} was 100 °C. In this present study, we selected a substrate temperature of 100 °C to obtain a higher fiber density of smaller-diameter CuPc nanorods. As use as OPV materials, vertically aligned rod-like structures should allow efficient hole carrier transport by reducing the number of hopping events between CuPc units; we expected high fiber densities and smaller diameters to provide larger interfaces for a high-throughput photocurrent after depositing C₆₀. Figures 7.2 presents top-view SEM images of the CuPc films formed on the ITO, PITO, and AITO substrates. We observe that

in-plane horizontal CuPc rods (diameter: ca. 50 nm) formed on ITO [Figure 7.2(a)]; a mixture of horizontal and vertical CuPc rods (diameter: ca. 50 nm) formed on PITO [Figure 7.2(b)]; and relatively well-defined vertically arrayed CuPc rods (diameter: <50 nm) formed on AITO [Figure 7.2(c)]. Figures 7.2(a)-1, 7.2(b)-1, and 7.2(c)-1 display cartoon representations of the morphologies of the CuPc films formed on the ITO, PITO, and AITO substrates, respectively.

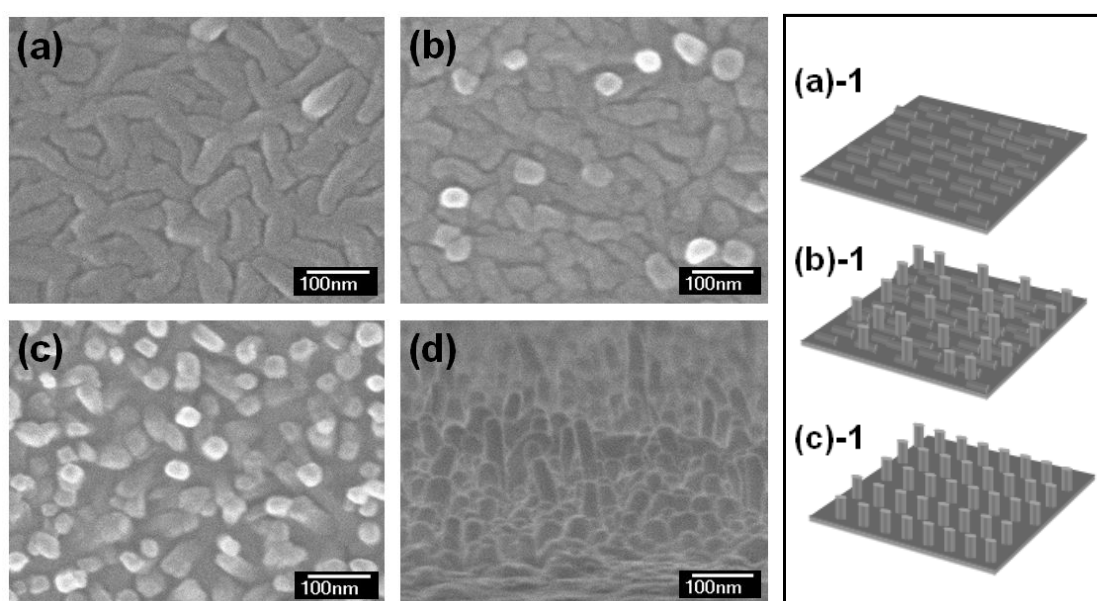


Figure 7.2 SEM images of TE-grown CuPc films on (a) ITO, (b) PITO, (c) AITO (top-view), and (d) AITO (side-view) substrates. The cartoon images (a)-1~(c)-1 represent the morphologies in (a)~(c), respectively.

The dimensions of vertically arrayed CuPc rods can be optimized to provide improved OPV performance. In this study, we prepared rod-like CuPc films of various lengths by changing the deposition time. The heights of the surface-grown rod-like films were controlled using a quartz crystal microbalance; we chose values of 100, 200, 300, and 500 Å, respectively [Figures 7.3(a)–(d)]. On the AITO substrate, we observed similar thicknesses for the continuous CuPc films formed under the conditions [cf. Figures 7.3(b) and 7.3(c)], suggesting that the growth mechanism may be divided into two steps. In the first step, CuPc tends to form a planar structure (ca. 40 nm); in the second step, CuPc rods of various lengths grow from the surface of this film. This growth mechanism presumes that the CuPc underlayer presents deposition sites for the formation of the resulting CuPc rods [229]. Figure 7.3(d) reveals that a thicker CuPc continuous film (ca. 70 nm) formed in the first step and longer CuPc rods in the second. Although the diameters of the CuPc rods (ca. 25 nm) were independent of the deposition time, their lengths were controllable by changing the deposition time. Figure 7.3(e) provides a cartoon representation of the surface growth of the CuPc rods; the thickness of the film grown in the first step is represented by the letter T , and the length and diameter of the rods grown in the second step are represented by the letters L and D , respectively. When a thickness of 100 Å was selected from the quartz crystal microbalance, the value of L of the vertical CuPc rods was ca. 25–30 nm with aspect ratio of ca. 1–1.2; T was too thin to identify [Figure 7.3(a)]. The vertical CuPc rods in the 200-Å-thick sample had rod dimensions ranging from 45 to 90 nm, with an aspect ratio in the range 1.8–3.6, and a value of T of ca. 35 nm [Figure 7.3(b)]. In Figure 7.3(c), the value of L of the vertical CuPc rods (300 Å thick) was ca. 90–150 nm, with an aspect ratio of ca. 3.6–6, and a value of T of 35–40 nm. The value of L of the vertical CuPc rods (500 Å thick) was ca. 90–1000 nm with an aspect ratio of ca. 3.6–40 and a value of T of ca. 70 nm [Figure 7.3(d)]. Consequently, when a thicker CuPc layer

was deposited, the length of the CuPc nanorods lacked uniformity and they were poorly vertically arrayed. To produce highly folded DA interfaces with higher exciton diffusion efficiency and fewer defects, we selected the CuPc rods of shorter length and higher vertically arrayed structure in Figure 7.3(b) to further investigate their potential PV cell applications.

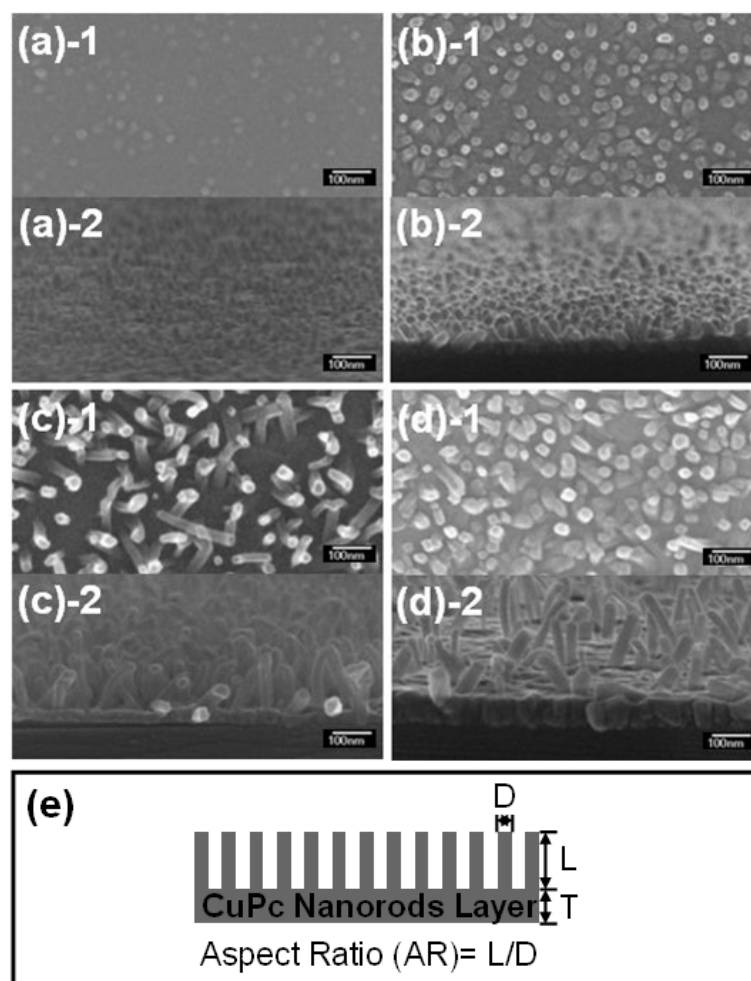


Figure 7.3 SEM images of vertical rod-like CuPc films grown on Au substrates at thicknesses (measured using a quartz crystal microbalance) of (a) 100, (b) 200, (c) 300, and (d) 500 Å. (e) Cartoon representation of an ideal BHJ of CuPc films. All scale bars are 100 nm.

The two principal phases of CuPc are the so-called α and β phases [229]. The conductivity of the β film ($2 \times 10^{-6} \text{ S m}^{-1}$) is much lower than that of the α film ($2 \times 10^{-4} \text{ S m}^{-1}$) [230], presumably because the overlap in the π - π stacking is higher in α phase than in the β phase. After annealing or depositing at temperatures greater than $200 \text{ }^\circ\text{C}$ [231], the β -phase CuPc films reveal a 2θ peak at 7.02° . Figure 7.4 presents GIXRD spectra of the CuPc powders and CuPc films formed on the various substrates at values of T_{sub} of 25 and $100 \text{ }^\circ\text{C}$. By controlling the surface energy of the ITO substrate and varying the value of T_{sub} , all of the CuPc films could be formed in the α phase with a signal at a 2θ value at 6.83° ; such high-conductivity α -phase CuPc rod-like films are suitable for mediating exciton transport within OPV devices.

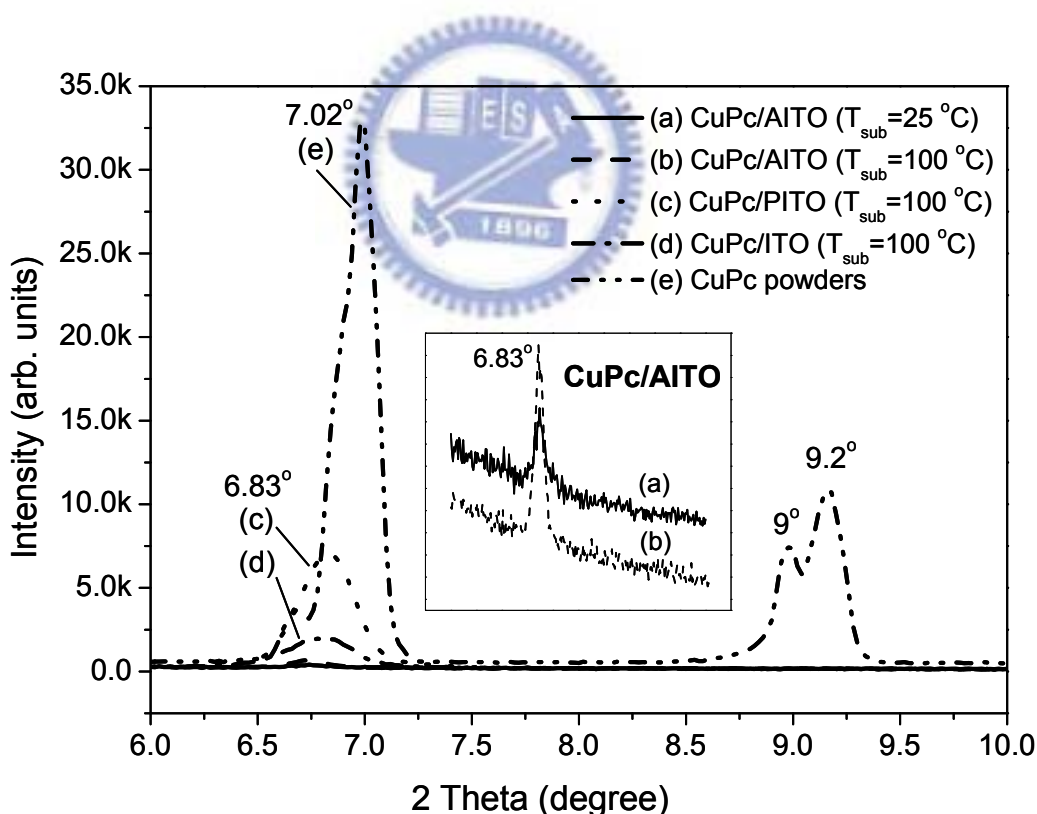


Figure 7.4 GIXRD spectra of CuPc powders and films deposited on various substrates at various substrate temperatures: (a) AITO ($T_{\text{sub}} = 25 \text{ }^\circ\text{C}$), (b) AITO ($T_{\text{sub}} = 100 \text{ }^\circ\text{C}$), (c) PITO ($T_{\text{sub}} = 100 \text{ }^\circ\text{C}$), (d) ITO ($T_{\text{sub}} = 100 \text{ }^\circ\text{C}$), and (e) CuPc powders.

Figure 7.5(a) presents a top-view SEM image of a Au thin film (ca. 20 Å) on an ITO glass substrate; this film is composed of non-continuous Au nanoparticles (NPs). Figures 7.5(b)–(d) display TEM images of the CuPc rods deposited on the Au substrates at a value of T_{sub} of 100 °C; Figure 7.5(e) presents the corresponding EDX analysis. CuPc rods having a diameter of ca. 25 nm formed on top of the Au NPs, presumably through crystallization. In our previous study [226], we found that CuPc molecules deposited on either a continuous Au layer (ca. 250 Å) or a Au NP layer (ca. 20 Å) exhibited vertical rod-like structures when T_{sub} was 100 °C. Our present findings reveal that the surface energy and the temperature of the substrate are two major factors affecting the formation of the various CuPc morphologies (Table 7.1). The variation in morphology that occurred upon increasing the temperature can be explained by considering the following equation [232]:

$$\gamma = \gamma^0 [1 - (T/T_c)]^n \quad (1)$$

where γ is the surface energy at temperature T and γ^0 is the surface energy at the critical temperature (T_c); the value of n may be close to unity for anodes. As the temperature increases, substrates having a lower surface energy (e.g., the value of γ^0 for Au is 39.40 mJ/m²) would induce vertical alignment of CuPc rods, whereas horizontal CuPc rods would grow on high-surface-energy surfaces (e.g., the value of γ^0 for ITO is 62.62 mJ/m²). Although the surface energy of PEDOT:PSS (ca. 74.28 mJ/m²) is higher than that of ITO, we obtained a mixture of horizontal and vertical CuPc rods. This random distribution of horizontal and vertical rods may have arisen from the inconsistent surface energy of PEDOT:PSS, which is composed of hydrophilic PSS components and hydrophobic PEDOT-PSS domains that undergo nanophase separation, as observed in AFM phase images [233].

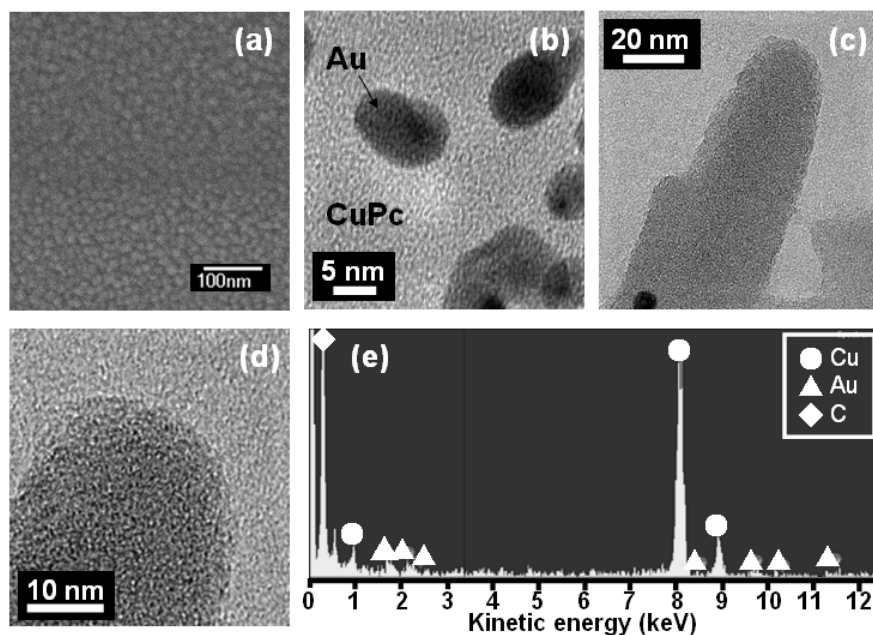


Figure 7.5 (a) SEM (top-view) image of a thin layer of Au on an ITO substrate. (b)–(d) TEM images and (e) EDX analysis of CuPc rods deposited on the Au substrates at $T_{sub} = 100$ °C. (b) Bottom section of CuPc rods. (c) CuPc rods. (d) HR-TEM images of the upper section of CuPc rods.

Table 7.1 Effect of substrate on CuPc film morphology. (Note: ITO: Indium tin oxide glass treated with a plasma cleaner. PITO: PEDOT:PSS films (ca. 50 nm) coated on ITO. AITO: Au layers (ca. 20 Å) deposited by TE on ITO.)

Substrate	Surface energy (mJ m^{-2})	Morphology of CuPc film ($T_{sub} = 100$ °C)	Diameter of CuPc rods (nm) ($T_{sub} = 100$ °C)
ITO	62.62 ^a	Horizontal rods ^c	about 50 ^c
PITO	74.28 ^a	Horizontal and vertical rods ^c	about 50 ^c
AITO	39.40 ^a	Vertical rods ^c	about 25 ^c
PEDOT	50.59 ^b	Vertical rods ^d	about 50 ^c
PSS	74.29 ^b	Horizontal rods ^d	about 50 ^c

a: This value was calculated using the geometric mean approximation (GMA) from the measurements of the advancing contact of H_2O and CH_2I_2

b: This value was calculated using the equation $\gamma = 0.75(E_{coh}/V)^{2/3}$ [234].

c: The morphology was identified from SEM results.

d: The morphology was presumed from surface energy differences in the PEDOT:PSS film.

To verify the origin of morphological variation of the sample formed on the PEDOT:PSS surface, we calculated the surface energies obtained from cohesive energy density (CED) and XPS analyses and examined AFM and SEM images to distinguish the factors affecting the growth of horizontal and vertical CuPc rods (Figure 7.6). The individual surface energies of PEDOT and PSS solid films can exhibit large variations; we estimated the surface energies (γ) of PEDOT and PSS from the cohesive energy density (CED) values obtained using the empirical equation given by Zisman [234]:

$$\gamma = 0.75(\text{CED})^{2/3} \quad (2)$$

$$\text{CED} = E_{\text{coh}}/V_{\text{mol}} \quad (3)$$

Table 7.2 lists the surface energies calculated using eqs 2 and 3. The cohesive energies (E_{coh}) and molecular volumes (V_{mol}) of the various structural groups were obtained from the literature [235]; the individual groups of PEDOT and PSS are also listed in Table 7.2. Accordingly, we estimated the surface energies of PEDOT and PSS to be 50.59 and 74.29 mJ/m², respectively, suggesting that out-of-plane CuPc rods would form on PEDOT domains ($\gamma = 50.59$ mJ/m²) and in-plane CuPc rods on PSS domains ($\gamma = 74.29$ mJ/m²). From contact angle analysis, we found that the surface energy of the PEDOT:PSS film was ca. 74.28 mJ/m², close to the value calculated for PSS. This result indicates that traditional contact angle analysis cannot be used alone to determine the effect of the surface energy on the growth of CuPc nanorods. In addition, our findings suggest that variations in the surface energy on the PEDOT:PSS surface were probably responsible for the variations in the CuPc morphology. The topography and phase images of the PEDOT:PSS film [Figures 7.6(a) and 7.6(b)] were similar to those reported by Crispin et al. [233], with separated PEDOT-PSS and PSS domains. In the phase image, the hard domains appear as bright regions, which we attribute to PEDOT-PSS domains, whereas the dark regions denote the soft segments that belonged to excess PSS domains [233]. The main morphological feature

of the PEDOT:PSS film is a homogeneous distribution of the two components on the nanoscale. Figure 7.6(c) displays a top-view SEM image of the rod-like CuPc film deposited on the PEDOT:PSS film. The distribution of vertical CuPc domains is similar to the distribution of PEDOT-PSS domains in the PSS matrix. Figure 6(d) displays a cross-sectional image that we used to provide an estimate of the percentage of vertical CuPc rods (ca. 13–16%). The XPS analysis also indicates that the atomic percentage of PEDOT was ca. 15.8% [Figure 7.6(e)]. The combined results from the AFM, XPS, and surface energy analyses suggest that vertical CuPc rods prefer to grow on the surfaces of the PEDOT-PSS domains (PEDOT rich domains), where CuPc tends to form horizontal rod structures in the PSS domains (PSS rich domains).



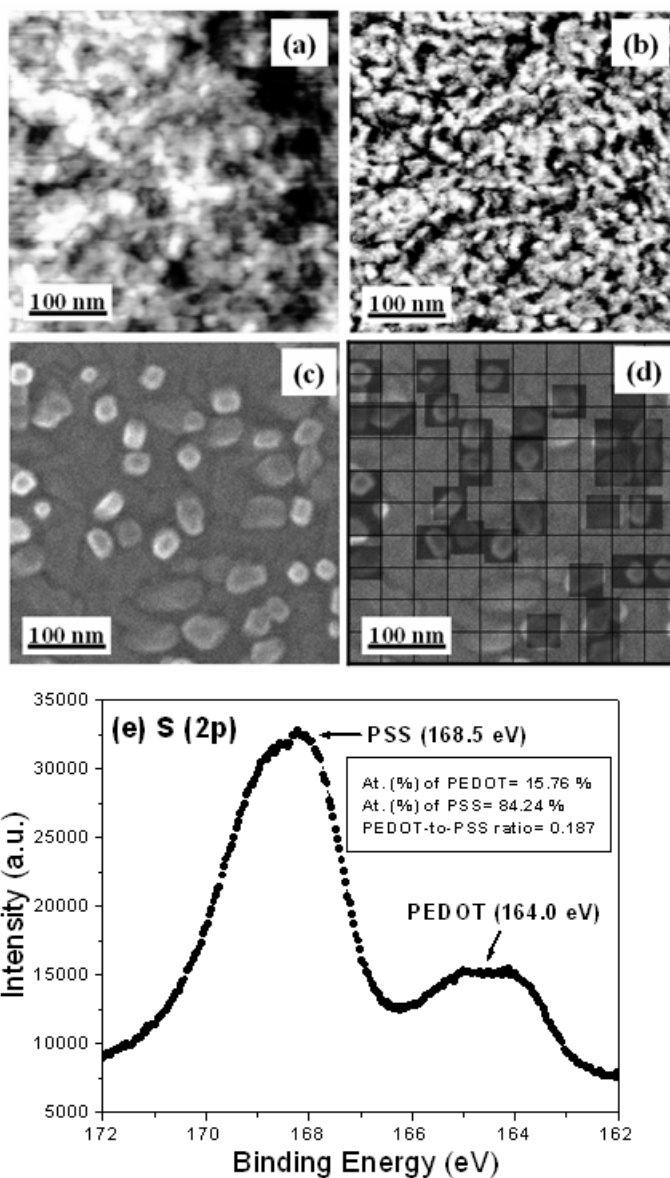
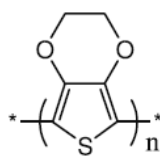
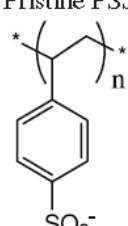
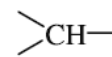
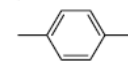


Figure 7.6 AFM images [topographic (a) and phase (b)] of the PITO surface. SEM images [top-view (c) and estimate (d)] of CuPc rod-like film on the PITO. (e) S(2p) core level spectra of the PITO surface.

Table 7.2 Calculated values of surface energy for polymers [234, 235].

Pristine PEDOT			Pristine PSS		
					
Group	E_{coh} (J mol ⁻¹)	V (cm ³ mol ⁻¹)	Group	E_{coh} (J mol ⁻¹)	V (cm ³ mol ⁻¹)
-CH ₂ -	2 × (4940)	2 × (16.1)	-CH ₂ -	1 × (4940)	1 × (16.1)
-O-	2 × (3350)	2 × (3.8)	 CH-	1 × (3430)	1 × (-1.0)
Ring closure 5	1 × (1050)	1 × (16)	 -	1 × (31 940)	1 × (52.4)
Conjugation in ring (double bond)	2 × (1670)	2 × (-2.2)	-SO ₃ ⁻	1 × (18 840)	1 × (27.6)
-S-	1 × (14 150)	1 × (12.0)			
$\gamma = 0.75(E_{\text{coh}}/V)^{2/3}$ $= 0.75(35\,120/63.4)^{2/3}$ $= 50.59(\text{mJ m}^{-2})$			$\gamma = 0.75(E_{\text{coh}}/V)^{2/3}$ $= 0.75(95\,630/97)^{2/3}$ $= 74.29(\text{mJ m}^{-2})$		



We fabricated OPV cells (glass/anode/CuPc/CuPc:C₆₀/C₆₀/BCP/Al) [210] featuring ITO [work function (WF) = 4.8 eV], PEDOT:PSS (WF = 5.2 eV), and Au (WF = 5.2 eV) as anodes; Figure 7.7(A) provides a schematic energy level diagram. In an ideal photovoltaic device, the electrode must have high transparency and the active layer must exhibit high absorption of visible light. Figure 7.7(B) presents the transmittance behavior of the fully processed solar cells. The absorption of CuPc reaches its maximum at 620 nm; the transmittance of the pristine ITO glass at 620 nm was 83.5% [Figures 7.7(B)-a]. After a thin Au film (ca. 20 Å) had been deposited, the transmittance at 620 nm of AITO decreased to 65% [Figures 7.7(B)-b]. After the active layers had been deposited onto AITO [Figures 7.7(B)-c and 7.7(B)-d], the transmittance in the range 350–800 nm decreased substantially. Figure 7.7(C) presents the architecture and an SEM image of a typical OPV cell. The cross-sectional image of the device clearly reveals the individual layers. The thicknesses of the ITO, PEDOT, and Al layers were 190, 50, and 120 nm, respectively. The thickness of the active layer in this cell was ca. 120 nm; note, however, that it could be controlled by changing the deposition time.

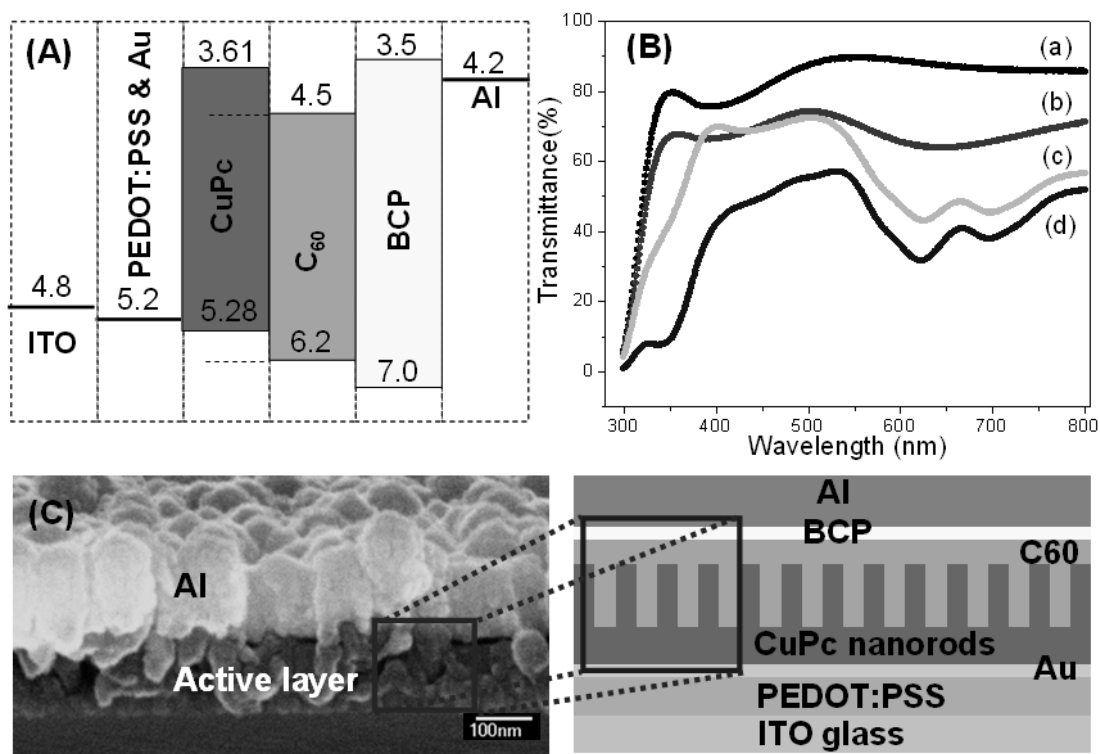


Figure 7.7 (A) Schematic representation of the energy levels of the devices. (B) UV-Vis spectral transmittance of fully processed solar cells incorporating various films: (a) ITO, (b) AITO, (c) rod-like CuPc (200 Å)/AITO, (d) C₆₀ (300 Å)/CuPc:C₆₀ (1:1) (100 Å)/rod-like CuPc (200 Å)/AITO. (C) Cross-sectional image of the device having the structure AITO/CuPc (200 Å)/CuPc:C₆₀ (100 Å)/C₆₀ (300 Å)/BCP (75 Å)/Al.

We conducted comparative experiments [Figure 7.8(A)] of OPV devices featuring the various HJ morphologies, including **PHJ** (CuPc on ITO or PITO; $T_{\text{sub}} = 25\text{ }^{\circ}\text{C}$), **h-BHJ** (CuPc on ITO; $T_{\text{sub}} = 100\text{ }^{\circ}\text{C}$), **m-BHJ** (CuPc on PITO; $T_{\text{sub}} = 100\text{ }^{\circ}\text{C}$), and **v-BHJ** (CuPc on AITO; $T_{\text{sub}} = 100\text{ }^{\circ}\text{C}$). The CuPc morphology was affected by the substrate temperature, with higher values of T_{sub} decreasing the surface energy of a particular substrate, thereby resulting in rod-like films. We constructed the **PHJ** structure at a value of T_{sub} of $25\text{ }^{\circ}\text{C}$; we obtained the rod-like structures at substrate temperatures of $100\text{ }^{\circ}\text{C}$. Figure 7.8(B) reveals the J - V curve characteristics of devices having the configuration anode/CuPc (200 Å)/CuPc:C₆₀ (1:1) (100 Å)/C₆₀ (300 Å)/BCP (75 Å)/Al under illumination at 100 mW/cm^2 ; these devices were all annealed at $150\text{ }^{\circ}\text{C}$ for 30 min prior to testing. In the absence of thermal treatment, the variation of PCE values of devices based on rod-like structures (i.e., **h-BHJ**, **m-BHJ**, and **v-BHJ**) was large from different batches. Because many defects existed at the interdigitated DA interfaces, their performance was sacrificed as a result of large interfacial resistances. Table 7.3 summarizes the performance of each device. The **PHJ** devices (a) and (b), which we constructed on CuPc/ITO and CuPc/PITO, respectively, performed poorly, as expected. Device (c) possessing the **h-BHJ** structure exhibited somewhat improved performance. The cell of device (d), incorporating the **m-BHJ** structure, exhibited the highest value of PCE (0.509%) among this series of devices. Notably, device (e), containing the ideal **v-BHJ** structure, performed poorly; its value of PCE was lower than that of device (d) primarily because of a remarkable decrease in current density, which we suspect was caused by the different UV-Vis spectra of these devices, i.e., the absorption of visible light was reduced by the presence of the Au layer. Thus, although we managed to form the ideal BHJ structure on the Au substrate, there are some problems that must be solved if it is to perform well in solar cells. Because device (e) exhibited a smaller open-circuit voltage than that of either device (c) or (d), one such issue

may be current shunt paths between ITO and CuPc caused by the non-continuous Au NP films [224]. Another issue may be the formation of defects between the interdigitated DA interfaces during this TE process, which would obviously occur to a lesser degree in the **h-BHJ** and **m-BHJ** device structures [223]. Therefore, the best performing BHJ solar cell was the **m-BHJ** device, which we suspect contained a lower number of packing defects and a lower density of vertical CuPc nanorods in the active layer.



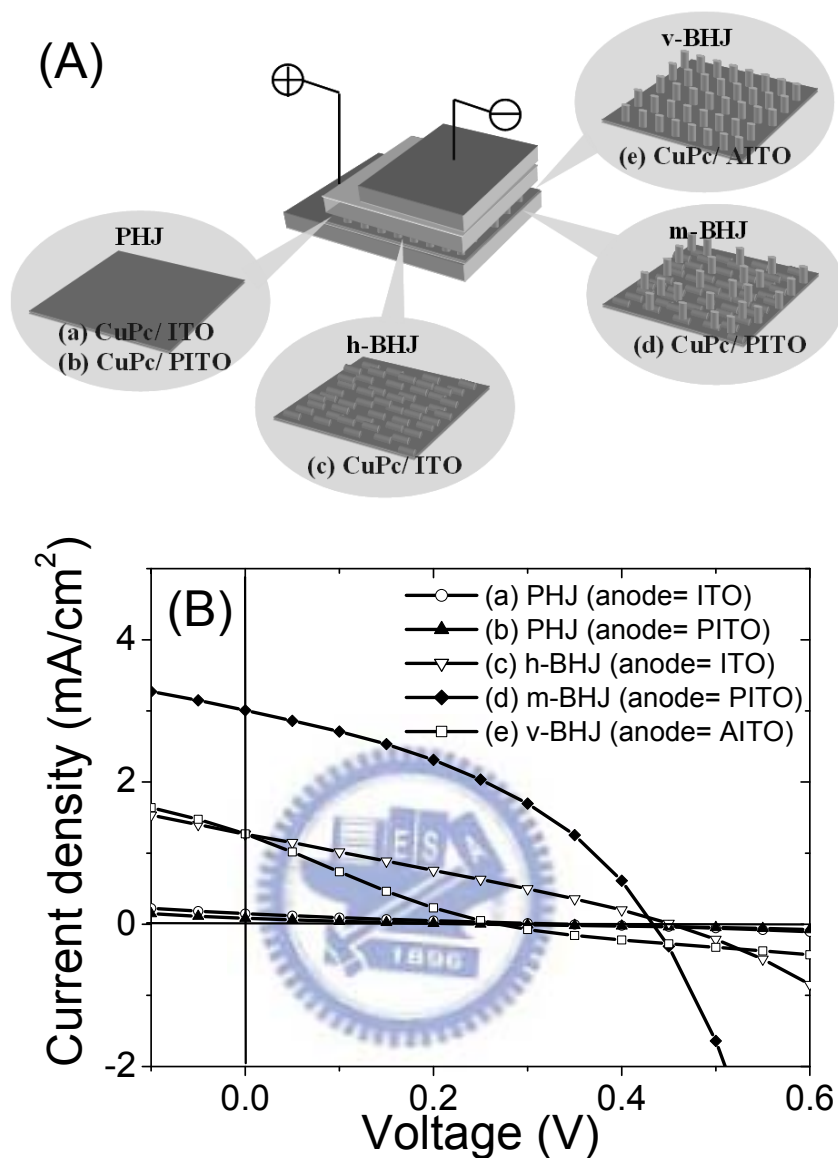


Figure 7.8 (A) Cartoon representations of four types of DA interfaces in solar cells. (B) *J*–*V* curves of devices possessing the configuration anode/CuPc (200 Å)/CuPc:C₆₀ (1:1) (100 Å)/C₆₀ (300 Å)/BCP (75 Å)/Al under illumination (100 mW/cm²), featuring various CuPc morphologies formed under various annealing temperatures.

Table 7.3 Performance of CuPc films in photovoltaic cells. All devices were measured under illumination of AM 1.5 (100 mW/cm²). (Note: **PHJ**: Planar heterojunction structure. **h-BHJ**: Horizontal-rod-based bulk heterojunction structure. **m-BHJ**: Mixture of horizontal- and vertical-rod bulk heterojunction structure. **v-BHJ**: Vertical-rod-based bulk heterojunction structure.

Device	Anode	Type of DA structure	J_{sc} (mA cm ⁻²)	V_{oc} (V)	FF	PCE (%)
(a)	ITO	PHJ	0.149	0.338	0.207	0.0104
(b)	PITO	PHJ	0.0836	0.259	0.194	0.0042
(c)	ITO	h-BHJ	1.27	0.453	0.275	0.1580
(d)	PITO	m-BHJ	3.02	0.438	0.386	0.5090
(e)	AITO	v-BHJ	1.27	0.27	0.215	0.0737



7.4 Conclusion

We have constructed low-molecular-weight organic solar cells using CuPc as the donor and C₆₀ as the acceptor and featuring four types of CuPc morphology. The CuPc morphology could be controlled by varying the surface energy and temperature of the substrates. When using ITO, PITO, and AITO as the substrates, the resulting CuPc morphologies were horizontal rods, a mixture of horizontal and vertical rods, and vertically aligned rods, respectively. Thus, substrates possessing lower surface energies (e.g., Au: $\gamma^0 = 39.40 \text{ mJ/m}^2$) induced vertical alignment of the CuPc rods, with horizontal CuPc rods forming on high-surface-energy surfaces (e.g., ITO: $\gamma^0 = 62.62 \text{ mJ/m}^2$). A combination of AFM, XPS, and surface energy analyses suggested that vertical CuPc rods preferred to grow on the PEDOT rich domains of the PITO surface, whereas horizontal CuPc rods formed preferably on its PSS rich domains. CuPc rods possessing controllable diameters (ca. 25 nm) and lengths (ca. 25–1000 nm) were obtained on AITO; they possessed an interdigitated DA structure similar to that of an ideal BHJ solar cell. After thermal annealing the devices at ca. 150 °C for 30 min, we observed (from GIXRD analysis) no changes in the crystal phases, the CuPc layers maintain the high conductivity α phase through the process. Thus, the values of PCE of CuPc/C₆₀-based solar cells can be enhanced as a result of the higher degree of folded interfaces upon changing the CuPc structure from planar to horizontal and vertical rods.

Chapter 8

Conclusions and Prospects

In this dissertation, I report the fabrication and characterization of flexible electrodes, in which solution processed circuits, cathodes and anodes for flexible organic solar cells (OSCs) are demonstrated. First, I devise an all-solution method for fabricating thin Ni films on PI (NiPI) with high adhesion and conductivity for the use of roll-to-roll manufacturing processes in producing flexible printed circuits for flexible electronics. Then, I invent a simple method to enhance the conductivity of PEDOT:PSS films through the use of spin-coating method with various surface-modified compounds, and apply the modified PEDOT:PSS films as anodes for ITO-free polymer solar cells (PSCs). Finally, I devise a method of manufacturing inverted PSCs incorporating two solution-processed electrodes, namely surface-nickelized polyimide films (NiPI films) as cathodes and high-conductivity PEDOT:PSS films as anodes, and a sandwiched active layer of a bulk heterojunction comprised of P3HT and PCBM. Furthermore, I report the small molecular OSC systems possessing an ideal BHJ structure using the self-assembly of CuPc as the donor material and C₆₀ as the acceptor. The primary results obtained in this dissertation and prospects are summarized as follows:

- (1) The fabrication of high conductivity NiPI films (ca. 2700 S cm⁻¹) benefited by a fully solution-based process was obtained without any Pd catalyst. When using the adhesive tape testing method (ASTM 3359-95) to roughly measure the adhesion between the nickel and polyimide phases, there was excellent adhesive performance in between. The outstanding electrical and adhesive performances of NIPI films were proved to be

suitable for applying in flexible electronics.

- (2) When electroplating copper on NiPI films, the flexible printed circuit boards (FPCB) have been obtained and the best peel strength between the copper and PI phases was ca. 1 kg/cm (Cu layer, 35-40 μ m) and this value was similar to the one obtained by the method of sputtering copper with the pre-plasma treatment on PI. As the results of the preliminary peel strength and TEM images responses, the NiPI film was presumed to be a better adhesive-promoting layer through forming the heterojunction interface between Ni and PI phases to enhance the adhesion property.
- (3) I have learnt from the series of studies that certain factors would affect the surface morphology of NiPI film. For instance, if longer treating time of KOH aqueous solution or longer dipping time of EN solution was selected, the planar morphology of NiPI could be obtained (see chapter 4). If shorter treating time of KOH aqueous solution or shorter dipping time of EN solution was selected, the granular morphology of NiPI could be achieved to apply in inverted PSCs (see chapter 6).
- (4) There was a latent roughness difference through fabricating PI films on rigid substrates, especially occurring in soft chemical structure of PI films. Compared with the contact angle and AFM results on both sides of PI films, it was presumed that rougher PI (A side) would enhance the ability of imide ring opening through using the alkaline hydrolysis method. If higher concentration (> 3 M) of $\text{KOH}_{(\text{aq.})}$ was selected, larger amount of opened imide rings was easily peel off PI through treating alkaline hydrolysis at longer period of time. Therefore, when applying this technique in roll-to-roll process, the issue on how to reduce the morphology difference on both sides of PI must be further considered (see chapter 4).

- (5) I have employed Raman and UV–Vis spectroscopy, SEM, tapping-mode AFM, TEM, and XPS to investigate the origin of decreasing on sheet resistance due to solvent-modified PEDOT:PSS films as transparent conducting anodes. By comparing the variation in conductivity of the modified films, I conclude that phase segregation enabled the formation of longer conduction paths of PEDOT-PSS domains. This phenomenon was the major influence on the conductivity enhancement; the transformation of the PEDOT structure and the decrease in the content of PSS domains on the polymer surface were secondary effects. ITO-free solar cells fabricated using these high-conductivity PEDOT:PSS films as anodes exhibited a high performance. The PCEs of the solar cell devices incorporating ME- and EG-modified PEDOT:PSS films reached 3.13 and 3.39%, respectively, under illumination of AM 1.5 (100 mW cm^{-2}). Although there was obviously distance effect ($> 1 \text{ mm}$) by using the ME- and EG-modified PEDOT:PSS films as anodes, combining the techniques of these high conductivity PEDOT:PSS and random mesh of silver nanowires systems was believed to enhance the conductivity for applying in ITO-free devices (see chapter 5).
- (6) The high conductivity ME-modified PEDOT:PSS film (ca. 283 S cm^{-1}) appears to be more suitable for plastic substrates because it does not require a very high temperature ($>150 \text{ }^\circ\text{C}$) to remove any polyalcohol and, thereby, decreases the likelihood of destroying the active layer (see chapter 6).
- (7) We have developed a procedure for the all-solution processing of ITO-free inverted PSCs on PI substrates. The inverted PSCs incorporating **HDM** films as anodes and **TNiPI** as the modified layer/cathodes exhibited high performance, with the PCE reaching 2.4% under AM 1.5 illumination (100 mWcm^{-2}). Although the deposition of

Au grids (thickness at 100 nm) was helpful in decreasing the distance effect of PEDOT:PSS layer (hole collection), the FF of 0.43 is still significantly lower than the FF of 0.64 for standard devices. It was believed that more efforts would be required in developing higher conductive NiPI films and PEDOT:PSS films to further enhance the device performance (see chapter 6).

- (8) Based on the advantage of light-scattering and light-trapping in inverted PSCs on granular NiPI, this technique was believed to be suitable for applying on the all-solution-processed polymer tandem cells embedded on flexible substrates. Combining the low-bandgap (LGB; 1.3-1.5 eV) and P3HT materials to absorb the full range of the solar spectrum, I assumed a higher performance of PSCs could be achieved in the near future. The schematic energy level of tandem cells was presented in Figure 8.1.

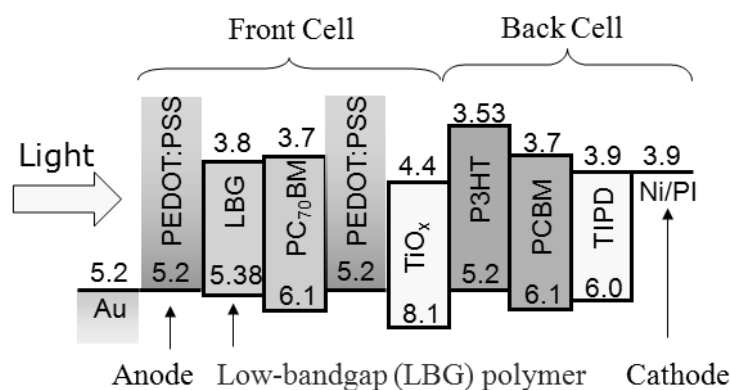


Figure 8.1 Schematic energy level of tandem cells on granular NiPI.

- (9) When using NiPI films as the back contact electrode/substrates in inverted PSCs, the work function, conductivity and granular size of NiPI film were three major factors in determining the device performance. In the follow-up investigation of NiPI, the work function could be easily changed from 3.9 to 6.6 eV with doping some metal elements, and it would directly affect the charge collection. Higher conductivity NiPI was believed to reduce the series resistance, and different granular size of NiPI was

believed to cause different light-scattering and light-trapping effects in devices (see chapter 6). Therefore, based on the comprehensive studies of those three factors, the optimized performance of the inverted devices could be obtained in the future.

(10) We have constructed small molecular organic solar cells using CuPc as the donor and C₆₀ as the acceptor and featuring four types of CuPc morphology. The morphology of CuPc could be controlled by varying the surface energy and temperature of the substrates to fabricate an interdigitated DA structure similar to that of an ideal BHJ solar cell. When using ITO, PITO, and AITO as the substrates, the resulting CuPc morphologies were horizontal rods, a mixture of horizontal and vertical rods, and vertically aligned rods, respectively. Thus, substrates possessing lower surface energies (e.g., Au: $\gamma^0 = 39.40 \text{ mJ/m}^2$) would induce a vertical alignment of the CuPc rods, while the horizontal CuPc rods could be formed on high-surface-energy surfaces (e.g., ITO: $\gamma^0 = 62.62 \text{ mJ/m}^2$). The values of PCE of CuPc/C₆₀-based solar cells can be enhanced as a result of the higher degree of folded interfaces upon changing the CuPc structure from planar to horizontal and vertical rods.

(11) The surface energy difference of PEDOT and PSS domains was presented to explain the morphology difference of CuPc films on PEDOT:PSS substrates. We estimated the surface energies of PEDOT and PSS by using the empirical equation given by Zisman to be 50.59 and 74.29 mJ/m², respectively. Furthermore, AFM and XPS results suggested that out-of-plane CuPc rods would grow on PEDOT domains ($\gamma = 50.59 \text{ mJ/m}^2$) while in-plane CuPc rods would be favored on PSS domains ($\gamma = 74.29 \text{ mJ/m}^2$). Based on our previous report (see chapter 5), it mentioned that a higher solvent polarity resulted in lower amounts of PSS remaining on the surfaces of the PEDOT:PSS films. It was believed that the optimized condition of this OSCs could be

introduced to change the PEDOT-to-PSS ratio on PEDOT:PSS films and indirectly control the ratio of out-of-plane and in-plane CuPc rod-like structures in devices.



References

Chapter 1 Introduction

- [1] M.A. Green, K. Emery, D.L. King, Y. Hishikawa, W. Warta, *Prog. Photovoltaics: Res. Appl.* **15**, 35 (2007).
- [2] H. Sirringhaus, T. Kawase, R. H. Friend, T. Shimoda, M. Inbasekaran, W. Wu, E. P. Woo, *Science* **290**, 2123 (2000).
- [3] S. E. Shaheen, R. Radspinner, N. Peyghambarian, G. E. Jabbour, *Appl. Phys. Lett.* **79**, 2996 (2001).
- [4] C. F. Huebner, J. B. Carroll, D. D. Evanoff Jr. , Y. Ying, B. J. Stevenson, J. R. Lawrence, J. M. Houchins, A. L. Foguth, J. Sperry, S. H. Foulger, *J. Mater. Chem.* **18**, 4942 (2008).
- [5] D. Tobjörk, N.J. Kaihovirta, T. Mäkelä, F.S. Pettersson, R. Österbacka, *Org. Electron.* **9**, 921 (2008).

Chapter 2 Literature Review

- [6] Flexible Flat Panel Displays, G. P. Crawford, Wiley (2005).
- [7] K. W. Paik, A. L. Ruoff, *J. Adhes. Sci. Technol.* **4**, 465 (1990).
- [8] D. Majumdar, R. G. Spahn, *J. Adhes. Sci. Technol.* **5**, 349 (1991).
- [9] M. Menezes, I. S. Robertson, H. K. Birnbaum, *J. Mater. Res.* **14**, 4025 (1999).
- [10] N. Inagaki, S. Tasaka, A. Onodera, *J. Appl. Polym. Sci.* **73**, 1645 (1999).
- [11] O. Kraft, R. Schwaiger, P. Wellner, *Mater. Sci. Eng.*, **A319**, 919 (2001).
- [12] G. A. Shafeev, P. Hoffmann, *Appl. Surf. Sci.*, **138/139**, 455 (1999).

- [13] K. Kordás, S. Leppävuori, A. Uusimäki, Thomas F. George, L. Nánai, R. Vajtai, K. Bali, J. Békési, *Thin Solid Films* **384**, 185 (2001).
- [14] M. Seita, H. Nawafune, T. Kanai, T. Nishioka, S. Mizumoto, *Electron. Circuits World Conv.*, **8**, 1 (1999).
- [15] H. Nawafune, T. Nishioka, H. Tsuji, S. Mizumoto, M. Seita, M. Kusaka, *J. Jpn. Inst. Electron. Packag.* **2**, 390 (1999).
- [16] S. Ikeda, K. Akamatsu, H. Nawafune, *J. Mater. Chem.* **11**, 2919 (2001).
- [17] K. Akamatsu, S. Ikeda, H. Nawafune, *Langmuir* **19**, 10366 (2003).
- [18] S. Ikeda, H. Yanagimoto, K. Akamatsu, H. Nawafune, *Adv. Funct. Mater.* **17**, 889 (2007).
- [19] R. R. Thomas, S. L. Buchwalter, L. P. Buchwalter, T. H. Chao, *Macromolecules*, **25**, 4559 (1992).
- [20] L. E. Stephans, A. Myles, R. R. Thomas, *Langmuir* **16**, 4706 (2000).
- [21] H. B. Michaelson, *J. Appl. Phys.* **48**, 4729 (1977).
- [22] N.J. Chou, C.H. Tang, *J. Vac. Sci. Technol.* **A2**, 751 (1984).
- [23] E. Kondoh, *Thin Solid Films* 359 (2000) 255.
- [24] M. W. Rowell, M. A. Topinka, M. D. McGehee, H. J. Prall, G. Dennler, N. S. Sariciftci, L. Hu and G. Gruner, *Appl. Phys. Lett.* **88**, 233506 (2006).
- [25] A. D. Pasquier, H. E. Unalan, A. Kanwal, S. Miller and M. Chhowalla, *Appl. Phys. Lett.* **87**, 203511 (2005).
- [26] J. S. Kim, M. Granström, R. H. Friend, N. Johansson, W. R. Salaneck, R. Daik, W. J. Feast, F. Cacialli. *J. Appl. Phys.* **84**, 6859 (1998).
- [27] Y. Park, V. Choong, Y. Gao, B. R. Hsieh, C. W. Tang, *Appl. Phys. Lett.* **68**, 2699 (1996).
- [28] E. Moons, M. Eschle, M. Graetzel, *Appl. Phys. Lett.* **71**, 3305 (1997).
- [29] L. Zugangy, Z. Weimingy, J. Rongbiny, Z. Zhiliny, J. Xueyiny, X. Minzhaoz, F.

- Bin, *J. Phys. Condens. Matter* **8**, 3221 (1996).
- [30] T. M. Brown, J. S. Kim, R. H. Friend, F. Cacialli, R. Daik, W. J. Feast, *Appl. Phys. Lett.* **75**, 1679 (1999).
- [31] L. Lindell, A. Burquel, F. L. E. Jakobsson, V. Lemaire, M. Berggren, R. Lazzaroni, J. Cornil, W. R. Salaneck, X. Crispin, *Chem. Mater.* **18**, 4246 (2006).
- [32] M. Shiraishi, M. Ata, *Carbon* **39**, 1913 (2001).
- [33] W. R. Small, F. Masdarolomoor, G. G. Wallace, M. in het Panhuis, *J. Mater. Chem.* **17**, 4359 (2007).
- [34] C. W. Tang, *Appl. Phys. Lett.* **48**, 183 (1986).
- [35] P. Peumans, V. Bulovic, S. R. Forrest, *Appl. Phys. Lett.* **76**, 2650 (2000).
- [36] P. Peumans, S. R. Forrest, *Appl. Phys. Lett.* **79**, 126 (2001).
- [37] G. Yu, J. Guo, J. C. Hummelen, F. Wudl, A. J. Hegger, *Science* **270**, 1789 (1995).
- [38] M. Granström, K. Petrisch, A. C. Arias, A. Lux, M. R. Andersson, R. H. Friend, *Nature* **395**, 257 (1998).
- [39] S. E. Shaheen, C. J. Brabec, S. Sariciftci, F. Padinger, T. Fromherz, J. C. Hummelen, *Appl. Phys. Lett.* **78**, 841 (2001).
- [40] F. Padinger, R. S. Rittberger, N. S. Sariciftci, *Adv. Funct. Mater.* **13**, 85 (2003).
- [41] W. U. Huynh, J. J. Dittmer, A. P. Alivisatos, *Science* **295**, 2425 (2002).
- [42] M. K. Nazeeruddin, A. Kay, I. Rodicio, R. Humphry-Baker, E. Müller, P. Liska, N. Vlachopoulos, M. Grätzel, *J. Am. Chem. Soc.* **115**, 6382 (1993).
- [43] A. Hagfeldt, M. Grätzel, *Acc. Chem. Res.* **33**, 269 (2000).
- [44] U. Bach, D. Lupo, P. Comte, J. E. Moser, F. Weissörtel, J. Salbeck, H. Speitzer, M. Grätzel, *Nature* **395**, 583 (1998).
- [45] H. Hoppe, N. S. Sariciftci, *J. Mater. Res.* **19**, 1925 (2004).
- [46] C. J. Brabec, N. S. Sariciftci, J. C. Hummelen, *Adv. Funct. Mater.* **11**, 15 (2001).
- [47] R. Koeppel, N. S. Sariciftci, *Photochem. Photobiol. Sci.* **5**, 1122 (2006).

- [48] Photoinduced Electron Transfer, M. A. Fox, M. Chanon, Elsevier, Amsterdam (1988).
- [49] I. H. Campbell, T. W. Hagler, D. L. Smith, *Phys. Rev. Lett.* **76**, 1900 (1996).
- [50] B. A. Gregg, M. C. Hanna, *J. Appl. Phys.* **93**, 3605 (2003).
- [51] M. C. Scharber, D. Mühlbacher, M. Koppe, P. Denk, C. Waldauf, A. J. Heeger, C. J. Brabec, *Adv. Mater.* **18**, 789 (2006).
- [52] C.H. Lee, G. Yu, D. Moses, A.J. Heeger, *Phys. Rev. B* **49**, 2396 (1994).
- [53] P. G. d. Costa, E. M. Conwell, *Am. Phys. Soc. Rap. Comm.* **48**, 1993 (1993).
- [54] R. N. Marks, J. J. M. Halls, D. D. C. Bradley, R. H. Friend, A. B. Holmes, *J. Phys.: Cond. Mat.* **6**, 1379 (1994).
- [55] S. Barth, H. Baessler, *Phys.Rev.Lett.* **79**, 4445 (1997).
- [56] M. Chandross, S. Mazumdar, S. Jeglinski, X. Wei, Z.V. Vardeny, E.W. Kwock, T.M. Miller, *J.Phys.:Condens.Matter* **6**, 1379 (1994).
- [57] J. Frenkel, *Phys. Rev.* **38**, 309 (1931).
- [58] R. Peierls, *Ann. Phys.* **13**, 905 (1932).
- [59] G.H. Wannier, *Phys. Rev.* **52**, 191 (1937).
- [60] Pergamon Press, K. C. Kao, W. Hwang, Oxford (1981).
- [61] R. H. Friend, G. J. Denton, J. J. M. Halls, N. T. Harrison, A. B. Holmes, A. Koehler, A. Lux, S. C. Moratti, K. Pichler, N. Tessler, K. Towns, *Synth.Met.* **84**, 463 (1997).
- [62] R. H. Friend, G. J. Denton, J. J. M. Halls, N. T. Harrison, A. B. Holmes, A. Koehler, A. Lux, S. C. Moratti, K. Pichler, N. Tessler, K. Towns, H. F. Wittmann, *Solid State Communications* **102**, 249 (1997).
- [63] J. Cornil, A.J. Heeger, J.L. Bredas, *Chem. Phys. Lett.* **272**, 463 (1997).
- [64] J.H. Burroughes, D.D.C. Bradley, A.R. Brown, R.N. Marks, K. Mackay, R.H. Friend, P.L. Burns, A.B. Holmes, *Nature* **347**, 539 (1990).
- [65] D. Braun, A.J. Heeger, *Appl. Phys. Lett.* **58**, 1982 (1991).

- [66] Organic Light-Emitting Devices: A Survey, J. Shinar, Springer, New York (2004).
- [67] D. C. Coffey, D. S. Ginger, *Nature Mater.* **5**, 735 (2006).
- [68] P. Peumans, A. Yakimov, S. R. Forrest, *J. Appl. Phys.* **93**, 3693 (2003).
- [69] D. Cheyng, H. Gommans, M. Odijk, J. Poortmans, P. Heremans, *Sol. Energy Mater. Sol. Cells* **90**, 399 (2006).
- [70] K. Suemori, Y. Matsumura, M. Yokoyama, M. Hiramoto, *Jpn. J. Appl. Phys.* **45**, L472 (2006).
- [71] V. Djara, J.C. Bernede, *Thin Solid Films* **493**, 273 (2005).
- [72] Z. R. Hong, Z. H. Huang, X. T. Zeng, *Thin Solid Films* **515**, 3019 (2007).
- [73] R. N. Marks, J. J. M. Halls, D. D. C. Bradley, R. H. Friend, A. B. Holmes, *J. Phys. Condens. Matter.* **6**, 1379 (1994).
- [74] L. S. Roman, L. Mammo, A. A. Pettersson, M. R. Andersson, O. Inganäs, *Adv. Mater.* **10**, 774 (1998).
- [75] N. S. Sariciftci, L. Smilowitz, A. J. Heeger, F. Wudl, *Science* **258**, 1474 (1992).
- [76] V. Dyakonov, G. Zorinants, M. Scharber, C. J. Brabec, R. A. J. Janssen, J. C. Hummelen, N. S. Sariciftci, *Phys. Rev. B* **59**, 8019 (1999).
- [77] G. Yu, J. Gao, J. C. Hummelen, F. Wudl, A. J. Heeger, *Science* **270**, 1789 (1995).
- [78] S. E. Shaheen, C. J. Brabec, N. S. Sariciftci, F. Padinger, T. Fromherz, J. C. Hummelen, *Appl. Phys. Lett.* **78**, 841 (2001).
- [79] M. Granstrom, K. Petritsch, A. C. Arias, A. Lux, M. R. Andersson, R. H. Friend, *Nature* **395**, 257 (1998).
- [80] K.M. Coakley, Y. Liu, M.D. McGehee, K.L. Frindell, G.D. Stucky, *Adv. Func. Mater.* **13**, 301 (2003).
- [81] F. Yang, M. Shtein, S. R. Forrest, *J. Appl. Phys.* **98**, 124906 (2005).
- [82] J. Rostalski, D. Meissner, *Sol. Energy Mater. Sol. Cells* **61**, 87 (2000).
- [83] H. Hoppe, N. S. Sariciftci, *J. Mater. Res.* **19**, 1924 (2004).

- [84] G. Dennler, M. C. Scharber, C. J. Brabec, *Adv. Mater.* **21**, 1 (2009).
- [85] W. A. Zisman, *Ind. Eng. Chem.* **55**, 19 (1963).
- [86] Contact angle, wettability and adhesion Advances in Chemistry Series vol 43 (Washington, DC: American Chemical Society), W. A. Zisman (1964).
- [87] Properties of Polymers (Amsterdam: Elsevier) chapters 4 and 8, D. W. Van Krevelen (1976).

Chapter 4 Chemical Formation of Palladium-free Surface-nickelized Polyimide Film for Flexible Electronics

- [88] J. D. Rancourt, G. M. Porta, T. L. Taylor, *Thin Solid Films* **158** (1988) 189.
- [89] M. M. Ellison, L.T..Taylor, *Chem. Mater.* **6**, 990 (1994).
- [90] J. B. Ma, J. Dragon, W. Van Derveer, A. Entenberg, V. Lindberg, M. Ansel, D. Y. Shih, P. Lauro, *J. Adhes. Sci. Technol.* **9**, 487 (1995).
- [91] C. A. Chang, J.E. Balgin, A. G. Schrott, K. C. Lin, *Appl. Phys. Lett.* **51**, 103 (1987).
- [92] N. Inagaki, S. Tasaka, K. Hibi, *J. Adhes. Sci. Technol.* **8**, 395 (1994).
- [93] G. Rozovskis, J. Vinkevicius, J. Jaciauskiene, *J. Adhes. Sci. Technol.* **10**, 399 (1996).
- [94] Y. Nakamura, Y. Suzuki, Y. Watanabe, *Thin Solid Films* **290/291**, 367 (1996).
- [95] A. M. Ektessabi, S. Hakamata, *Thin Solid Films* **377/378**, 621 (2000).
- [96] P. C. Chiang, W. T. Whang, S. C. Wu, K.R. Chuang, *Polymer* **45**, 4465 (2004).
- [97] R. E. Southward, D. W. Thompson, A. K. St. Clair, *Chem. Mater.* **9**, 501 (1997).
- [98] T. Sawada, S. Ando, S. Sasaki, *Appl. Phys. Lett.* **74**, 938 (1999).
- [99] S. Ikeda, K. Akamatsu, H. Nawafune, *J. Mater. Chem.* **11**, 2919 (2001).

- [100] K. Akamatsu, S. Ikeda, H. Nawafune, *Langmuir* **19**, 10366 (2003).
- [101] K. Akamatsu, S. Ikeda, H. Nawafune, S. Deki, *Chem. Mater.* **15**, 2488 (2003).
- [102] S. Ikeda, K. Akamatsu, H. Nawafune, T. Nishino, S. Deki, *J. Phys. Chem. B* **108**, 15599 (2004).
- [103] K. Akamatsu, S. Ikeda, H. Nawafune, H. Yanagimoto, *J. Am. Chem. Soc.* **126**, 10822 (2004).
- [104] Z. Wu, D. Wu, S. Qi, T. Zhang, R. Jin, *Thin Solid Films* **493**, 179 (2005).
- [105] Z. Wu, D. Wu, W. Yang, R. Jin, *J. Mater. Chem.* **16**, 310 (2006).
- [106] R. T. Richard, *Langmuir* **12**, 5247 (1996).
- [107] E. S. Lori, M. Anthony, R. T. Richard, *Langmuir* **16**, 4706 (2000).
- [108] R. T. Richard, *Langmuir* **19**, 5763 (2003).
- [109] C. Ailger, R. Stadler, *Macromolecules* **23**, 2097 (1990).
- [110] N. J. Chou, C. H. Tang, *J. Vac. Sci. Technol.* **A2**, 751 (1984).
- [111] F. S. Ohuchi, S. C. Freilich, *J. Vac. Sci. Technol.* **A4**, 1039 (1986).
- [112] J. L. Jordan, P. N. Sanda, J. F. Morar, C.A. Kovac, F. J. Himpsel, R. A. Pollack, *J. Vac. Sci. Technol.* **A4**, 1046 (1986).
- [113] L. J. Atanasoska, S. G. Anderson, H. M. Meyer III, Z. Lin, J. H. Weaver, *J. Vac. Sci. Technol.* **A5**, 3325 (1987).
- [114] F. Faupel, R. Willecke, A. Thran, *Mater. Sci. Eng. R* **22**, 1 (1998).
- [115] E. Kondoh, *Thin Solid Films* **359**, 255 (2000).
- [116] T. C. Wang, B. Chen, M. F. Rubner, R. E. Cohen, *Langmuir* **17**, 6610 (2001).
- [117] T. C. Wang, M. F. Rubner, R. E. Cohen, *Chem. Mater.* **15**, 299 (2003).
- [118] T. Homma, A. Tamaki, H. Nakai, T. Osaka, *J. Electroanal. Chem.* **559**, 131 (2003).
- [119] ASTM D3359-95 standard method for measuring adhesion by tape test, Annual Book of ASTM Standards, Vol. 06.01.
- [120] T. Osaka, N. Takano, T. Kurokawa, T. Kaneko, K. Ueno, *Surf. Coat. Technol.*

169/170, 124 (2005).

Chapter 5 High-Conductivity Poly(3,4-ethylenedioxythiophene):Poly-(styrene sulfonate) Film for Use in ITO-Free Polymer Solar Cells

- [121] G. Li, V. Shrotriya, J. S. Huang, Y. Yao, T. Moriarty, K. Emery, Y. Yang, *Nat. Mater.* **4**, 864 (2005).
- [122] W. L. Ma, C. Y. Yang, X. Gong, K. Lee, A. J. Heeger, *Adv. Funct. Mater.* **15**, 1617 (2005).
- [123] J. Y. Kim, K. Lee, N. E. Coates, D. Moses, T.-Q. Nguyen, M. Dante, A. J. Heeger, *Science* **317**, 222 (2007).
- [124] C. J. Brabec, N. S. Sariciftci, J. C. Hummelen, *Adv. Funct. Mater.* **11**, 15 (2001).
- [125] H. Spanggaard, F. C. Krebs, *Sol. Energy Mater. Sol. Cells* **83**, 125 (2004).
- [126] K. M. Coakley, M. D. McGehee, *Chem. Mater.* **16**, 4533 (2004).
- [127] H. Hoppe, N. S. Sariciftci, *J. Mater. Res.* **19**, 1924 (2004).
- [128] E. Bundgaard, F. C. Krebs, *Sol. Energy Mater. Sol. Cells* **91**, 954 (2007).
- [129] S. Günes, H. Neugebauer, N. S. Sariciftci, *Chem. Rev.*, **107**, 1324 (2007).
- [130] M. Jorgensen, K. Norrman, F. C. Krebs, *Sol. Energy Mater. Sol. Cells* **92**, 686 (2008).
- [131] B. C. Thompson, J. M. J. Fréchet, *Angew. Chem. Int. Ed.* **47**, 58 (2008).
- [132] F. C. Krebs, H. Spanggaard, T. Kjær, M. Biancardo, J. Alstrup, *Mater. Sci. Eng. B* **138**, 106 (2007).
- [133] C. Lungenschmied, G. Dennler, H. Neugebauer, S. N. Sariciftci, M. Glatthaar, T. Meyer, A. Meyer, *Sol. Energy Mater. Sol. Cells* **91**, 379 (2007).
- [134] X. Yang, J. Loos, S. C. Veenstra, W. J. H. Verhees, M. M. Wienk, J. M. Kroon, M.

- A. J. Michels, R. A. J. Janssen, *Nano Lett.* **5**, 579 (2005).
- [135] F. C. Krebs, K. Norrman, *Prog. Photovolt: Res. Appl.* **15**, 697 (2007).
- [136] M. W. Rowell, M. A. Topinka, M. D. McGehee, H. J. Prall, G. Dennler, N. S. Sariciftci, L. Hu, G. Gruner, *Appl. Phys. Lett.* **88**, 233506 (2006).
- [137] A. D. Pasquier, H. E. Unalan, A. Kanwal, S. Miller, M. Chhowalla, *Appl. Phys. Lett.* **87**, 203511 (2005).
- [138] T. Aernouts, P. Vanlaeke, W. Geens, J. Poortmans, P. Heremans, S. Borgis, R. Mertens, R. Andriessen, L. Leenders, *Thin Solid Films* **451**, 22 (2004).
- [139] J. Y. Lee, S. T. Connor, Y. Cui, P. Peumans, *Nano Lett.* **8**, 689 (2008).
- [140] F. Zhang, M. Johansson, M. R. Andersson, J. C. Hummelen, O. Inganäs, *Adv. Mater.* **14**, 662 (2002).
- [141] J. Y. Kim, J. H. Jung, D. E. Lee, J. Joo, *Synth. Met.* **126**, 311 (2002).
- [142] B. D. Martin, N. Nikolov, S. K. Pollack, A. Saprigin, R. Shashidhar, F. Zhang, P. A. Heiney, *Synth. Met.* **142**, 187 (2004).
- [143] Y. H. Ha, N. Nikolov, S. K. Pollack, J. Mastrangelo, B. D. Martin, R. Shashidhar, *Adv. Funct. Mater.* **14**, 615 (2004).
- [144] J. Ouyang, Q. Xu, C. W. Chu, Y. Yang, G. Li, J. Shinar, *Polymer* **45**, 8443 (2004).
- [145] S. Ashizawa, R. Horikawa, H. Okuzaki, *Synth. Met.* **153**, 5 (2005).
- [146] J. Hung, P. F. Miller, J. S. Wilson, A. J. de Mello, J. C. de Mello, D. D. C. Bradley, *Adv. Funct. Mater.* **15**, 290 (2005).
- [147] J. Ouyang, C. W. Chu, F. C. Chen, Q. Xu, Y. Yang, *Adv. Funct. Mater.* **15**, 203 (2005).
- [148] B. Winther-Jensen, F. C. Krebs, *Sol. Energy Mater. Sol. Cells* **90**, 123 (2006).
- [149] J. Huang, X. Wang, Y. Kim, A. J. de Mello, D. D. C. Bradley, J. C. de Mello, *Phys. Chem. Chem. Phys.* **8**, 3904 (2006).
- [150] X. Crispin, F. L. E. Jakobsson, A. Crispin, P. C. M. Grim, P. Andersson, A. Volodin,

- C. van Haesendonck, M. van der Auweraer, W. R. Salaneck, M. Berggren, *Chem. Mater.* **18**, 4354 (2006).
- [151] L. Lindell, A. Burquel, F. L. E. Jakobsson, V. Lemaur, M. Berggren, R. Lazzaroni, J. Cornil, W. R. Salaneck, X. Crispin, *Chem. Mater.* **18**, 4246 (2006).
- [152] T. Y. Kim, J. E. Kim, K. S. Suh, *Polym. Int.* **55**, 80 (2006).
- [153] C. J. Ko, Y. K. Lin, F. C. Chen, C. W. Chu, *Appl. Phys. Lett.* **90**, 063509 (2007).
- [154] S. Chaudhary, H. Lu, A. M. Müller, C. J. Bardeen, M. Ozkan, *Nano Lett.* **7**, 1973 (2007).
- [155] U. Barsch, F. Beck, *Electrochim. Acta*, **41**, 1761 (1996).
- [156] S. K. M. Jönsson, J. Brigerson, X. Crispin, G. Greczynski, W. Osikowicz, A. W. Denier van der Gon, W. R. Salaneck, M. Fahlman, *Synth. Met.* **10361**, 1 (2003).
- [157] S. Timpanaro, M. Kemerink, F. J. Touwslager, M. M. de Kok, S. Schrader, *Chem. Phys. Lett.* **394**, 339 (2004).
- [158] A. M. Nardes, M. Kemerink, R. A. J. Janssen, J. A. M. Bastiaasen, N. M. M. Kiggen, B. M. W. Langeveld, A. J. J. M. van Breemen, M. M. de Kok, *Adv. Mater.* **19**, 1196 (2007).
- [159] A. M. Nardes, M. Kemerink, R. A. J. Janssen, *Phys. Rev. B* **76**, 085208 (2007).

Chapter 6 All-Solution-Processed Inverted Polymer Solar Cells on Granular Surface-Nickelized Polyimide

- [160] J.Y. Kim, S.H. Kim, H.H. Lee, K. Lee, W. Ma, X. Gong, A.J. Heeger, *Adv. Mater.* **18**, 572 (2006).
- [161] S.S. Kim, S.I. Na, J. Jo, G. Tae, D.Y. Kim, *Adv. Mater.* **19**, 4410 (2007).

- [162] J.Y. Kim, K. Lee, N.E. Coates, D. Moses, T.Q. Nguyen, M. Dante, A.J. Heeger, *Science* **317**, 222 (2007).
- [163] M.D. Irwin, D.B. Buchholz, A.W. Hains, R.P.H. Chang, T.J. Marks, *Proc. Natl. Acad. Sci. U.S.A.* **105**, 2783 (2008).
- [164] C.P. Chen, S.H. Chan, T.C. Chao, C. Ting, B.T. Ko, *J. Am. Chem. Soc.* **130**, 12828 (2008).
- [165] X. Yang, J. Loos, S.C. Veenstra, W.J.H. Verhees, M.M. Wienk, J.M. Kroon, M.A.J. Michels, R.A.J. Janssen, *Nano Lett.* **5**, 579 (2005).
- [166] F.C. Krebs, K. Norrman, *Prog. Photovolt: Res. Appl.* **15**, 697 (2007).
- [167] M.S. White, D.C. Olson, S.E. Shaheen, N. Kopidakis, D.S. Ginley, *Appl. Phys. Lett.* **89**, 143517 (2006).
- [168] C. Waldauf, M. Morana, P. Denk, P. Schilinsky, K. Coakley, S.A. Choulis, C.J. Brabec, *Appl. Phys. Lett.* **89**, 233517 (2006).
- [169] G. Li, C.W. Chu, V. Shrotriya, J. Huang, Y. Yang, *Appl. Phys. Lett.* **88**, 253503 (2006).
- [170] H.H. Liao, L.M. Chen, Z. Xu, G. Li, Y. Yang, *Appl. Phys. Lett.* **92**, 173303 (2008).
- [171] R. Steim, S.A. Choulis, P. Schilinsky, C.J. Brabec, *Appl. Phys. Lett.* **92**, 093303 (2008).
- [172] T. Ameri, G. Dennler, C. Waldauf, P. Denk, K. Forberich, M.C. Scharber, C.J. Brabec, K. Hingerl, *J. Appl. Phys.* **103**, 084506 (2008).
- [173] B.Y. Yu, A. Tsai, S.P. Tsai, K.T. Wong, Y. Yang, C.W. Chu, J.J. Shyue, *Nanotechnology* **19**, 255202 (2008).
- [174] S.K. Hau, H.L. Yip, O. Acton, N.S. Baek, H. Ma, A.K. Y. Jen, *J. Mater. Chem.* **18**, 5113 (2008).
- [175] T. Nyberg, *Synth. Met.* **140**, 281 (2004).
- [176] M. Glatthaar, M. Niggemann, B. Zimmermann, P. Lewer, M. Riede, A. Hinsch, J.

- Luther, *Thin Solid Films* **491**, 298 (2005).
- [177] B. Zimmermann, M. Glatthaar, M. Niggemann, M.K. Riede, A. Hinsch, A. Gombert, *Sol. Energy Mater. Sol. Cells* **91**, 374 (2007).
- [178] K. Tvingstedt, O. Inganäs, *Adv. Mater.* **19**, 2893 (2007).
- [179] V. Kažukauskas, M. Pranaitis, F. Kajzar, M. Glatthaar, A. Hinsch, *Mol. Cryst. Liquid Cryst.* **484**, 373 (2008).
- [180] J. Kim, D.Y. Khang, J.H. Kim, H.H. Lee, *Appl. Phys. Lett.* **92**, 133307 (2008).
- [181] K. Tvingstedt, N.K. Persson, O. Inganäs, *Appl. Phys. Lett.* **91**, 113514 (2007).
- [182] L.S. Roman, O. Inganäs, T. Granlund, T. Nyberg, M. Svensson, M.R. Andersson, J.C. Hummelen, *Adv. Mater.* **12**, 189 (2000).
- [183] K. Akamatsu, S. Ikeda, H. Nawafune, *Langmuir* **19**, 10366 (2003).
- [184] S. Ikeda, H. Yanagimoto, K. Akamatsu, H. Nawafune, *Adv. Funct. Mater.* **17**, 889 (2007).
- [185] Y.S. Hsiao, W.T. Whang, S.C. Wu, K.R. Chuang, *Thin Solid Films* **516**, 4258 (2008).
- [186] Y. Matsumura, Y. Enomoto, M. Sugiyama, K. Akamatsu, H. Nawafune, *J. Mater. Chem.* **18**, 5078 (2008).
- [187] A. Hayakawa, O. Yoshikawa, T. Fujieda, K. Uehara, S. Yoshikawa, *Appl. Phys. Lett.* **90**, 163517 (2007).
- [188] F. Zhang, M. Ceder, O. Inganäs, *Adv. Mater.* **19**, 1835 (2007).
- [189] Z. Tan, C. Yang, E. Zhou, X. Wang, Y. Li, *Appl. Phys. Lett.* **91**, 023509 (2007).
- [190] Y.S. Hsiao, W.T. Whang, C.P. Chen, Y.C. Chen, *J. Mater. Chem.* **18**, 5948 (2008).
- [191] S.K. M. Jönsson, J. Brigerson, X. Crispin, G. Greczynski, W. Osikowicz, A.W. Denier van der Gon, W.R. Salaneck, M. Fahlman, *Synth. Met.* **10361**, 1 (2003).
- [192] B.D. Martin, N. Nikolov, S.K. Pollack, A. Saprigin, R. Shashidhar, F. Zhang, P.A. Heiney, *Synth. Met.* **142**, 187 (2004).

- [193] J. Ouyang, Q. Xu, C.W. Chu, Y. Yang, G. Li, J. Shinar, *Polymer* **45**, 8443 (2004).
- [194] J. Ouyang, C.W. Chu, F.C. Chen, Q. Xu, Y. Yang, *Adv. Funct. Mater.* **15**, 203 (2005).
- [195] J. Hung, P.F. Miller, J.S. Wilson, A.J. de Mello, J.C. de Mello, D.D.C. Bradley, *Adv. Funct. Mater.* **15**, 290 (2005).
- [196] A.M. Nardes, M. Kemerink, M.M. de Kok, E. Vinken, K. Maturova, R.A.J. Janssen, *Org. Electron.* **9**, 727 (2008).
- [197] H.L. Skriver, N.M. Rosengaard, *Phys. Rev. B* **46**, 7157 (1992).
- [198] G. Li, V. Shrotriya, Y. Yao, J. Huang, Y. Yang, *J. Mater. Chem.* **17**, 3126 (2007).
- [199] S. Chaudhary, H. Lu, A.M. Müller, C.J. Bardeen, M. Ozkan, *Nano Lett.* **7**, 1973 (2007).
- [200] T. Aernouts, P. Vanlaeke, W. Geens, J. Poortmans, P. Heremans, S. Borghs, R. Mertens, R. Andriessen, L. Leenders, *Thin Solid Films* **451**, 22 (2004).
- [201] J.Y. Lee, S. T. Connor, Y. Cui, P. Peumans, *Nano Lett.* **8**, 689 (2008).
- [202] J. Huang, X. Wang, Y. Kim, A. J. de Mello, D.D.C. Bradley, J.C. de Mello, *Phys. Chem. Chem. Phys.* **8**, 3904 (2006).
- [203] S.I. Na, S.S. Kim, J. Jo, D.Y. Kim, *Adv. Mater.* **20**, 1 (2008).
- [204] V. Terrazzoni-Daudrix, J. Guillet, X. Niquille, A. Shah, R. Morf, A. Tishchenko, V. Brioude, O. Parriaux, D. Fischer, *Mat. Res. Soc. Symp. Proc.* **769**, H6.14.1 (2003).
- [205] F. Monestier, J.-J. Simon, P. Torchio, L. Escoubas, F. Flory, S. Bailly, R. de Bettignies, S. Guillerez, C. Defranoux, *Sol. Energy Mater. Sol. Cells* **91**, 405 (2007).
- [206] L. A. A. Pettersson, S. Ghosh, O. Inganäs, *Org. Electron.* **3**, 143 (2002).

Chapter 7 Morphological Control of CuPc and its Application in Organic

Solar Cells

- [207] J. Nelson, *Science* **293** 1059 (2001).
- [208] W. U. Huynh, J. J. Dittmer, A. P. Alivisatos, *Science* **295** 2425 (2002).
- [209] P. Peumans, S. Uchida, S. R. Forrest, *Nature* **425** 158 (2003).
- [210] P. Peumans, A. Yakimov, S. R. Forrest, *J. Appl. Phys.* **93** 3693 (2003).
- [211] V. Djara, J. C. Bernède, *Thin Solid Films* **493** 273 (2005).
- [212] B. P. Rand, J. Xue, S. Uchida, S. R. Forrest, *J. Appl. Phys.* **98** 124902 (2005).
- [213] K. Suemori, Y. Matsumura, M. Yokoyama, M. Hiramoto, *Jpn. J. Appl. Phys.* **45** L472 (2006).
- [214] P. Liu, Q. Li, M. Huang, W. Pan, W. Deng, *Appl. Phys. Lett.* **89** 213506 (2006).
- [215] F. Brovelli, B. L. Rivas, J. C. Bernède, M. A. del Valle, F. R. Díaz, Y. Berredjem, *Polym. Bull.* **58** 521 (2007).
- [216] D. Cheynsa, H. Gommans, M. Odijk, J. Poortmans, P. Heremans, *Sol. Energy Mater. Sol. Cells* **91** 399 (2007).
- [217] H. L. Wong, C. S. K. Mak, W. K. Chan, A. B. Djurišić, *Appl. Phys. Lett.* **90** 081107 (2007).
- [218] M. Y. Chan, S. L. Lai, M. K. Fung, C. S. Lee, S. T. Lee, *Appl. Phys. Lett.* **90** 023504 (2007).
- [219] B. P. Rand, D. P. Burk, *Phys. Rev. B* **75** 115327 (2007).
- [220] P. Peumans, S. R. Forrest, *Appl. Phys. Lett.* **79** 126 (2001).
- [221] J. Xue, B. P. Rand, S. Uchida, S. R. Forrest, *J. Appl. Phys.* **98** 124903 (2005).
- [222] S. M. Schultes, P. Sullivan, S. Heutz, B. M. Sanderson, T. S. Jones, *Mater. Sci. Eng. C* **25** 858 (2005).
- [223] F. Yang, M. Shtein, S. R. Forrest, *J. Appl. Phys.* **98** 124906 (2005).

- [224] F. Yang, S. R. Forrest, *Adv. Mater.* **18** 2018 (2006).
- [225] R. R. Lunt, J. B. Benziger, S. R. Forrest, *Appl. Phys. Lett.* **90** 181932 (2007).
- [226] S. C. Suen, W. T. Whang, F. J. Hou, B. T. Dai, *Org. Electron.* **7** 428 (2006).
- [227] M. C. Hersam, N. P. Guisinger, J. W. Lyding, *Nanotechnology* **11** 70 (2000).
- [228] A. Tekiel, M. Goryl, M. Szymonski, *Nanotechnology* **18** 475707 (2007).
- [229] E. G. Boguslavskii, S. A. Prokhorova, V. A. Nadolinnyi, *J. Struct. Chem.* **46** 1014 (2005).
- [230] L. Lozzi, S. Santucci, S. La Rosa, B. Delley, S. Picozzi, *J. Chem. Phys.* **121** 1883 (2004).
- [231] S. Karan, B. Mallik, *Solid State Commun.* **143** 289 (2007).
- [232] A. W. Adamson, *Physical Chemistry of Surfaces*, John Wiley & Sons, Inc (1990).
- [233] X. Crispin, F. L. E. Jakobsson, A. Crispin, P. C. M. Grim, P. Andersson, A. Volodin, C. van Haesendonck, M. Van der Auweraer, W. R. Salaneck, M. Berggren, *Chem. Mater.* **18** 4354 (2006).
- [234] W. A. Zisman. Contact angle, wettability and adhesion. In: *Advances in Chemistry*, Series 43. Washington, DC: American Chemical Society; (1964).
- [235] D. W. Van Krevelen, *Properties of Polymers*, Chapters 4 and 8 (1976).

List of Publications

Journal Publications

1. **Yu-Sheng Hsiao**, Wha-Tzong Whang, Sheng-Chang Wu, Kuen-Ru Chuang, “Chemical formation of palladium-free surface-nickelized polyimide film for flexible electronics”, *Thin Solid Films* **516**, 4258 (2008). (Impact Factor 1.693)
2. **Yu-Sheng Hsiao**, Wha-Tzong Whang, Shich-Chang Suen, Jau-Ye Shiu, Chih-Ping Chen, “Morphological control of CuPc and its application in organic solar cells”, *Nanotechnology* **19**, 415603, (2008). (Impact Factor 3.310)
3. **Yu-Sheng Hsiao**, Wha-Tzong Whang, Chih-Ping Chen, Yi-Chun Chen, “High-conductivity poly(3,4-ethylenedioxythiophene):poly(styrene sulfonate) film for use in ITO-Free polymer solar cells”, *J. Mater. Chem.* **18**, 5948 (2008). (Impact Factor 4.339)
4. **Yu-Sheng Hsiao**, Wha-Tzong Whang, Chih-Ping Chen, Sheng-Chang Wu, “All-Solution-Processed Inverted Polymer Solar Cells on Granular Surface-Nickelized Polyimide”, *Org. Electron.* (2009). (Impact Factor 3.879)

Patent

1. 黃華宗、**蕭育生**，「表面金屬化聚亞醯胺材料及其製備方法」，中華民國發明專利，九十六年，申請案號：095112434號。
2. Wha-Tzong Whang, **Yu-Sheng Hsiao**, “Surface-metallized polyimide material and method for manufacturing the same claims”, 2007, Patent No: US 2007/0237969 A1.

Project

1. 黃華宗、**蕭育生**、許育銓，國立交通大學與達邁公司建教合作研究計畫「無膠系軟板之表面金屬化聚亞醯胺膜研究」，九十五~九十六年。

Conference Publication

1. **Yu-Sheng Hsiao**, Wha-Tzong Whang, Shich-Chang Suen, Jau-Ye Shiu, Chih-Ping Chen, “Morphology control of CuPc and its application in organic solar cells”, 2007 MRS fall meeting, Boston, USA.

Resume

- 姓名: 蕭育生 (Yu-Sheng Hsiao)
- 性別: 男
- 生日: 70年3月22日, 台北人
- 電子郵件信箱: mrbean@mail2000.com.tw
- 聯絡電話: (學校) 03-5712121-55347 (手機) 0952278502
- 通訊地址: 新竹市大學路 1001 號



國立交通大學材料與工程研究所(黃華宗老師實驗室)

- 永久地址: 台北市辛亥路二段 41 號 11 樓之二

學歷

-
- 博士: 國立交通大學材料與工程研究所 2005.7~2009.4
指導教授: 黃華宗 教授
論文題目: 軟性電路板及電極之製備與特性研究及其於有機太陽能電池之應用
- 碩士: 國立交通大學材料與工程研究所 2003.7~2005.6
指導教授: 黃華宗 教授
論文題目: 化學方法製備鎳奈米顆粒及鎳薄膜於軟性聚亞醯胺基板上與特性研究
- 學士: 國立中興大學化學工程學系 1999.7~2003.6
指導教授: 鄭如忠 教授
專題題目: 由溶膠凝膠反應製備含矽聚亞醯胺之研究

工作經驗

-
- 工業技術研究院 (工讀生) 2007.6~2009.4
從事有機太陽能電池(包括半導體特性之小分子及高分子)相關技術開發、軟性電極應用在軟性電子元件之開發、光電用聚亞醯胺基材開發。
 - 達邁科技 (工讀生) 2003.7~2007.5
因為實驗室與達邁科技公司有建教合作計畫, 其內容為化學製備表面金屬化聚亞醯胺相關技術之開發(發展雙面或單面之無膠系雙層基板)。
 - 國立交通大學材料科學與工程學系 高分子定性分析及高分子物理課程助教。
2005.9~2007.6